Solid-State NMR Spectroscopic Studies Concerning the Biomineralization Process in Diatoms and on Inorganic Phosphorus Chalcogenide Cage Compounds

DISSERTATION ZUR ERLANGUNG DES DOKTORGRADES DER
NATURWISSENSCHAFTEN (DR. RER. NAT.) DER
NATURWISSENSCHAFTLICHEN FAKULTÄT III - BIOLOGIE UND
VORKLINISCHE MEDIZIN DER UNIVERSITÄT REGENSBURG

vorgelegt von
Christian Gröger
aus Denkendorf / Bayern
März 2008

Promotionsgesuch eingereicht am 10.02.2008
Promotionskolloquium stattgefunden am 25.04.2008

Die Arbeit wurde angeleitet von Prof. Dr. Eike Brunner

Prüfungsausschuss:
Vorsitzender : Prof. Dr. Richard Warth
1. Gutachter : Prof. Dr. Eike Brunner
2. Gutachter : Prof. Dr. Manfred Sumper
3. Prüfer : Prof. Dr. Dr. Hans Robert Kalbitzer

Contents

1 Introduction

Nuclear magnetic resonance (NMR) spectroscopy has become an indispensable method for chemical analysis, molecular structure determination, as well as the study of dynamics in organic, inorganic, and biological systems. Although most NMR experiments are performed on liquid-state samples, solid-state NMR becomes more and more attractive because new research topics such as the study of membrane proteins, amyloid fibrils, biominerals, or inorganic clusters demand examination methods which are able to study such systems in their native environment. The present work deals with solid-state NMR spectroscopic studies of diatoms, a special algal species, as well as of inorganic solids.

The characteristic feature of diatoms is the mineralized cell wall containing amorphous silica as well as certain biomolecules. The cell walls exhibit a high degree of complexity and species-specific hierarchical structures. The mechanisms yielding such intricate structures are not well understood. These structures are reproduced under mild physiological conditions and within an amazingly short time. The biological processes generating patterned silica are, therefore, of great interest to the emerging field of nanotechnology. The aim of this work is the characterization of diatom cell walls especially with respect to the presence of organic components enclosed in the inorganic silica matrix and the investigation of the silica metabolism of diatoms by means of solid-state NMR spectroscopic techniques.

A further subject of the present work is the structural characterization of phosphorus chalcogenide cage compounds. The results of single crystal X-ray analysis of such compounds are ambiguous, e.g., with respect to the distinction of phosphorus and sulfur. In addition these compounds are insoluble. Therefore, solid-state NMR spectroscopy appears to be the method of choice for structural analysis of these compounds.

2 General Remarks on Solid-State NMR Spectroscopy

The main theoretical and experimental concepts of solid-state NMR spectroscopy relevant within the present thesis will be briefly described in the following chapter. It covers both, the theory of the NMR Hamiltonian and its main nuclear spin interactions as well as basic solid-state NMR techniques and experiments which are used within this thesis.

2.1 The Nuclear Spin Hamiltonian

[Haeberlen, 1976] [Mehring, 1983] [Smith, 1992a] [Smith, 1992b] [Schmidt-Rohr, 1999] The nuclear spin hamiltonian $\mathscr{H}$ can be expressed as sum of nuclear spin interactions $\mathscr{H}^{\lambda}$ which have all a common structure:

$$\mathscr{H} = \sum_{\lambda} \mathscr{H}^{\lambda} \tag{2.1}$$

$$\mathscr{H}^{\lambda} = C^{\lambda}\, \mathbf{I} \cdot \mathbf{R}^{\lambda} \cdot \mathbf{A}^{\lambda} = C^{\lambda}\, \mathbf{R}^{\lambda} \cdot \mathbf{T}^{\lambda} = C^{\lambda} \sum_{\alpha,\beta=1}^{3} R^{\lambda}_{\alpha\beta} T^{\lambda}_{\alpha\beta} \tag{2.2}$$

The superscript λ denotes the type of interaction and will be omitted in the following for the sake of clarity. C is a constant factor comprising physical constants. $\mathbf{I}$ and $\mathbf{A}$ are vectors and $\mathbf{R}$ is a second-rank Cartesian tensor, in general. The vector $\mathbf{I}$ is normally the angular momentum, whereas the vector $\mathbf{A}$ either represents an angular momentum or a magnetic field vector. The tensor $\mathbf{C}$ depends on the considered magnetic spin interaction. It is convenient to represent the vectors $\mathbf{I}$ and $\mathbf{A}$ as second-rank Cartesian tensor $\mathbf{T}$ formed by the dyadic product of $\mathbf{I}$ and $\mathbf{A}$. $\mathbf{R}$ and $\mathbf{T}$ can be decomposed into their irreducible constituents, the isotropic component $\mathbf{R}^{(0)}$, the traceless antisymmetric component $\mathbf{R}^{(1)}$, and the traceless symmetric tensor $\mathbf{R}^{(2)}$.

$$\mathbf{R} = \mathbf{R}^{(0)} + \mathbf{R}^{(1)} + \mathbf{R}^{(2)} \qquad \mathbf{R}^{(0)} = {}^{1}\!/_{3}\,\mathrm{Tr}(\mathbf{R})\;\mathbb{1} \tag{2.3}$$

$$R^{(1)}_{\alpha\beta} = {}^{1}\!/_{2}\,(R_{\alpha\beta} - R_{\beta\alpha}) \tag{2.4}$$

$$R^{(2)}_{\alpha\beta} = {}^{1}\!/_{2}\,(R_{\alpha\beta} + R_{\beta\alpha}) - R_{\alpha\beta}\;\delta_{\alpha\beta} \tag{2.5}$$

The asymmetric part $\mathbf{R}^{(1)}$ does not contribute to the spectrum in first order and will, therefore, be omitted. The remaining part of $\mathbf{R}$ is diagonal in its principal axes system (PAS). In solid-state NMR, it is convenient to introduce the isotropic parameter ξ, the anisotropy parameter δ, and the asymmetry parameter η instead of the diagonal elements $R_{\alpha\alpha}$.

$$\mathbf{R}(PAS) = \begin{bmatrix} R_{\mathrm{xx}} & & \\ & R_{\mathrm{yy}} & \\ & & R_{\mathrm{zz}} \end{bmatrix} = \xi\;\mathbb{1} + \delta \begin{bmatrix} -{}^{1}\!/_{2}(1+\eta) & & \\ & -{}^{1}\!/_{2}(1-\eta) & \\ & & 1 \end{bmatrix} \tag{2.6}$$

$$\xi = {}^{1}\!/_{3}\,\mathrm{Tr}(\mathbf{R}) \qquad \delta = R_{\mathrm{zz}} - R \qquad \eta = \tfrac{R_{\mathrm{yy}} - R_{\mathrm{xx}}}{\delta} \tag{2.7}$$

$$|R_{\mathrm{zz}} - R| \;\geq\; |R_{\mathrm{xx}} - R| \;\geq\; |R_{\mathrm{yy}} - R| \tag{2.8}$$

The theoretical treatment of rotations, e.g., magic angle spinning (MAS) in space or spin manipulation in spin space, are conveniently described by expressing the Hamiltonian using spherical rather than Cartesian tensors. Equation (2.2) can be written in the irreducible spherical tensor representation as

$$\mathscr{H}^{\lambda} = C^{\lambda} \sum_{l} \sum_{m=-l}^{l} (-1)^{m} R^{\lambda}_{\mathrm{l,m}} T^{\lambda}_{\mathrm{l,-m}} \tag{2.9}$$

Only $R_{\mathrm{l,m}}$ with $l = 0,2$ are nonzero for symmetric 2nd-rank Cartesian tensors $\mathbf{R}$. Furthermore, components with $m = 0,2$ contribute to $\mathbf{R}$ in its PAS, only. Therefore, we need to consider only the following four spherical components $\rho_{\mathrm{l,m}}$ if we transfer the spherical components $(R_{\mathrm{l,m}}(\mathrm{LAB}))$ from the laboratory frame (LAB) to the PAS $(\rho_{\mathrm{l,m}}(\mathrm{PAS}))$ (see equation 2.11):

$$\rho_{0,0} = \xi \quad \rho_{2,0} = \sqrt{{}^{3}\!/_{2}}\;\delta \quad \rho_{2,\pm 2} = {}^{1}\!/_{2}\;\eta\;\delta \tag{2.10}$$

The $T_{\mathrm{l,m}}$ are basically linked to the LAB frame, but the $\rho_{\mathrm{l,m}}$ have to be transferred from the PAS to the LAB frame using Wigner rotation matrices $\mathscr{D}^{l}_{\mathrm{m'm}}(\Omega)$.

$$R_{\mathrm{l,m}}(\mathrm{LAB}) = \sum_{m'} \mathscr{D}^{l}_{\mathrm{m'm}}(\Omega)\; \rho_{\mathrm{l,m'}}(\mathrm{PAS}) \tag{2.11}$$

$\Omega = \alpha, \beta, \gamma$ is the triple of Euler angles describing the orientation of the LAB frame with respect to the PAS. Using the highfield approximation, i.e., assuming that the external magnetic field is very large compared to the internal interactions, only terms which commutate with the external field contribute to the spectrum in first order. Considering only the terms $T_{\mathrm{l,m}}$ with $m = 0$ in the LAB frame results in the secular Hamiltonian.

$$\mathscr{H} = C\,\left\{\xi\; T_{0,0} + \sqrt{{}^{3}/_{2}}\;\delta\;\mathscr{D}^{2}_{0,0}\;T_{20} + {}^{1}/_{2}\;\eta\;\delta\;(\mathscr{D}^{2}_{2,0} + \mathscr{D}^{2}_{-2,0})\;T_{2,0}\right\} \tag{2.12}$$

Often, the samples under study are powders or disordered systems and not single crystals. Powder samples consist of small particles with random orientations and, therefore, powder averaging $\int \mathscr{H}(\Omega)\; d\Omega$ has to be performed.

2.2 Nuclear Spin-Spin Interactions

2.2.1 Chemical Shift Interaction

The hamiltonian $\mathscr{H}^{\mathrm{CS}}$ describes the interaction of the nuclear angular moment with the surrounding electron distribution (chemical shielding). In general, all three parameters ξ, δ, and η of the chemical shielding tensor $\mathbf{R}^{\mathrm{CS}}$ are non-zero. ξ is also called chemical shift δ^{iso} and is one of the most important measurable quantities in NMR spectroscopy due to its high sensitivity to changes in the electronic environment. The secular part of $\mathscr{H}^{\mathrm{CS}}$ given in spherical coordinates shows that the chemical shielding exhibits an angular dependence which is measurable by solid-state NMR spectroscopy [Haeberlen, 1976].

$$\mathscr{H}^{CS} = \hbar\gamma_1 B_0 \left\{\delta^{iso} + \delta\left[{}^{1}/_{2}\left(1 - 3\cos^2\theta\right) + {}^{1}/_{2}\eta\sin^2\theta\cos 2\alpha\right]\right\}\mathbf{I}_{\mathrm{z}} \tag{2.13}$$

The inverse values of the three principal values $R^{\mathrm{CS}}_{\mathrm{xx}}$, $R^{\mathrm{CS}}_{\mathrm{yy}}$ and $R^{\mathrm{CS}}_{\mathrm{zz}}$ of $\mathbf{R}^{\mathrm{CS}}$ define an ellipsoid. θ is the angle between the z-axis of the ellipsoid and the direction of the external magnetic field

B_0 whereas α specifies the angle between the x-axis of the ellipsoid before and after rotation around the z-axis of the ellipsoid.

2.2.2 Quadrupolar Interaction

Spin 1/2 nuclei only possess magnetic dipole moments. All electric as well as magnetic multipole moments of higher order are zero. Nuclei with spin ≥ 1 exhibit a quadrupole moment Q which is responsible for the electric quadrupolar interaction with an electric field gradient **V**. **V** is a traceless quantity and possess a non-zero asymmetry paramter η. The secular part of the hamiltonian is given by [Man, 1996] [Vega, 1996]

$$\mathscr{H}^{\mathrm{Q}} = \frac{C}{4I(2I-1)}\left[{}^{1}\!/_{2}\left(1-3\cos^2\theta\right) + {}^{1}\!/_{2}\eta\sin^2\theta\cos 2\alpha\right]\left[3I_{\mathrm{z}}^2 - I(I+1)\right] \tag{2.14}$$

C is the quadrupolar coupling constant. Equation 2.14 only holds for the limit of small coupling constants C compared to the Zeeman interaction. Higher non-secular terms have to be considered for large values of C.

2.2.3 Direct Dipolar Interaction

The hamiltonian $\mathscr{H}^{\mathrm{D}}$ of direct dipolar interactions between nuclear spins **I** and **S** is constructed according to the correspondence principle of two classically interacting dipoles. It provides valuable structural information due to its distance dependence r^{-3} and is one of the main pathes for polarization transfer and relaxation. The dipolar coupling tensor $\mathbf{R}^{\mathrm{D}}$ is inherently traceless and symmetric without asymmetry: $\xi = 0$, $\delta = r^{-3}$, and $\eta = 0$. In the PAS of the dipolar interaction only the spherical component $\rho_{20} = \sqrt{3/2}\, r^{-3}$ is non-zero. Transformation into the LAB frame using (2.11) and (2.12) and taking into account that T_{20} give different secular contributions for $\mathbf{I} = \mathbf{S}$ (homonuclear case) and $\mathbf{I} \neq \mathbf{S}$ (heteronuclear case) results in the following secular parts of the direct magnetic dipolar interaction:

Direct homonuclear dipolar interaction [Haeberlen, 1976]:

$$\mathscr{H}^{\mathrm{D}} = -\frac{\mu_0\,\hbar\,\gamma_{\mathrm{I}}^2}{4\,\pi\,r^3}\cdot {}^{1}\!/_{2}\left(1-3\cos^2\theta\right)\cdot\left(3\mathbf{I}_{\mathrm{z}}\mathbf{I}_{\mathrm{z}} - \mathbf{I}\mathbf{I}\right) \tag{2.15}$$

Direct heteronuclear dipolar interaction:

$$\mathscr{H}^{\mathrm{D}} = -\frac{\mu_0\, \hbar\, \gamma_{\mathrm{I}}\, \gamma_{\mathrm{S}}}{4\, \pi\, r^3} \cdot {}^1\!/_2 \left(1 - 3\cos^2\theta\right) \cdot (\mathbf{I}_z \mathbf{S}_{\mathrm{z}}) \tag{2.16}$$

θ denotes the angle between the internuclear vector of two coupling spins and the static magnetic field B_0. $\frac{\mu_0 \hbar \gamma_{\mathrm{I}} \gamma_{\mathrm{S}}}{4\pi r^3} = d$ is called dipolar coupling constant.

2.2.4 Indirect Spin-Spin Interaction

The indirect spin-spin interaction (J-coupling) is a dipole coupling mediated via the electrons involved in the chemical bond. It gives rise to the splitting of NMR signals and is used to identify the binding state of atoms. Furthermore, it is used and to accomplish polarization transfer. Formally it has the same mathematical structure as the direct dipolar coupling. In contrast to the dipolar coupling hamiltonian $\mathscr{H}^{\mathrm{D}}$, however, it has an isotropic part $\xi \neq 0$ which is called scalar coupling constant $\mathrm{J}^{\mathrm{iso}}$. All three parameters ξ, δ, and η contribute to the J-coupling tensor $\mathbf{R}^{\mathrm{J}}$. Corresponding to the direct dipolar coupling, homonuclear and heteronuclear secular J-coupling Hamiltonians exhibit a different structure in the LAB frame [Smith, 1992a] [Smith, 1992b].

Indirect homonuclear dipolar coupling:

$$\mathscr{H}^{\mathrm{J}} = \mathrm{J}^{\mathrm{iso}}\mathbf{II} + \left\{ {}^1\!/_4 \left(1 - 3\cos^2\theta\right) + {}^1\!/_4 \eta\, \delta \sin^2\theta \cos 2\alpha \right\} \left(3\mathbf{I}_{\mathrm{z}}\mathbf{I}_{\mathrm{z}} - \mathbf{II}\right) \tag{2.17}$$

Indirect heteronuclear dipolar coupling:

$$\mathscr{H}^{\mathrm{J}} = \mathrm{J}^{\mathrm{iso}}\mathbf{I}_{\mathrm{z}}\mathbf{S}_{\mathrm{z}} + \left\{ {}^1\!/_4 \left(1 - 3\cos^2\theta\right) + {}^1\!/_4 \eta\, \delta \sin^2\theta \cos 2\alpha \right\} \left(\mathbf{I}_{\mathrm{z}}\mathbf{S}_{\mathrm{z}}\right) \tag{2.18}$$

The angles are defined similarly as in case of the chemical shift hamiltonian. The J-coupling is often covered and truncated by other, stronger interactions in solid-state NMR spectroscopy. In many cases, the J-coupling is, therefore, neglected.

2.3 High Resolution Solid-State NMR Spectroscopy

Spectral resolution and sensitivity are a prerequisite to obtain the desired information from NMR spectra in many cases. However, large anisotropic interactions present in solid-state lead to severe line broadenings which complicate or make it even impossible to extract this information. In this chapter, different experimental techniques are reviewed which are routinely used to overcome these interactions. Figure 2-1 demonstrates the stepwise improvement in sensitivity and resolution obtained for the ^{31}P NMR signal of *O*-phospho-L-tyrosine by applying high resolution solid-state NMR techniques.

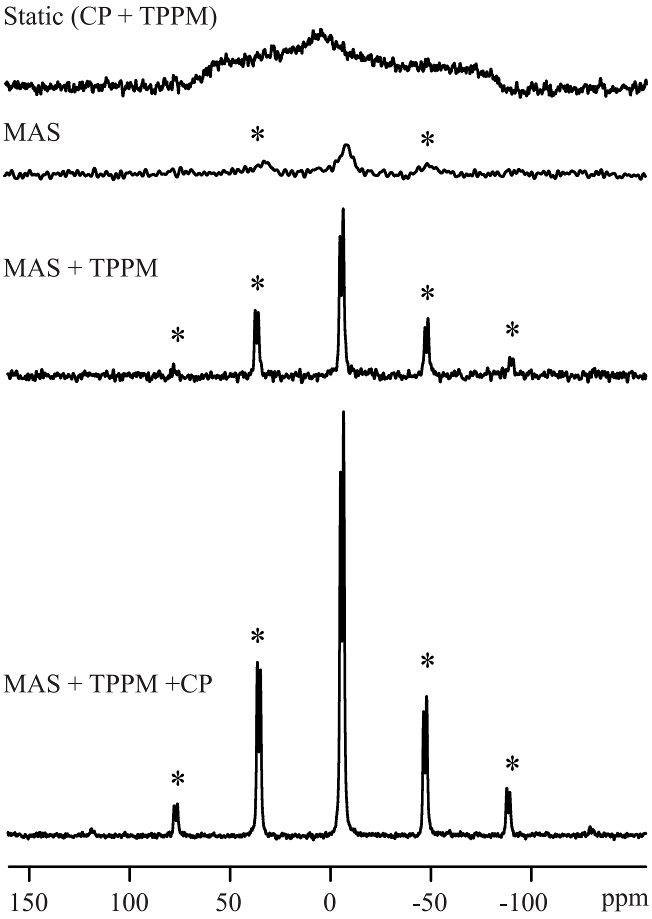

Figure 2-1
Experimental ^{31}P solid-state NMR spectra of *O*-phospho-L-tyrosine measured at B_0 = 7.05 T. From top to bottom: Static spectrum measured using CP and heteronuclear TPPM decoupling; MAS NMR spectrum acquired without CP and heteronuclear decoupling; MAS NMR spectrum measured without CP but under heteronuclear TPPM decoupling; MAS NMR spectrum acquired with CP and heteronuclear TPPM decoupling. Taken from [Iuga, 2007].

2.3.1 Magic Angle Spinning

The molecules in isotropic liquids reorient rapidly. The complete reorientation of a water molecule on average requires ca. 10^{-11} s which results in a linewidth of ca. 0.1 Hz in the ^{1}H NMR spectrum [Hennel, 2005]. On the other hand, a static sample of ice exhibits a linewidth of ca. 100 kHz. In isotropic liquids with small molecules, all anisotropic nuclear interactions are averaged out by the molecular motion because these interactions are strongly dependent on their molecular orientation in the external magnetic field B_0. The reorientation of the molecules affects the ”spatial part” of the nuclear interactions denoted as **R** in the theoretical description of the NMR Hamiltonian (see Chapter 2.1). In general, it can be written as a second-rank Cartesian tensor but it can also be expressed as sum of an isotropic part and a Legendre polynominal $P_2(\theta)$ of second order if the size of the interaction allows a treatment in first order perturbation theory [Mehring, 1983]:

$$P(\theta) \sim (1 - 3\cos^2\theta) \tag{2.19}$$

θ is the angle between the static magnetic field B_0 and a vector $\vec{r}$ describing a certain property of the nuclear magnetic interaction. In the case of direct dipolar interaction, θ is the angle between the static magnetic field B_0 and the internuclear vector of the two coupled spins. If a molecule reorients rapidly and isotropically, the term $(1 - 3\cos^2\theta)$ can be replaced by the average

$$\int (1 - 3\cos^2\theta) d\Omega \tag{2.20}$$

which is zero. $d\Omega = \sin\theta d\theta d\phi$ is the element of the solid angle. That means, rapid molecular reorientation removes the anisotropic interactions and only the isotropic part of the interaction remains. A similar result can be obtained in monocrystalline solids by orienting the sample such that $(1 - 3\cos^2\theta) = 0$, i.e., $\theta = \arccos(1/\sqrt{3}) = 54.74^\circ$ with respect to the external magnetic field. However, this angle can not be adjusted for all dipolar couplings in a monocrystal or all molecules in a powder sample.
Andrew et al. [1958a] [1958b] and, independently, Lowe [1982] had the idea to replace the random motion of molecules in liquids by a macroscopic sample spinning in case of rigid solids. The maximum line narrowing effect is achieved if the angle Θ, which is the angle between the external magnetic field B_0 and the sample spinning axis, is set to the "magic angle" $\Theta_\mathrm{m} = 54.74^\circ$. The term "magic-angle" spinning was coined by Professor Gorter (Leiden) when he heard about the method at the Ampere Congress in Pisa in 1960 for the first time [Hennel, 2005]. For this angle, all nuclear interactions which can be described by a Legendre polynominal $P_2(\theta)$ disappear [Hennel, 2005]. This can be understood as follows: Using the cosine theorem of spherical trigonometry and taking the time average over one sample spinning period, $P_2(\theta)$ can be replaced by the average value:

$$\overline{(1 - 3\cos^2\theta)} = 1/2(3\cos^2\Theta - 1)(3\cos^2\beta - 1) \tag{2.21}$$

A explanation of the angles used in equation 2.21 is given in Figure 2-2.

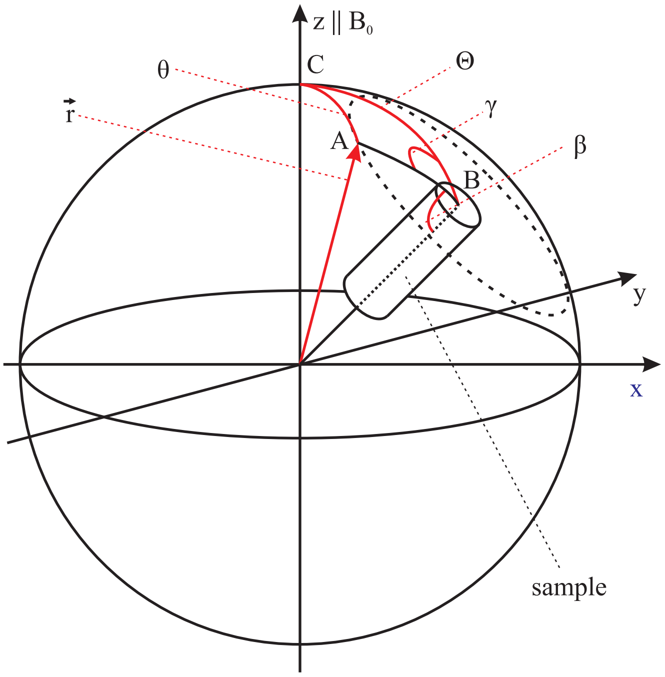

Figure 2-2
Definition of the angles and vectors used in this chapter for the case of a direct dipolar interaction. $\vec{r}$: internuclear vector of two coupling nuclei, θ: time dependent angle between the internuclear vector $\vec{r}$ and the static magnetic field B_0, Θ: constant angle between the sample spinning axis and the static magnetic field B_0, γ: time dependent angle by rotating the sample around sample spinning axis, β: constant angle between the sample spinning axis and the spherical triangle ABC.

If a NMR signal is solely broadened by inhomogeneous interactions [Maricq, 1979] such as heteronuclear direct dipole interactions or chemical shift anisotropy, MAS leads to a MAS NMR signal consisting of a narrow central line and spinning sidebands separated from the central line by multiples of the sample spinning rate in the spectrum. For homogeneous interactions [Maricq, 1979] such as the homonuclear magnetic dipolar interactions, the situation is more complicated. In the case of isolated systems of two magnetically equivalent spins (homonuclear two-spin system) the residual broadening vanishes even for slow sample spinning rates ν_r as in the case of the inhomogeneous interactions. In contrast, the centerline as well as the spinning sidebands exhibit a residual linewidth if more than two spins are present in a non-linear geometry depending on the sample spinning rate [Brunner, 1990a] [Brunner, 1990b]. The residual linewidth can be further reduced by increasing the sample spinning rate or by applying special decoupling techniques (see Chapter 2.3.2 and 2.3.3).

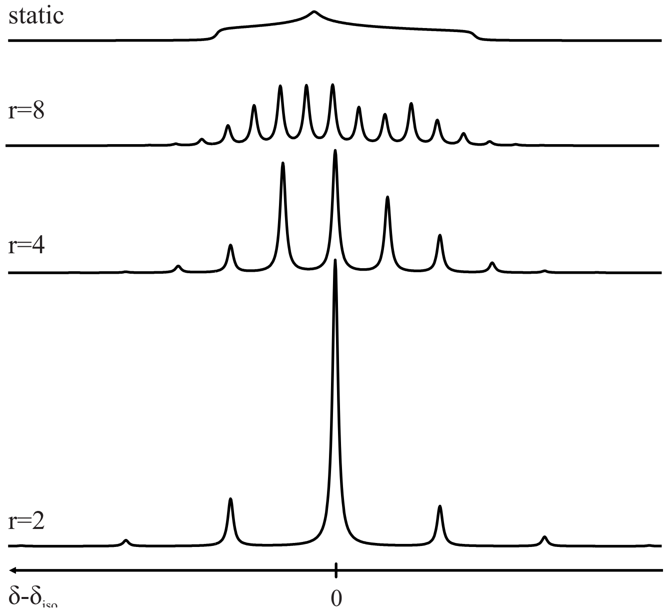

Figure 2-3
Calculated MAS NMR spectra of an CSA-broadened signal for various ratios $r = (\delta\gamma_I B_0)/(2\pi\nu_r)$. The centerline is placed at $\delta - \delta_{\text{iso}} = 0$. The other signals are spinning sidebands. The residual linewidth originates from the used convolution function. Taken from [Iuga, 2007].

2.3.2 Heteronuclear Decoupling

Heteronuclear spin decoupling in liquid-state NMR spectroscopy is routinely applied by using multiple pulse decoupling techniques. In liquid-state NMR spectroscopy, molecular reorientation removes most of the magnetic spin-spin interactions, only leaving the J-coupling as a main source of line splitting. In many cases, the residual linewidth in liquid-state NMR spectra is only limited by relaxation mechanisms. In solids, the situation is different. Not only J-couplings have to be considered but also the anisotropic heteronuclear dipolar couplings which are, in many cases, several orders of magnitude larger than the J-couplings. Hetronuclear decoupling under MAS conditions poses several problems. Anisotropic heteronuclear dipolar couplings become time dependent under MAS [Ernst, 2003]. An additional time dependence due to RF irradiation can lead to interference effects between both techniques. Such interferences may result in undesired recoupling effects, i.e., in a significant line broadening [Ernst, 2003, and references therein]. This effect is demonstrated in Figure 2-4.

A strong homonuclear dipolar coupling network can also affect the efficiency of heteronuclear decoupling techniques. The homonuclear dipolar Hamiltonian does not commute with itself at different times under MAS conditions and does also not commute with the heteronuclear coupling. Therefore, residual cross terms between the heteronuclear dipolar couplings with the homonuclear coupling as well as the chemical shift anisotropy lead to an incomplete averaging of the heteronuclear dipolar couplings [Ernst, 2003]. For many years high power continuous wave (CW) decoupling was the routinely applied method in order to achieve heteronuclear decoupling in solid-state NMR spectroscopy [Schmidt-Rohr, 1999] [Ernst, 2003]. CW decoupling involves a continuous irradiation of the decoupling spins with high RF power (see Figure 2-5).

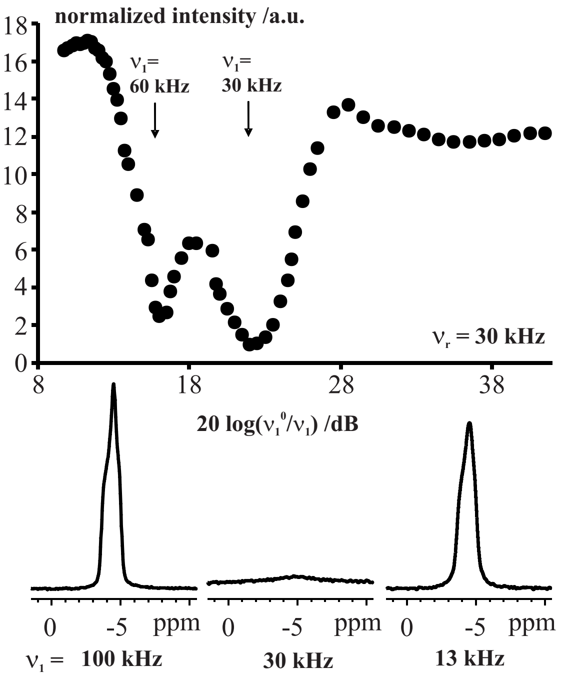

Figure 2-4
Intensity of the $^{31}P\{^{1}H\}$ CP MAS NMR signal (peak maximum) of *O*-phospho-L-threonine in arbitrary units (a.u.) measured at B_0 = 7.05 T as a function of the decoupling field strength ν_1 (in frequency units). ν_1^0 = 180 kHz corresponds to the maximum decoupling field strength obtained at 6 dB damping. The pronounced influence of rotational resonance upon the linewidth is demonstrated in the spectra at the bottom. Taken from [Iuga, 2007].

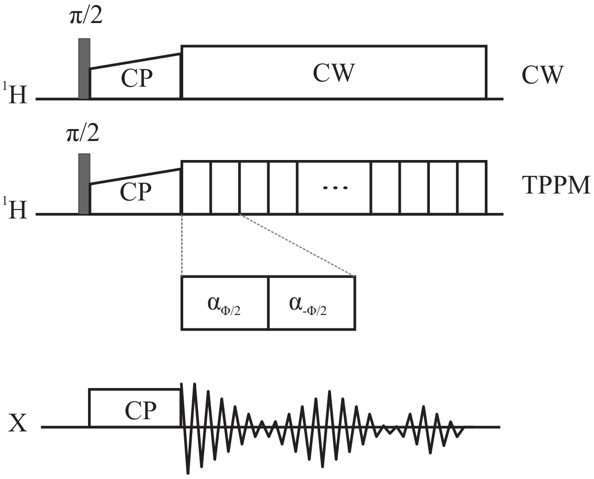

Figure 2-5
CW and TPPM [Bennett, 1995] decoupling pulse schemes in combination with a common CPMAS experiment (see Chapter 2.3.4).

Today, the most frequently applied decoupling sequence is two-pulse phase-modulated (TPPM) decoupling [Bennett, 1995] (see Figure 2-5) which further reduces the linewidth compared to CW. In addition, lower RF powers are sufficient. As in case of CW, TPPM also comprises a windowless irradiation. The basic element of TPPM comprises two pulses of equal flip angle α, close to π, but with a phase difference $\Delta\Phi$. Both parameters have to be experimentally optimized. Two further developments of the TPPM experiment are the XiX [Detken, 2002] and the SPINAL [Fung, 2000] pulse scheme offering several advantages over TPPM in special cases.

2.3.3 Homonuclear Lee-Goldburg Decoupling

^{1}H solid-state NMR spectroscopy of organic compounds remains to be a challenging task. Severe line broadening up to 100 kHz caused by homonuclear dipolar coupling networks, e.g., ^{1}H nuclei results in poorly resolved spectra. This broadening can only be overcome by MAS by sample spinning rates much higher than the strength of the dipole-dipole interactions. Commercially available probes allow sample spinning rates at up to 70 kHz which is not sufficient to remove these interactions completely. Additional line narrowing can, in general, be obtained by the application of CRAMPS (Combined Rotation And Multiple Pulse Spectroscopy [Gerstein, 1996]) techniques. The first experiment of this type was the WAHUHA cycle developed by Waugh, Huber, and Haeberlen [Waugh, 1968a] [Waugh, 1968b] [Haeberlen, 1968]. Many improved pulse sequences were developed on the basis of the WAHUHA theory (see, e.g., [Schmidt-Rohr, 1999]). The application of such multiple pulse sequences usually requires cycle times which are short compared to the rotor periods which is not feasible for high sample spinning rates. Another approach was proposed by Lee and Goldburg [Lee, 1965]. It involves a continuous windowless application of a RF field ω_1 with a resonance offset ΔLG according to the Lee-Goldburg (LG) condition

$$|\Delta LG| = \frac{1}{\sqrt{2}}\omega_1 \tag{2.22}$$

which produces an effective field ω_{eff} in the rotating frame inclined at the magic angle $\theta_m = \tan^{-1}(\sqrt{2})$. The magnetic vector M rapidly precesses around the effective field ω_{eff} (see Figure 2-6) resulting in a cancelation of the secular parts of the direct dipolar coupling interaction. The duration t_{LG} for a full 2π cylce of the magnetic vector M around the effective field ω_{eff} is

$$t_{\mathrm{LG}} = \sqrt{\frac{2}{3}}\frac{2\pi}{\omega_1} \tag{2.23}$$

which can be set to a short value by applying high fields ω_1. Therefore, these kinds of experiments can also be performed under fast sample spinning. Note that resonance between the sample spinning rate and the LG frequnecy has to be avoided.

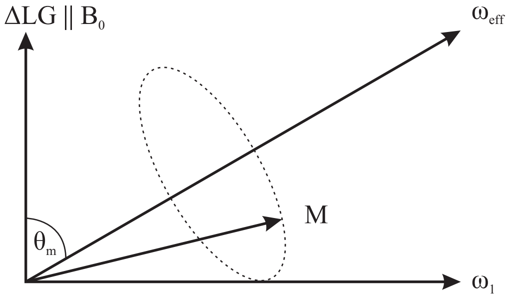

Figure 2-6
Nutation of the magnetization vector M around the effective field ω_{eff} under Lee-Goldburg irradiation in the rotating frame.

Two improved LG variants are presented in the following which were applied within this work. It has been shown by Levitt and coworkers that the efficiency of the decoupling is significantly improved if the LG irradiation is both frequency- and phase-switched after a complete rotation (2π) of the magnetization around the effective field ω_{eff} (FSLG) [Bielecki, 1989] [Bielecki, 1990]. The frequency is switched between the two LG conditions $\pm\Delta\text{LG}$ and simultaneously phase shifted after a full rotation period t_{LG}. A further improvement can be achieved by placing the magnetization perpendicular to the effective field ω_{eff} [van Rossum, 1997]. The pulse scheme is represented in Figure 2-7. The other variant was developed in the Vega group and is called phase-modulated Lee-Goldburg (PMLG) [Vinogradov, 1999]. An inspection of equation 2.22 and 2.23 shows that the precession angle α_{LG} of the RF-field in the rotating frame during t_{LG} is given by

$$\alpha_{\text{LG}} = |\Delta LG| \cdot t_{\text{LG}} = 207.8^\circ \tag{2.24}$$

Vinogradov *et al.* [Vinogradov, 1999] showed that this behavior can be simulated by a stepwise phase shift of the irradiated field ω_1. A full PMLG cycle consists of 18 pulses of duration $2t_{\text{LG}}/18$ (see Figure 2-7). The phase θ_{LG} of the first pulse is $\theta_{\text{LG}} = 0$. The increment in phase angle $\Delta\alpha$ of each successive pulse is $\Delta\alpha = 207.8^\circ/9$ (x in Figure 2-7). After 9 pulses, the LG condition is changed from $+\Delta\text{LG}$ to $-\Delta\text{LG}$ and the phase is simultaneously switched by 180°. The next pulses are again phase incremented until a full PMLG cycle is compete (-x in Figure 2-7). LG sequences can be implemented in different solid-state NMR experiments in order to achieve highly resolved ^{1}H spectra. In case of 1D ^{1}H spectra, PMLG or FMLG is applied between the FID acquisition points [Vinogradov, 2002] [Levitt, 1993]. PMLG or FMLG can also be performed in 2D HETeronuclear CORrelation (HETCOR) experiments during t_1 in order to increase the resolution in the indirect dimension and prevent spin diffusion [Vinogradov, 1999] [van Rossum, 1997]. It has to be considered that the dispersion of the ^{1}H dimension in 1D and 2D LG-experiments is scaled by the factor $\cos\theta = 1/\sqrt{3}$.

The performance of a CP experiment can also be optimized by spin locking the magnetization using a LG sequence [Fu, 2004]. It was shown that the so called LG-FMCP polarization transfer increases the ^{1}H spin-lattice relaxation times and simultaneously decreases the cross polarization times of non-protonated spins. Both effects are advantageous.

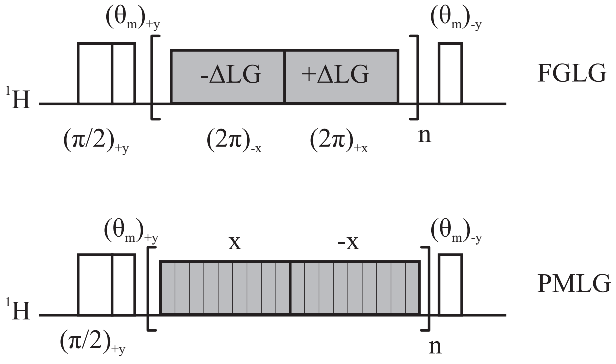

Figure 2-7
Pulse sequences of FSLG [van Rossum, 1997] and PMLG [Vinogradov, 1999].

2.3.4 Cross Polarization

Owing to the strong homonuclear couplings between ^{1}H nuclei in organic solids and the resulting broad linewidth, rare nuclei such as ^{13}C, ^{29}Si and ^{31}P are often directly detected in solid-state NMR spectroscopy rather than ^{1}H nuclei. Two specific disadvantages are associated with the NMR spectroscopy of dilute nuclei compared to ^{1}H nuclei, mainly their low sensitivity and long relaxation times. Both drawbacks can be overcome by performing cross polarization (CP) experiments. This method was first proposed by Hartmann and Hahn [1962] and was established by Pines *et al.* [1972] [1973]. The experiment is based on a polarization transfer from abundant nuclei (I) with a high gyromagnetic ratio to dilute spins (S) via the direct heteronuclear dipolar coupling. Figure 2-8 shows different pulse sequences for the standard 1D CP experiment. The I spins, in most cases ^{1}H nuclei, serve as polarization source. They are excited by a pulse, usually $\pi/2$. In the following, both spins are spin locked in the transverse plane of the rotating frame by a simultaneous radio frequency irradiation during the contact period τ_{CP}. Hartmann and Hahn [1962] showed that a polarization transfer process between both nuclei could be established if the precession frequencies ω_{I} and ω_{S} of both spins I and S are matched to each other by adjusting the power ratio $B_{\mathrm{rf,I}}/B_{\mathrm{rf,S}}$. This matching condition is known as Hartmann-Hahn condition:

$$\omega_{\mathrm{I}} = \gamma_{\mathrm{I}} B_{\mathrm{rf,I}} = \gamma_{\mathrm{S}} B_{\mathrm{rf,S}} = \omega_{\mathrm{S}} \tag{2.25}$$

If this condition is fulfilled, a polarization transfer between both spins is possible due to a mutual flip-flop process of the involved spin pairs I–S. In this context it is important to note that the cross polarization process is not a matter of spin diffusion because it was shown that the polarization can be transferred back to the I spins by an echo [Ernst, 1998]. The maximal sensitivity enhancement for the CP experiment is given by the ratio $\gamma_{\mathrm{I}}/\gamma_{\mathrm{S}}$. Further sensitivity gain is achieved by the possibility of faster pulsing because the relaxation delay in CP experiments between consecutive scans is limited by the – in most cases significantly shorter – T_1 relaxation time of the abundant nuclei.

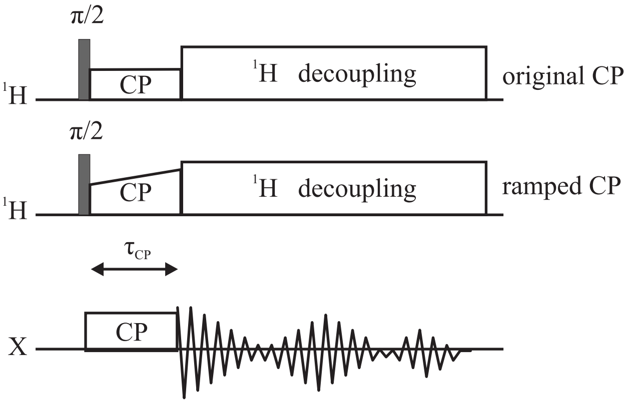

Figure 2-8
Pulse sequence of the standard 1D CP experiment (top ^{1}H channel) [Pines, 1972] [Pines, 1973] and of the ramped CP experiment (bottom ^{1}H channel) [Metz, 1994].

The combination of CP and MAS (CPMAS [Schaefer, 1976]) has become a standard technique for obtaining high resolution spectra in solid-state NMR spectroscopy. As it is discussed above, the efficiency of the CP critically depends on the matching of the Hartmann-Hahn condition. Owing to dipolar broadenings the Hartmann-Hahn matching profile is very broad for a static sample. However, if the sample spinning rate is of the order of the dipolar couplings between I–I and I–S, respectively, the Hartmann-Hahn condition breaks down into a series of matching sidebands $\omega_{\Delta(\mathrm{n})}$ separated by the sample spinning rate ν_{r}:

$$\omega_{\Delta(\mathrm{n})} = \omega_{\mathrm{S}} - \omega_{\mathrm{I}} = 2\pi \cdot n \cdot \nu_{\mathrm{r}} \tag{2.26}$$

An efficient CP is only obtained for $n = \pm 1, \pm 2$. In this case, it is difficult to adjust and maintain an optimum Hartmann-Hahn match for the magnetization transfer. However, several techniques have been developed to optimize CP under MAS conditions. One of the most frequently applied techniques is the ramped-amplitude CP MAS NMR experiment depicted in Figure 2-8 [Metz, 1994]. In this case $B_{\mathrm{rf,I}}$ is not kept constant but the field is varied (ramped) such that the field passes through the matching condition.

The CP experiment can be extended to a 2D HETCOR experiment by introducing an additional spin evolution time before the CP period [Schmidt-Rohr, 1999].

2.4 Spin Diffusion Experiments

2.4.1 The NOESY-Experiment - ^{1}H Driven Spin Diffusion

The aim of a 2D Nuclear Overhauser Effect SpectroscopY (NOESY) experiment is the identification of neighboring spins by measuring cross-relaxation. The 2D pulse sequence for the 2D NOESY experiment in solution was developed by Ernst and coworkers [Jeener, 1979]. A solid-state version of this experiment was introduced by Szeverenyi *et al.* [1982]. The corresponding pulse sequence is shown in Figure 2-9. In this experiment, the transverse magnetization of the dilute spins X is created by cross polarization from the abundant ^{1}H nuclei. In the case of inorganic compounds as in Chapter 4, the initial magnetization of the X spins can be prepared by a $\pi/2$ pulse. After excitation, the X spins are allowed to evolve during t_1. Throughout this evolution period, ^{1}H decoupling is applied and MAS is simultaneously performed during the whole experiment leaving only the chemical shift interaction. Therefore, the X spins become frequency labeled during this time. The following $\pi/2$ pulse rotates the magnetization along the z-axis. During the mixing time τ_{mix}, ^{1}H decoupling is switched off which allows ^{1}H-driven spin diffusion processes. Owing to the r^{-6} distance dependence of the spin diffusion rate of rare spins, the spin diffusion process is restricted to closley neighbored nuclei (3-5 Å distance) [Schmidt-Rohr, 1999]. The transition probability $P_{\mathrm{AB}}(t)$ for the spin diffusion process of the rare spins A and B with corresponding Larmor frequencies ω_{A} and ω_{B} is given by [Schmidt-Rohr, 1999]

$$P_{\mathrm{AB}}(t) = \frac{1}{2}\pi\, g_0^{\mathrm{AB}}(\Delta\omega_{\mathrm{AB}})\, \omega_{\mathrm{D}}^2 t. \tag{2.27}$$

In this equation which was derived from Fermi's golden rule, ω_{D} is the homonuclear dipolar coupling frequency of two neighboring spins A and B, $\Delta\omega_{\mathrm{AB}}$ denotes the chemical shift difference $\omega_{\mathrm{A}} - \omega_{\mathrm{B}}$ of the two spins and $g_0^{\mathrm{AB}}(\Delta\omega_{\mathrm{AB}})$ is the zero-quantum transition lineshape function of the participating spins. In case of high resolution solid-state NMR spectroscopy under fast MAS, g_0^{AB} is predominantly governed by the heteronuclear dipolar interactions to neighboring protons. Therefore ^{1}H decoupling is switched off during the mixing time and heteronuclear dipolar interaction can compensate the chemical shift difference $\Delta\omega_{\mathrm{AB}}$. In this manner, the ^{1}H nuclei "drive" the spin diffusion process. However, the spin diffusion directly takes place through space between the rare X nuclei and not via the ^{1}H nuclei. The second $\pi/2$ pulse converts the longitudinal magnetization back into observable transverse magnetization which is detected under ^{1}H decoupling in the following acquisition period t_2. A proper phase cycle has to be applied in order to suppress any signals which do not originate from the longitudinal magnetization present during the mixing time [Levitt, 2000].

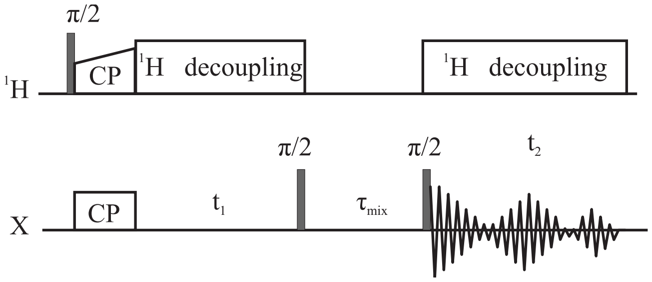

Figure 2-9
Pulse sequence of the 2D NOESY experiment as proposed by Szenerenyi *et al.* [1982].

Nuclei without spin diffusion provide only diagonal peaks. Any spin diffusion process that couples different resonance frequencies will manifest itself by off-diagonal / cross peaks in the spectrum. The integrated area of the cross peaks is proportional to the distance of the involved nuclei and is routinely used in structure determination to determine the structure of proteins [Cavanagh, 1996]. Also correlation due to spatial reorientation will give rise to off diagonal peaks. These signals can not be distinguished from those originated in spin diffusion processes, in many cases. Additionally, the mixing time τ_{mix} should be synchronized with the sample spinning rate in order to avoid artefacts due to reorientation of the rotor.

2.4.2 Radio Frequency Driven NOESY-Type Experiments

The zero-quantum transition lineshape function $g_0^{\mathrm{AB}}(\Delta\omega_{\mathrm{AB}})$ in equation 2.27 is the bottleneck of the ordinary ^{1}H driven NOESY experiment discussed above. The effect of the chemical shift differences can be removed by means of special experimental techniques such as spin locking

of the rare spins in the x/y plane (ROESY experiment [Levitt, 2000]).
In case of dilute spin systems under fast MAS, ω_D may be the limiting factor. The averaging effects of MAS can be overcome by applying a sequence of π pulses synchronized with the sample spinning rate during the longitudinal mixing time of experiment (Radio Frequency-driven Dipolar Recoupling, RFDR). This pulse scheme results in a reintroduction of the flip-flop term of the dipolar coupling even in the presence of chemical shift differences and fast MAS. The pulse sequence was first proposed by Bennett *et al.* [1992] [1998] and is depicted in Figure 2-10.

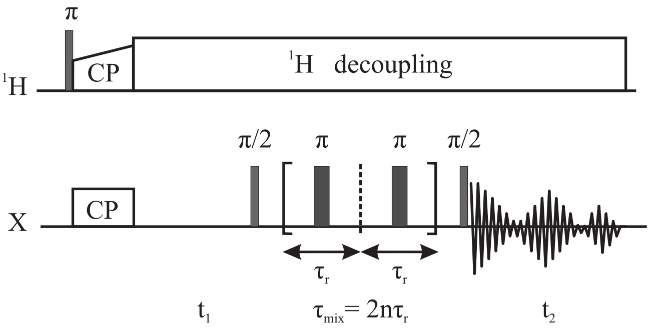

Figure 2-10
Pulse sequence of the 2D RFDR-NOESY experiment developed by Bennett *et al.* [1992]. A pulse train of 2n π-pulses is applied synchrous with the sample spinning rate $\nu_r = 1/\tau_R$ during the longitudinal mixing time.

Besides the RFDR zero-quantum recoupling technique, a multitude of other recoupling methods were developed (see, e.g., POST-C7 in section 2.5.2). However, RFDR has the advantage of its robustness against chemical shift differences and its low demand of receiver power. However, a severe drawback is given by the fact that the compensation of pulse and phase errors requires at least 8-fold phase cycling such that the recoupling period may become relatively long.

2.4.3 The R-TOBSY Experiment – J-Coupling Driven Spin Diffusion

In solid-state NMR, correlations between different nuclei are routinely probed using dipole-dipole interactions. Usually, J-couplings are truncated since they are much weaker than the dipole-dipole couplings. Nevertheless, J-coupling mediated experiments are very important due to their exclusive selectivity which is provided by the through bond interaction. Until now, only a limited number of solid-state MAS NMR techniques exists allowing to exclusively detect the J-coupling (e.g. TOBSY [Baldus, 1996] [Baldus, 1997] and INADEQUATE [Lesage, 1999]). Another promising approach is delivered by the so-called R-symmetry pulse sequences introduces by Levitt and coworkers [Carravetta, 2000] [Brinkmann, 2001] [Levitt, 2002]. Based on these principles, Brunklaus [2003b] [Chan, 2001] developed a pulse sequence driving homonuclear polarization transfer by the J-coupling with high efficiency. The experiment is constructed like a NOESY experiment (see Section 2.4.1). In contrast to the common NOESY experiment, a special homonuclear decoupling sequence – the $R30_6^{14}$ symmetry based pulse scheme – is implemented during the mixing period (see Figure 2-11).

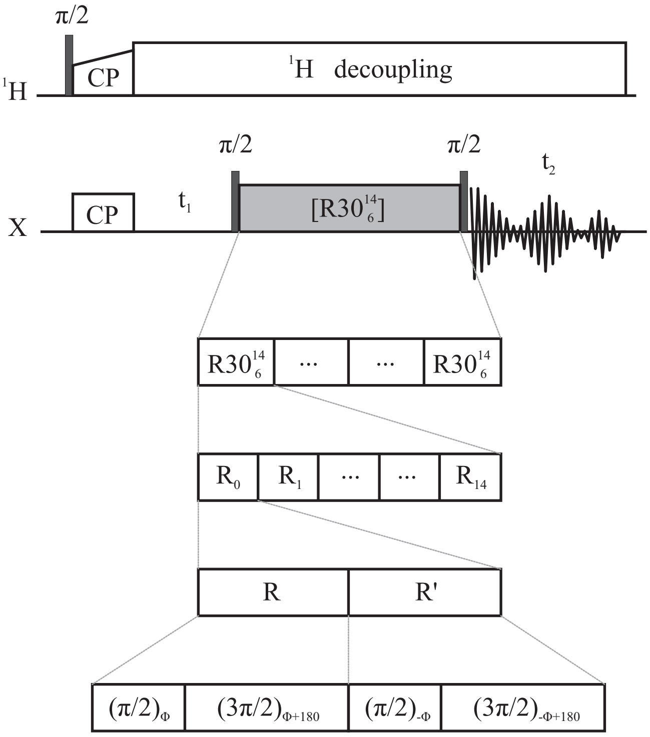

Figure 2-11
Pulse sequence of the 2D R-TOBSY experiment developed by Brunklaus [2003b] [Chan, 2001].

The mixing period consists of a train of $R30_6^{14}$ elements. Each $R30_6^{14}$ element consists of 15 R_i elements which again contain a basic R element and a phase shifted R' element. The R element rotates the spins by 180° around the x-axis. Therefore, R is equal to a single π pulse or, as is applied in the present work, a composite π pulse: R$=(\pi/2)_\phi(3\pi/2)_{\phi+180^\circ}$. The R' is also a composite π pulse but all phases possess a change in sign compared with the R element: R'$=(\pi/2)_{-\phi}(3\pi/2)_{-\phi+180^\circ}$. The ω_1 amplitude of the applied RF-field during the mixing time has to be tuned such that 30 R elements (of duration τ_R) exactly fill 6 rotor periods τ_r:

$$30\tau_R = 6\tau_r \tag{2.28}$$

This implies that the required RF-frequency ω_1 is five times the sample spinning rate. The $R30_6^{14}$ sequence consists of 15 pairs of elements $R_\phi R'_{-\phi}$, where ϕ is a phase shift:

$$\phi = 14\pi/30 \tag{2.29}$$

2.5 Multi-Quantum Spectroscopy

2.5.1 The Refocused INADEQUATE Experiment

The INADEQUATE (Incredible NAtural Double abundancE QUAntum Transfer Experiment) experiment was first proposed by Bax and coworkers [Bax, 1980] [Bax, 1981] and is a routinely used technique to probe direct scalar connectivities in liquid-state NMR spectroscopy. The INADEQUATE experiment only selects nuclei that are directly bound to each other and filters any signals arising from isolated spins. In the following, only the 2D single quantum-double quantum (SQ-DQ) INADEQUATE experiment is discussed. The 1D version of this experiment – which is helpful to optimize the 2D experiment – is not described here.

In the 2D experiment, the signals of two coupled spins, A and B, occur at their common DQ frequency ω_{DQ} in the indirect dimension and are correlated with their SQ frequencies $\omega_{\mathrm{SQ}}^{\mathrm{A}}$ and $\omega_{\mathrm{SQ}}^{\mathrm{B}}$ in the direct dimension. However, this experiment yields correlations in antiphase making this experiment rather impractical in solid-state NMR spectroscopy of amorphous solids. The line width in such systems may be more than one order of magnitude higher than the J-coupling resulting in the mutual cancelation of the antiphase signals. Therefore, the original version of this experiment could only be applied to an limited number of solids such as plastic crystals and single crystals with a small line widths [Lesage, 1997, and references therein]. Lesage et al. [Lesage, 1999] [Sakellariou, 2002] developed an improved version of this experiment called refocused INADEQUATE which could successfully be applied to systems where the line width greatly exceeds the value of the scalar coupling [Lesage, 1999] [Fayon, 2002]. The pulse sequence is presented in Figure 2-12.

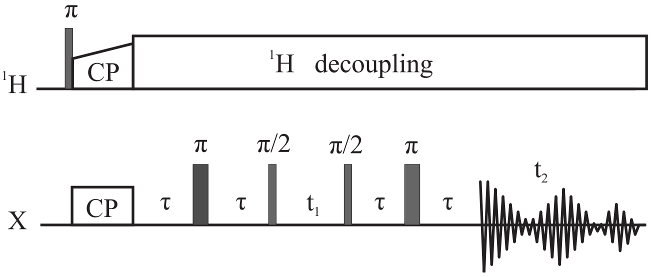

Figure 2-12
Pulse sequence of the 2D refocused INADEQUATE experiment, as proposed by Emsley and coworkers [Lesage, 1999].

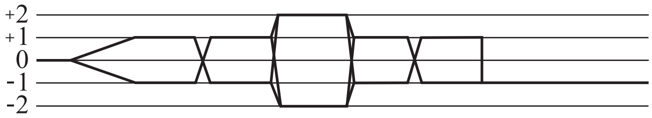

Figure 2-13
Coherence-transfer pathway diagram of the refocused INADEQUATE experiment.

The performance of the experiment depends on the fact that the J-coupling is the only transfer way for the spin diffusion process. Therefore, homonuclear dipolar interactions together with other anisotropic interactions are removed by fast MAS. At the same time, heteronuclear dipolar and scalar interactions are averaged out by heteronuclear decoupling. After CP excitation, the isotropic chemical shift is refocused by the first π-pulse. Subsequently, DQ coherence created by the first $\pi/2$ pulse evolves during t_1 at a frequency ω_{DQ} which is the sum of the SQ frequencies of the two coupled spins A and B:

$$\omega_{\mathrm{DQ}} = \omega_{\mathrm{SQ}}^{\mathrm{A}} + \omega_{\mathrm{SQ}}^{\mathrm{B}} \tag{2.30}$$

The DQ-coherence is converted back into antiphase coherence by the second $\pi/2$ pulse. Unlike the original INADEQUATE version, an extra Hahn echo period $\tau - \pi - \tau$ is introduced between t_1 and t_2 which converts the antiphase component back into an inphase signal. Phase cycles [Bodenhausen, 1984] have to be applied to the pulses and the receiver in order to filter SQ coherences and to select the the right coherence transfer pathway which is shown in Figure 2-13 [Lesage, 1999]. The efficiency of the refocused INADEQUATE experiment depends on the ratio T_2'/T_2^* where T_2^* is the apparent relaxation time determined from the line width of an ordinary 1D experiment and T_2' is the transverse dephasing time measured in a spin echo experiment. That means that the refocused INADEQUATE experiment is particularly effective for solid systems which are inhomogeneously broadened. The maximum transfer into DQ coherence occurs for $\tau = 1/(4J)$. For strongly coupled systems and signals close to the SQ-DQ diagonal in the spectrum, this condition is not fulfilled and the signals will heavily loose intensity [Buddrus, 1987]. In this case, an optimum is given for $\tau = 3/(4J)$ or $\tau = 5/(4J)$. Moreover, the τ delays should be set such that an integral number of the rotor period fits in in order to completely average out the homonuclear couplings [Sakellariou, 2002]. Signals very close to the SQ-DQ diagonal or close to rotational resonance should be analyzed very carefully. In these cases, artefacts my occur which do not originate from the presence of a J-coupling [Fayon, 2005]. Some artefacts in the spectrum can be eliminated by using composite π pulses [Lesage, 1997] or introducing an additional z-filter before t_2 [Cadars, 2007]. Another version of the INADEQUATE experiment which is also appropriate for the application in solid-state NMR spectroscopy is the INADEQUATE-CR experiment which was proposed by Verel *et al.* [Verel, 1999].

2.5.2 The POST-C7 Experiment

The POST-C7 NMR recoupling experiment [Lee, 1995] [Hohwy, 1998] belongs to the class of C-symmetry based pulse sequences developed by Levitt and coworkers [Carravetta, 2000] [Brinkmann, 2001] [Levitt, 2002] and makes use of symmetry considerations between the rotor rotation and the spin rotation. Therefore, pulse sequences of this type have to be synchronized with the sample spinning rate as well as with the RF-frequency and phase.

In the following, the experiment will be described in the context of a 2D single quantum-double quantum (SQ-DQ) experiment. This experiment is constructed as shown in Figure 2-14. Polarization of the dilute X spins can be excited by cross polarization from the protons. A $\pi/2$ pulse transforms the transverse magnetization into longitudinal magnetization. The following (POST-)C7 sequence of duration τ_{exc} converts this z-magnetization into DQ coherence which is allowed to evolve during the subsequent DQ evolution time t_1. A second (POST-)C7 pulse train of duration $\tau_{\text{rec}} = \tau_{\text{exc}}$ reconvers the DQ coherence into longitudinal magnetization. After a final $\pi/2$ pulse the FID is acquired.

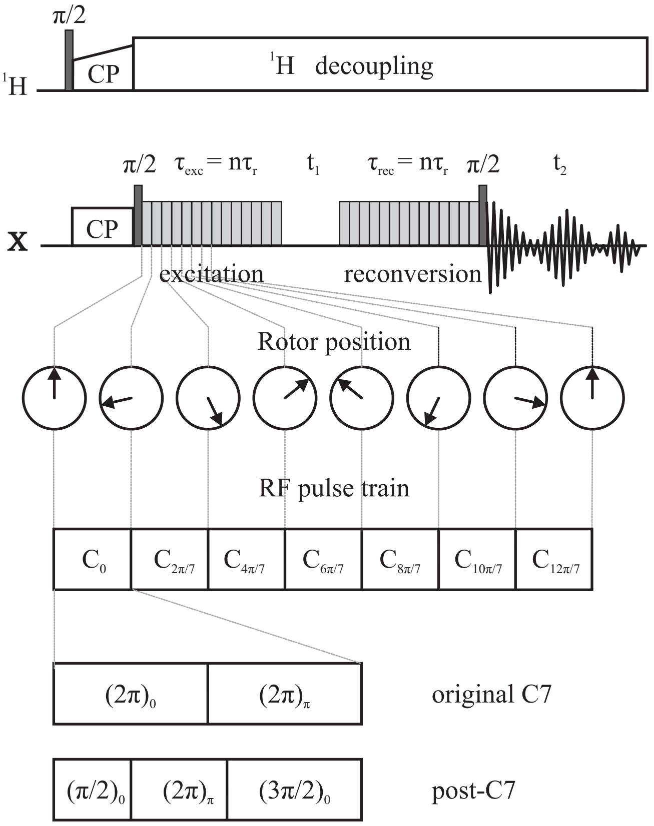

Figure 2-14
Pulse sequence of the 2D POST-C7 SQ-DQ experiment developed by Levitt and coworkers [Lee, 1995] [Hohwy, 1998].

As in case of the INADEQUATE experiment, a phase cycle has to be performed on the (POST-)C7 pulse sequence of the DQ reconversion period and the final read out pulse [Bodenhausen, 1984]. One basic (POST-)C7 sequence is timed such that one modulation cycle is exactly equal to two rotor periods $\tau_\mathrm{r} = |2\pi/\omega_\mathrm{r}|$. The (POST-)C7 sequence is composed of of seven segments C_ϕ of duration $\tau_\mathrm{c} = 2\tau_\mathrm{r}/7$. Each of these pulse segments exhibits a phase ϕ and comprises either two $(2\pi)_{(\varphi)}$ pulses with phase difference $\delta\varphi = \pi$ (original C7 [Lee, 1995]) or three pulses $(\pi/2)_{\varphi 1}$ $(2\pi)_{\varphi 2}$ $(3\pi/2)_{\varphi 1}$ with a phase difference of π between φ_1 and φ_2 (POST-C7 [Hohwy, 1998]). The latter one shows an improved tolerance toward chemical shift offsets and RF inhomogeneity. The nutation frequency of the X spins throughout the C7 pulse train has to be seven times the sample spinning rate: $\omega_\mathrm{X} = 7\omega_\mathrm{r}$. This can become a problem for high spinning frequencies because of the high RF field which can damage the probe. The DQ excitation period is build up of an integer number q of C_ϕ elements ($\tau_\mathrm{rec} = q\tau_\mathrm{c}$) with a phase shift of $\Delta\phi = 2\pi/7$ between each consecutive C_ϕ element ($\phi_\mathrm{exc} = \{0, 2\pi/7, ..., 2\pi(q-1)/7\}$). The DQ reconversion period possesses the same number and duration of C_ϕ elements. The phase cycle is continued and the additional phase γ due to DQ filtration has to be added: $\phi_\mathrm{rec} = \{2\pi q/7+\gamma, 2\pi(q+1)/7+\gamma, ..., 2\pi(2q-1)/7+\gamma\}$. During the whole experiment, ^{1}H decoupling has to be applied avoiding any resonance condition between the decoupling frequency and the used frequency for the C7 sequence.

The advantage of this kind of DQ recoupling is its high recoupling efficiency of up to 54 % and its robustness against offsets caused, e.g., by chemical shifts.

3 NMR Spectroscopic Studies on Diatoms

3.1 Biomineralization

Biomineralization, i.e., the process of formation and patterning of inorganic materials by living organisms, is a common phenomenon in nature. Biominerals often exhibit extraordinarily interesting properties from the materials science point-of-view as well as with respect to biomedical applications. Mineral deposition plays a major role in skeletal formation and biomineral deposits sometimes act as storage systems delivering ions during periods of special demand [Simkiss, 1989]. Increasing research interest is devoted to the study of the processes leading to the formation of biominerals [Addadi, 1992] [Weiner, 1997] [Mann, 2001] [Müller, 2003] [Sumper, 2006b] [Naka, 2007] [Baeuerlein, 2007] [Gröger, 2008]. On the one hand, the understanding of these genetically controlled processes is of fundamental biological interest. On the other hand, the knowledge of the biochemical and biophysical principles steering biomineralization would greatly enhance the synthetic possibilities of materials science.

Biomineralization encompasses the formation of calcium-based compounds such as calcium carbonate or hydroxyapatite, of siliceous compounds, of iron oxides, and others. Calcium carbonate is, for example, the major constituent of nacre. The bones of vertebrates contain hydroxyapatite. Apart from hydroxyapatite, fluorohydroxyapatite is found in teeth. Biogenic silica is usually formed intracellularly. It occurs in various plants (see Section 3.5) such as several grasses and sedges. Rice hulls are known to contain considerable amounts of silica. They are, therefore, supposed to be a valuable future silica source. The most beautiful and attractive examples for silica biomineralization are, however, found in microorganisms such as silicoflagellates, radiolarians, and diatoms. Owing to their ornately micro- and nanostructured cell walls, diatoms belong to the most attractive objects for microscopic studies. Biogenic silica is also found in the spicules of silica sponges. Very often, biominerals are made up of amorphous compounds or small microcrystalline domains embedded into an amorphous matrix. In most cases, organic material is incorporated which leads to composite materials with extremely interesting properties.

Mineral	Formula	Organism / Function
Calcium carbonate		
Calcite	$CaCO_3$	Algae / exoskeletons
		Trilobites / eye lens
Aragonite	$CaCO_3$	Fish / gravity device
		Molluscs / exoskeleton
Vaterite	$CaCO_3$	Ascidians / spicules
Amorphous	$CaCO_3 \cdot nH_2O$	Plants / Ca storage
Calcium phosphate		
Hydroxyapatite	$Ca_{10}(PO_4)_6(OH)_2$	Vertebrates / skeletons, teeth, Ca storage
Octacalcium phosphate	$Ca_8H_2(PO_4)_6$	Vertebrates
Amorphous	-	Mussels / Ca storage
		Vertebrates / precurser
Calcium oxalate		
Whewellite	$CaC_2O_4 \cdot H_2O$	Plants / Ca storage
Weddellite	$CaC_2O_4 \cdot 2H_2O$	Plants / Ca storage
Metal sulfates		
Gypsum	$CaSO_4$	Jellyfish larvae / gravity device
Barite	BAS_4	Algae / gravity device
Celestite	$SrSO_4$	Acantharia / cellular support
Silicon dioxide		
Silica	$SiO_2 \cdot H_2O$	Diatoms, silicoflagellates, radiolarians, sponges / exoskeletons

Table 3-1 Types and function of biominerals [Simkiss, 1989] [Weiner, 1997] [Mann, 2001].

3.2 Diatoms - General Aspects

Diatoms are unicellular, eukaryotic algae which can be found in almost every sea and fresh water habitat on earth. They are responsible for approximately 40 % of the marine primary production [Falkowski, 1998] and play a key role in the ocean's silicon cycle [Treguer, 1995]. In particular, diatoms are well-known for the intricate micro- and nano-structured patterns of their silica-based cell walls. This makes them an outstandingly interesting system for the study of silica biomineralization processes [Sumper, 2006b]. The species-specific patterns are reproduced during each cell division cycle [Zurzolo, 2001] which is closely correlated with the silicon metabolism of the cell. The silicified cell wall is called frustule. It is constructed of two almost equal halves, with the smaller fitting into the larger like a Petri dish (see Figure 3-1). The larger of the two halves is denoted the epitheca, and the inner one is denoted the hypotheca. Each theca is typically composed of two parts: the valve (which forms the larger outer surface) and a girdle (circular bands of silica attached to the edge of the valve). The characteristic patterns are precisely reproduced from generation to generation, implicating a strict genetic control of this process. The nanoscale architecture of these patterns, by far, exceeds the capabilities of recent materials science. An understanding of the underlying process would greatly facilitate nanotechnological applications. In general, diatoms are classified into two major groups depending on the symmetry of their frustules [Van Den Hoek, 1997]. Centric diatoms are radially symmetrical, whereas pennate diatoms are elongated and bilaterally symmetrical.

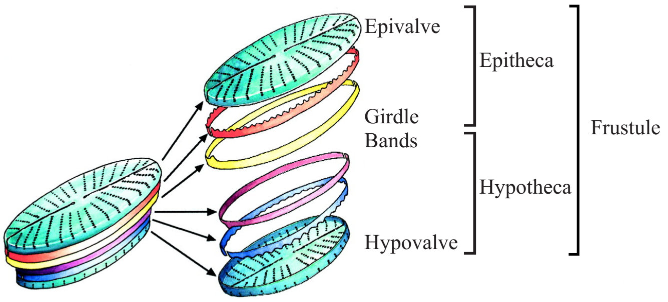

Figure 3-1
Schematic overview of the siliceous components of diatom cell walls. Adapted from [Zurzolo, 2001].

Diatom cells are diploid. The normal asexual method of reproduction is cell division into two daughter cells. Each valve of the parental cell thus becomes an epitheca of one daughter cell [Zurzolo, 2001] (see Figure 3-2). The process of frustule formation is only partially understood and is largely based on microscopic observations. Prior to cell division, the cell elongates, pushing the epitheca slightly away from the hypotheca, and the nucleus divides by mitosis. After the protoplast has divided by invagination of the plasma membrane, each daughter cell must generate a new hypotheca. The new valve which must cover one half of the cell, is commonly reproduced by the generation of a huge vesicle known as the silica deposition vesicle (SDV) [Drum, 1964]. Hypotheca biogenesis involves silica deposition inside the SDV followed by its coating with an organic matrix that prevents its dissolution. Once generated, the entire structure is then exocytosed, after which the two daughter cells separate. For the vast majority of diatom species, the Petri-dish nature of the frustule and its reproduction lead to a reduction in size during successive mitotic divisions in one of the daughter cells. Mitotically dividing diatom populations, therefore, decrease in size over time. Restoration of the original size occurs by sexual reproduction, followed by auxospore formation [Zurzolo, 2001].

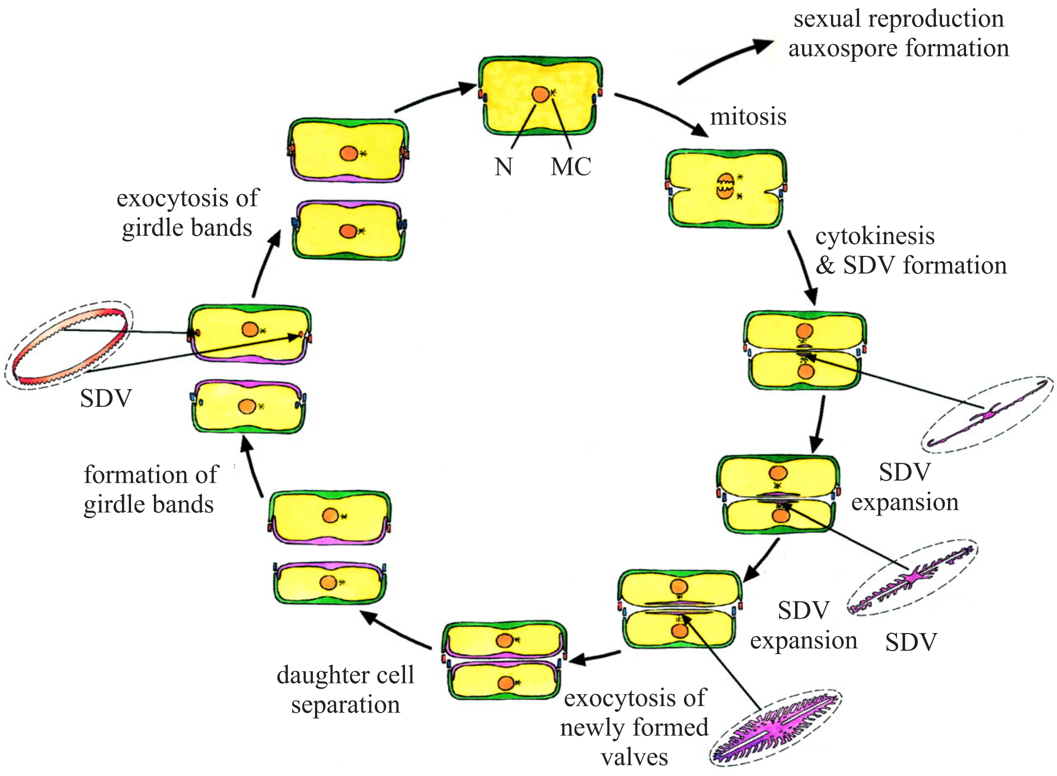

Figure 3-2 Schematic overview of mitotic cell division and hypovalve and girdle band formation. N: nucleus, MC: microtubule center, SDV: silica deposition vesicle. Adapted from [Zurzolo, 2001].

3.3 Experimental Methods

3.3.1 Diatom Cell Culture and ^{29}Si Isotope Labeling

The cells were grown in an artificial sea water medium at 20 °C with mechanical stirring and aeration at a *pH* between 8.2 and 8.8 applying a cycle of 14 h light/10 h darkness (5000-10000 Lux). The culture medium was prepared according to the recipe from the North East Pacific Culture Collection [Harrison, 1980] and was subsequently filtered aseptic. The culture containers were autoclaved before use. Three different isotope enriched silica types were used according to desired experimental conditions. Commercially available $Na_2SiO_3{\cdot}9H_2O$ (Merck) was used for experiments in natural abundance. For ^{28}Si or ^{29}Si enrichment, $Na_2{}^{28/29}SiO_3$ was produced by melting sodium carbonate (Na_2CO_3) and isotope enriched silicon (98.5% $^{28/29}SiO_2$, euriso-top) in a molar ratio of 1:1 at 1150 °C in a platinum crucible for 1 h [Brauer, 1975]. $Na_2{}^{28/29}SiO_3$ was dissolved in millipore water at 90 °C for 1 hour and added to the culture medium without further treatment.

3.3.2 Diatom Cell Synchronization

The process of mitosis in diatoms is coupled with the presence of silica required for the production of new cell walls. Therefore, several checkpoints for the availability of silica exist during the mitosis cycle. In the absence of a sufficient amount of silicon, cell division will not be induced and the cells are resting at certain stages in the cell cycle. [Brzezinski, 1990] [Martin-Jezequel, 2000]. Based on previous work concerning the synchronization of diatom cultures by silicon starvation on *Navicula pelliculosa* [Darley, 1971] and on *Thalassiosira pseudonana* [Frigeri, 2006], the following, slightly different method was applied: Cells were grown up in an artificial sea water medium (see above) until no silicic acid was detected in the medium anymore. The silicon level was monitored by a commercial photometric molybdate silicic acid test (Merck). The cell count was measured using a Neubauer counting chamber. After 24 - 48 hours, silicon starvation was terminated by the addition of fresh silicic acid. Afterwards, the development of new cell walls followed by cell separation were detected. Synchrony of the cell culture was verified by microscopy.

3.3.3 Cell Lysis and Cell Wall Purification

10 mL harvested cell samples were dissolved in a 200 mL solution containing 80 mM EDTA and 10 % SDS. The solution was boiled using a microwave. Afterwards, the sample was cooled, washed with millipore water, and centrifuged. Subsequently, the sample was resolubilized in the EDTA/SDS solution. This procedure was repeated until the cell solution remained colorless and only a white pellet of cell walls was visible after centrifugation.

3.3.4 Fluorescence Microscopy

Special fluorescent silica tracer dyes are taken up by diatoms. These dyes are accumulated inside the acidic environment of the SDV and inside the subsequently synthesized new cell walls [Li, 1989] [Shimizu, 2001] [Descles, 2008]. Fluorescence microscopy was applied in order to monitor the formation of freshly formed siliceous cell walls and to confirm the synchrony of the culture. After silicon starvation, fresh silicon and the fluorescence dye Lyso- Tracker Yellow HCK-123 (final concentration 1 μM, Invitrogen) [Descles, 2008] were added to the medium. A small aliquot of the culture was harvested in regular intervals. These samples were directly used without further treatment for fluorescence microscopic studies on a confocal laser scanning microscope (LSM 510 Meta, Zeiss). The wavelength of the argon laser for excitation was 488 nm. The ”green” fluorescence of HCK-123 was detected using an emission-filter 505-545 nm. A 660-800 nm emission-filter was used for the detection of the ”red” auto-fluorescence of the chloroplasts. Object lenses 100x (Plan Apochromat 100x/ 1,4oil DIC) and 40x (LD Achroplan 40x/ 0,6 corr Ph2) were used.

3.3.5 ^{29}Si Solid-State NMR Spectroscopy

Solid-state ^{29}Si NMR experiments were performed on a Bruker Avance 300 spectrometer operating at 59.6 MHz for ^{29}Si. A commercial double resonance 7 mm MAS NMR probe was used. The algal samples were centrifuged directly into home-made container insets exactly fitting into a 7 mm MAS NMR rotor (see Figure 3-3). Single-pulse excitation spectra (pulse length 6 μs) were recorded at 0 °C and a sample spinning rate of 4000 Hz. The spectra were referenced relative to liquid tetramethylsilane (δ = 0 ppm). For each spectrum, 4096 scans were accumulated with a delay of 42 s and spinal32 ^{1}H decoupling [Fung, 2000].

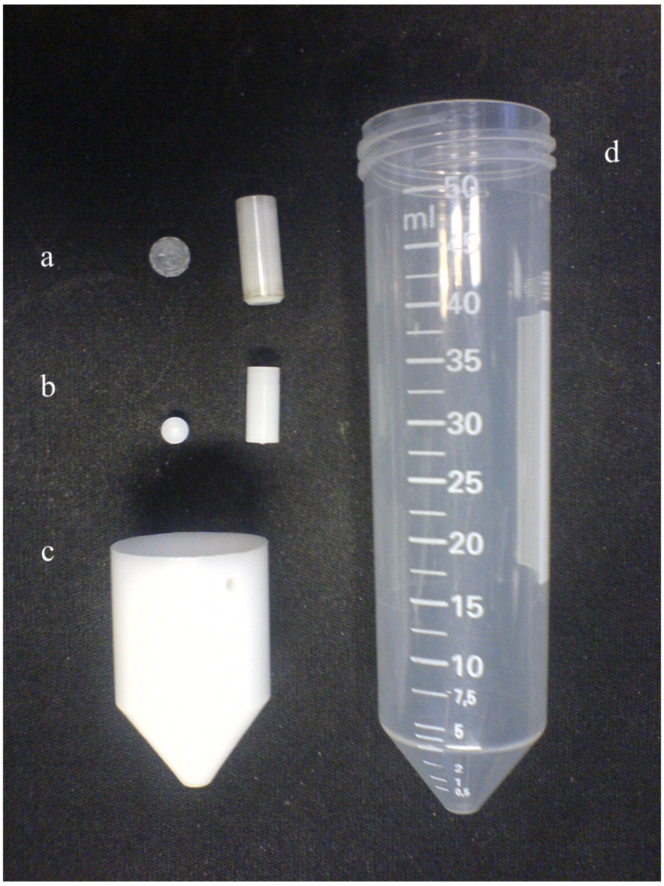

Figure 3-3
a) Standard 7 mm MAS rotor (Bruker) and rotor cap, b) home-made container inset and cap fitting exactly into a standard 7 mm MAS rotor, c) centrifugation inset fitting exactly into a standard 50 mL centrifugation tube (VWL), d) standard 50 mL centrifugation tube (VWL).

3.4 ^{29}Si NMR Spectroscopy

^{29}Si NMR spectroscopy is a versatile and non-destructive tool to detect ^{29}Si and to discriminate between the different silicon species. The chemical shift of ^{29}Si is very sensitive to changes in the chemical environment (see Figure 3-4) [Williams, 1979] [Marsman, 1981] [Gröger, 2008]. ^{29}Si NMR spectroscopy on biominerals greatly benefits from extended previous studies of silica-based inorganic materials such as zeolites and glasses [Engelhardt, 1987] [Eckert, 1992] [Engelhardt, 1996] [MacKenzie, 2002] [Eckert, 2004]. Nevertheless, ^{29}Si NMR spectroscopy of biominerals poses a number of problems and challenges. Since siliceous biominerals are usually amorphous, relatively broad solid-state ^{29}Si NMR signals result. The transverse relaxation times, T_2, observed in biominerals are relatively short which complicates the application of two-dimensional (2D) experiments based on the mixing or evolution of transverse magnetization. Moreover, relatively long relaxation delays between subsequent excitation steps have to be chosen due to the long T_1 times typically observed for ^{29}Si (up to several minutes). Doping of the biominerals with relaxation agents such as paramagnetic sites is in principle feasible but suffers from two major drawbacks: (i) It can not be excluded that this method unintentionally changes the structure of the material. (ii) Further line broadening may result. Long T_1-times in combination with the low natural abundance of only 4.7 % for ^{29}Si makes ^{29}Si NMR spectroscopy time-consuming. Therefore, ^{29}Si isotope labeling is necessarily required for NMR spectroscopy on biominerals, in particularly for 2D experiments.

The polymerization process of monosilicic acid has been studied extensively by ^{29}Si NMR spectroscopy. A variety of intermediate species such as polysilicic acid chains and rings have been identified [Harris, 1983] [Knight, 1986] [Engelhardt, 1987] [Knight, 1988] [Knight, 1989] [Kinrade, 1998a] [Kinrade, 1998b] [Brunet, 1991]. These species can easily be identified using liquid-state ^{29}Si NMR spectroscopy by means of their characteristic chemical shifts [Marsman, 1981]. Figure 3-5 shows two spectra of a freshly prepared silicic acid solution (top) and of the same sample after 24 h (bottom). The different silica species are assigned to their Q-groups due to their well known chemical shifts. Figure 3-4 shows a summary of ^{29}Si chemical shifts measured for various silicon species including organo-silicon complexes [Engelhardt, 1987] [Engelhardt, 1996] [Marsman, 1981] [Williams, 1982] [Wasylishen, 1982] [Williams, 1989] [Maciel, 1996] [Marsmann, 1996] [Kinrade, 1999] [Tacke, 1999] [Lewis, 2001] [Kinrade, 2001a] [Kinrade, 2001b] [Kinrade, 2004] [Mabboux, 2005] [Bruker, 2005] [Gröger, 2008] as well as data resulting from quantum chemical calculations [Sahai, 2001] [Sahai, 2002] [Kubicki, 2003] [Sahai, 2004] [Casserly, 2005]. Since the chemical shift ranges observed for the various species overlap each other, it is sometimes impossible to unambiguously confirm the existence of certain silicon species solely by means of the chemical shifts taken from one-dimensional (1D)

^{29}Si NMR spectra. Therefore, 2D NMR techniques have to be applied in many cases.

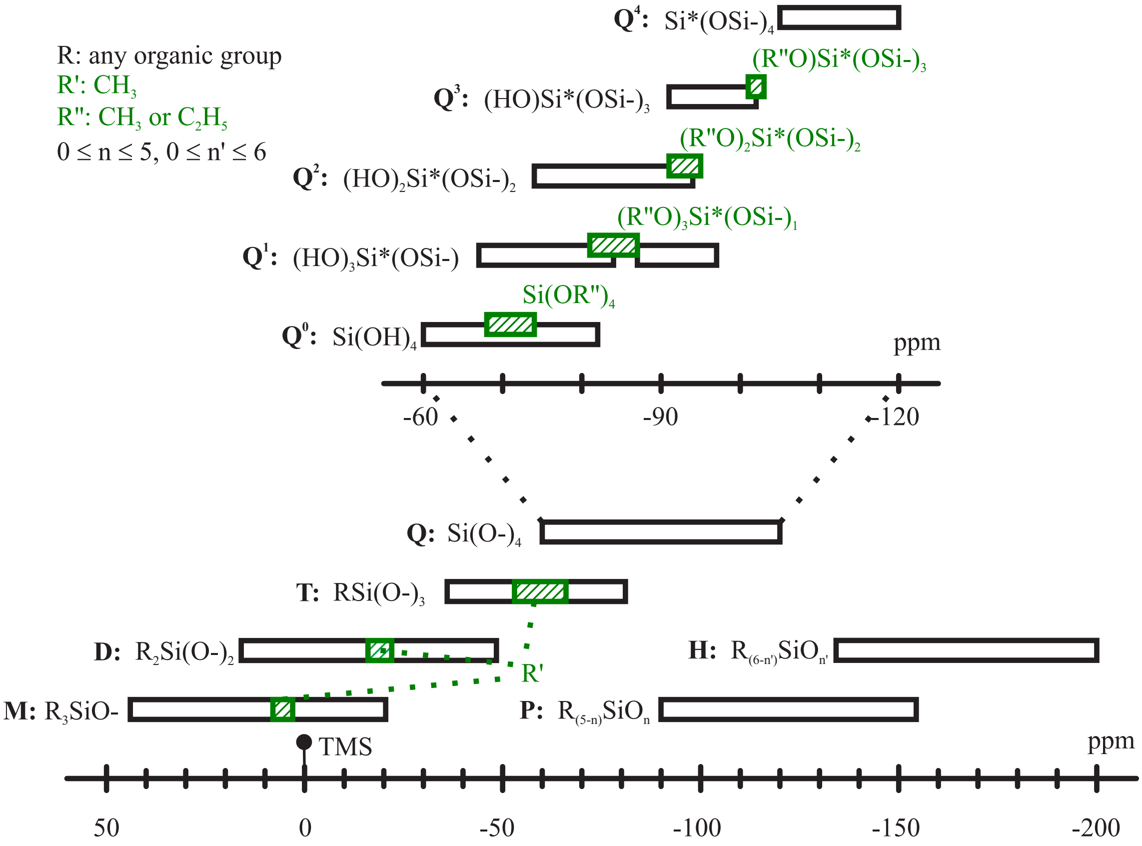

Figure 3-4 ^{29}Si NMR chemical shifts of various silicon species. It should be noted that different notations are found in the literature for some of the listed silicon species. Here, the Q-group notation is used [Engelhardt, 1987]. All four-coordinated silicon species surrounded by four oxygen atoms are denoted as Q-groups.

The linewidth of a ^{29}Si NMR signal in a solution is correlated with the overall rotational correlation time τ_c of the corresponding silica species [Cavanagh, 1996]. τ_c is given by the following equation:

$$\tau_c = \frac{4\pi\eta_w r_H^3}{3k_B T} \tag{3.1}$$

η_w denotes the viscosity of the solvent, r_H is the hydrodynamic radius of the particle which may differ from the radius of the particle measured, e.g., by dynamic light scattering. k_B denotes the Boltzmann constant and T is the temperature. Note that polymerized silica particles, exceeding a certain size, are not necessarily visible in liquid-state ^{29}Si NMR experiments due to the large rotational correlation time of such particles and the correspondingly low signal to noise ratio of the signal (see Figure 3-5).

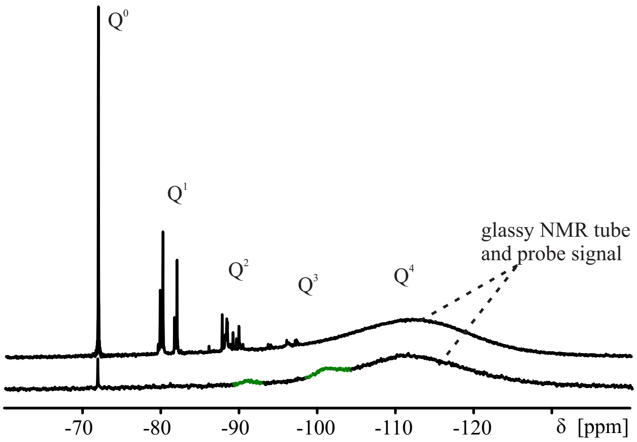

Figure 3-5
^{29}Si liquid-state NMR spectra of a silicic acid solution prepared from ^{29}Si isotope labeled Na_2SiO_3 (0.5 M). Top: after 10 min. Bottom: after 24 h. The broad background signal centered around -112 ppm originates from the glassy NMR tube and the probe. The green marked signals in the lower spectrum are due to polymerized and immobile silica species.

3.5 ^{29}Si NMR Spectroscopic Studies on Silica Deposits in Plants: An Overview

The deposits of amorphous silica, found in several plants, are important for growth, mineral nutrition, mechanical strength, and resistance against stress and diseases [Epstein, 1994] [Ma, 2006]. Monosilicic acid is taken up from the soil by the roots and transported through the xylem. Subsequently, it is accumulated and deposited as polymerized silica. A gene controlling the silica uptake in rice could be identified meanwhile [Ma, 2002]. Nevertheless, many steps of the silicon metabolism and biomineralization process remain enigmatic. This is particularly true for the mechanism underlying the maintenance of a supersaturated silicic acid concentration during the transport of silicic acid and the selective polymerization at special places. As already mentioned, ^{29}Si NMR spectroscopy is well-suited to identify different silicon species by chemical shift analysis. Therefore, a number of liquid-state (see Table 3-2) as well as solid-state (see Table 3-3) ^{29}Si NMR spectroscopic studies have been performed in order to determine the form and composition of silicon species in plants [Bertermann, 2000] [Mann, 1983] [Casey, 2004] [Freitas, 2000] [Mitani, 2005] [Park, 2006].

Species	Q^0	Q^1
Tricitum aestivum, xylem sap	-71	-80
Oryza sativa, xylem sap	-72.6	

Table 3-2
Isotropic ^{29}Si NMR chemical shift values for plants taken from liquid-state NMR studies.

Species	Q^2	Q^3	Q^4
Equisetum arvense stems and blossoms, freeze-dried	-92	-101	-111
Equisetum giganteum leaves, freeze-dried	-92	-101	-111
Equisetum giganteum stems, freeze-dried	-92	-101	-111
Equisetum hyemale blossoms, freeze-dried	-91	-101	-111
Equisetum hyemale stems, freeze-dried	-91	-101	-111
Equisetum palustre stems and leaves, freeze-dried	-92	-101	-110
Equisetum telmateia stems and blossoms, freeze-dried	-92	-101	-111
Echium vulgare stem leaves, freeze-dried	-92	-101	-110
Symphytum officiale stem leaves, freeze-dried	-92	-101	-110
Phalaris canariensis hairs, untreated and acid treated, after syliation new signal at 13.5 ppm	-92	-102	-111
Rice hulls cut and oven dried at 105 °C, signal at -26 ppm	-90	-100	-112
Rice leaves	-92	-101	-111

Table 3-3
Isotropic ^{29}Si NMR chemical shift values for various plants taken from solid-state NMR studies.

In general, the signal patterns are very similar to those typically observed for synthetic silica gels [Maciel, 1980] [Maciel, 1996]. ^{29}Si MAS NMR studies were performed on hairs of the grass *Phalaris canariensis* [Mann, 1983] [Perry, 1989a] [Perry, 1989b] [Perry, 2003]. The spectra exhibit the characteristic signals of the Q_4, Q_3, and Q_2 groups. Relatively broad lines indicate the amorphous state of the silica. The presence and location of surface hydroxyl groups was tested by silylation: The samples were exposed to Me_3SiCl which reacts with Si-OH groups forming Me_3Si-O-Si moieties. The result of this reaction could be quantified by solid-state ^{29}Si NMR spectroscopy. In particular, a decrease of the Q_3 and Q_2 group signals could be observed which is accompanied by the appearance of a new signal at +13.5 ppm indicating the formation of Me_3Si-O-Si moieties (see Figure 3-6). Interestingly, only 24 % of the hydroxyl groups are capable of reacting with Me_3SiCl. This observation shows that only about 1/4 of the hydroxyl groups is located at Me_3SiCl-accessible surface sites.

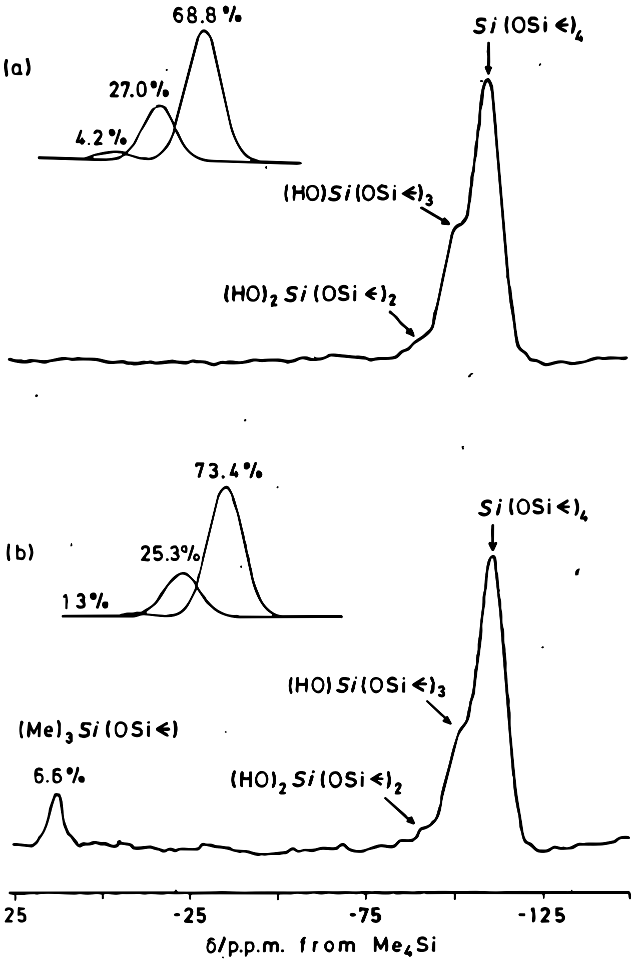

Figure 3-6
^{29}Si MAS NMR spectra of fibres from *Phalaris canariensis* before (a) and after (b) silylation. Taken from [Mann, 1983].

Bertermann and Tacke [2000] have also studied various plant species by solid-state ^{29}Si NMR spectroscopy. The 1D ^{29}Si CP MAS NMR spectra of freeze-dried plant samples exhibit the characteristic Q-group signals of amorphous silica. None of the signals, typical for organosilicon complexes, could be observed. Furthermore, several solid-state ^{29}Si NMR studies were performed on rice, a plant which is well-known to accumulate high amounts of silica in its hulls [Hamdan, 1997] [Freitas, 2000] [Park, 2006]. Apart from the aforementioned ordinary signals of the Q-groups, only one paper reports the existence of a signal due to organo-silicon species [Freitas, 2000]: Rice hulls and the endocarp from babassu coconuts were examined in this work. A sharp signal at -26 ppm could be identified in the directly excited ^{29}Si MAS NMR spectra of both samples apart from a very broad signal centered around -112 ppm. These experiments were performed with a short relaxation delay (2 s for the rice hulls, 10 s for the coconut endocarp). Short relaxation delays favor the accumulation of signals arising from organo-silicon species by partially suppressing the signals due to the Q-groups which typically possess relatively long T_1 times in the solid-state. However, the signal located at -26 ppm could not be detected in ^{29}Si{^{1}H} CP MAS NMR experiments, although the presence of neighboring ^{1}H-nuclei are expected for organo-silicon species. One reason for this observation might be the high mobility of the organo-silicon species which would result in a decreased CP efficiency. Furthermore, liquid-state ^{29}Si NMR experiments were carried out on the xylem sap of wheat [Casey, 2004] and rice [Mitani, 2005]. In both studies, the plants were allowed to soak up a ^{29}Si-enriched nutrient solution prior to the sample extraction. The ^{29}Si NMR spectra of both samples exhibit a signal at -72 ppm that is characteristic for monosilicic acid. In addition, a minor peak at -80 ppm is observed for wheat which corresponds to disilicic acid. Interestingly, the silicic acid rapidly autopolymerizes after the collection of the xylem sap indicating the absence of any additional silicic acid stabilizing factors in the xylem sap of wheat and rice.

3.6 ^{29}Si NMR Spectroscopic Studies on Silica Deposits in Diatoms and Sponges

A first insight into the short range structure and the composition of the inorganic bulk silica is delivered by 1D ^{29}Si MAS NMR experiments. Numerous ^{29}Si MAS NMR spectroscopic studies of diatoms, sponges and snails have meanwhile been published (see Tables 3-4 and 3-5) [Perry, 1989b] [Bertermann, 2003] [Christiansen, 2006] [Lutz, 2005] [Vrieling, 2003] [Weaver, 2003] [Gendron-Badou, 2003] [Sumper, 2006b] [Brunner, 2007]. Typical one-dimensional ^{29}Si MAS NMR spectra of the diatom cell walls from *Thalassiosira pseudonana*, *Ditylum brightwellii* and *Stephanopyxis turris* are shown in Figure 3-7. The siliceous cell walls were isolated according to the procedure given by Kröger *et al.* [1999]. All spectra exhibit the well-known signals due to four-coordinated silicon at δ = -92 ppm (Q^2 groups), δ = -102 ppm (Q^3 groups) and δ = -111 ppm (Q^4 groups). They are very similar to the spectra observed for amorphous silica found in siliceous plant deposits (see Table 3-3) and in other diatom species (see Table 3-4 and 3-5).

Species	Q^2	Q^3	Q^4
Halichondria panecea (sponge)	-93	-102	-112
Navicula pelliculosa (diatom) cell walls untreated and acid treated	-93	-102	-114
Patella vulgate (snail) limpet teeth	-	-102	-114
Chaetoceros debiles (diatom)			
complete cells, freeze-dried	-92	-102	-111
isolated cell walls, freeze-dried	-92	-101	-111
Chaetoceros didymum (diatom)			
complete cells, freeze-dried	-92	-102	-111
isolated cell walls, freeze-dried	-92	-101	-111
Cylindrotheca fusiformis (diatom)			
complete cells, freeze-dried	-92	-102	-111
isolated cell walls, freeze-dried	-92	-102	-111
Nitzschia angularis (diatom)			
complete cells, freeze-dried	-92	-101	-110
isolated cell walls, freeze-dried	-92	-101	-110
Thalassiosira pseudonana (diatom) sonicated, freeze-dried	-94	-102	-112

Table 3-4
Isotropic ^{29}Si NMR chemical shift values for various diatoms, sponges, and snail teeth, continued in Table 3-5.

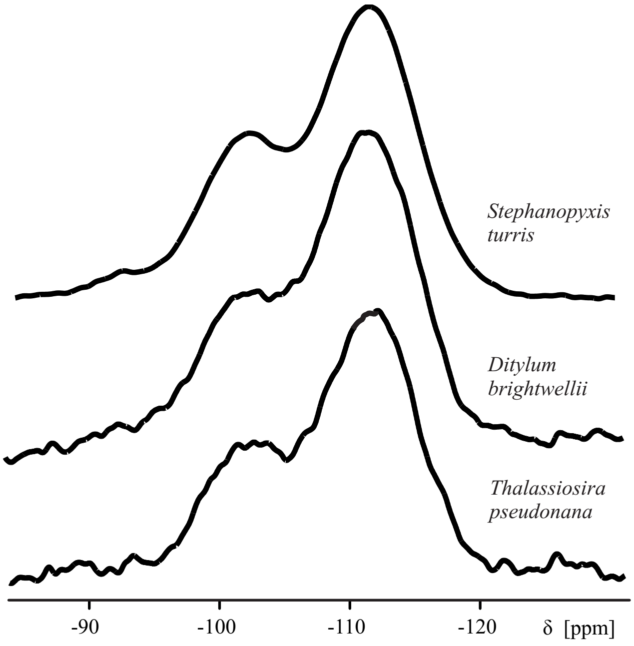

Figure 3-7
^{29}Si MAS NMR spectrum of ^{29}Si isotope labeled cell walls isolated from *Stephanopyxis turris* and cell walls with natural abundance of ^{29}Si isolated from *Ditylum brightwellii* and *Thalassiosira pseudonana*.

The differences of the ^{29}Si chemical shift and of the intensity ratio of the Q-groups found for the various species and samples in Tables 3-4, 3-5 and in the presented spectra above are well within the experimental error, i.e., no significant differences are detected.

Species	Q^2	Q^3	Q^4
Navicula pelliculosa (diatom) complete cells, ^{29}Si pulse labeld liquid-state NMR -71 ppm (Q^0), -131.5 ppm	-	-	-
Coscinodiscus granii (diatom) isolated cell walls, freeze-dried	-93	-102	-111
Ditylum brightwellii (diatom)			
untreated	-92	-102	-111
acid cleaned	-92	-102	-111
Thyla aurantia (sponge) acid treated	-	-101	-112
sponge	-92	-102	-111
Chatoceros (diatom) freeze-dried, -84 ppm (Q^1)	-92	-102	-111
fossil diatoms	-91	-101	-112
Stephanopyxis turris (diatom) isolated cell walls, freeze-dried	-93	-102	-112
Thalassiosira pseudonana (diatom) isolated cell walls, freeze-dried	-92	-102	-111

Table 3-5
Isotropic ^{29}Si NMR chemical shift values for various diatoms, sponges, and snail teeth. Continuation of Table 3-4.

A series of ^{29}Si{^{1}H} CP MAS NMR spectra of commercially available ^{29}Si isotope enriched SiO_2 (euriso-top) and ^{29}Si isotope labeled isolated cell walls of *Thalassiosira pseudonana* were measured with different cross polarization times τ ranging from 0.5 ms to 50 ms. The spectra series are depicted in Figure 3-8 (SiO_2) and in Figure 3-9 (*Thalassiosira pseudonana*). Comparing the synthetic $^{29}SiO_2$ sample and the natural biomineral, the pronounced differences are clearly seen. Note that the absolute intensities of the spectra are normalized differently. The relative intensities of the different resonances in the ^{29}Si{^{1}H} CP MAS NMR spectra strongly depend on the number and distances of the neighboring ^{1}H nuclei and the contact time used in the pulse program. The signal-area of the different resonances does, therefore, not reflect the real molar ratio of the different Q^n groups present in the samples but indicates the presence of neighboring ^{1}H nuclei.

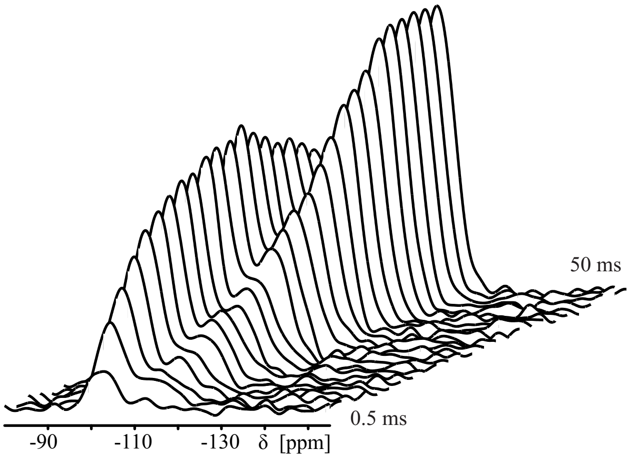

Figure 3-8
^{29}Si{^{1}H} CP spectra series of commercially available $^{29}SiO_2$ for CP times between 0.5 ms and 50 ms.

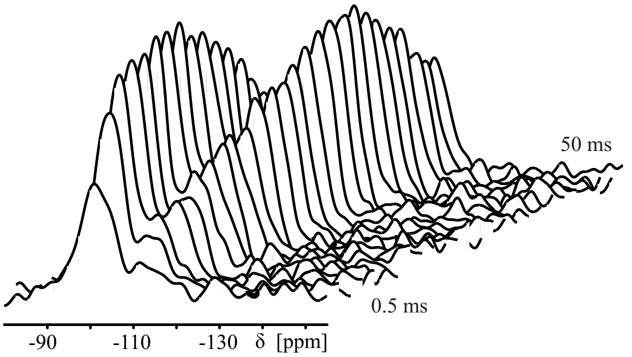

Figure 3-9
^{29}Si{^{1}H} CP spectra series of ^{29}Si isotop labeled and insolated cell walls of *Thalassiosira pseudonana* for CP times between 0.5 ms and 50 ms.

The signal intensity, I_{CP}, observed in the $^{29}\mathrm{Si}\{^1\mathrm{H}\}$ CP experiment depends on the CP contact time, τ, as follows [Mehring, 1983]:

$$I_{\mathrm{CP}}(\tau) \propto \left(1 - \frac{T_{\mathrm{CP}}}{T_{1\rho}^{H}}\right)^{-1} \left(\exp\left\{-\frac{\tau}{T_{1\rho}^{\mathrm{H}}}\right\} - \exp\left\{-\frac{\tau}{T_{\mathrm{CP}}}\right\}\right) \tag{3.2}$$

T_{CP} is the so-called CP buildup time constant. $T_{1\rho}^{\mathrm{H}}$ is the longitudinal relaxation time of the ^{1}H-nuclei under spin-locking conditions. Note that equation 3.2 only holds if $T_{1\rho}^{\mathrm{H}}$ is short compared to $T_{1\rho}^{\mathrm{Si}}$; a condition which is usually fulfilled. The initial buildup of the intensity is, therefore, due to the increase of ^{29}Si magnetization owing to cross polarization from protons with a characteristic time constant T_{CP}. The subsequent decay of the signal intensity is a manifestation of the relaxation of the spin-locked ^{1}H magnetization characterized by the longitudinal $T_{1\rho}^{\mathrm{H}}$ spin lattice relaxation time in the rotating frame. The longitudinal relaxation time $T_{1\rho}^{\mathrm{Si}}$ is two orders of magnitude higher than that for protons. Plots of the signal intensities I_{CP} as a function of the CP time τ for the two measurement ^{29}Si{^{1}H} CP NMR series, depicted in Figure 3-8 (^{29}Si isotope labeled SiO$_2$) and Figure 3-9 (cell walls from *Thalassiosira pseudonana*) as well as for a sample of isolated cell walls of *Chaetoceros didymum*, are given below. The intensities I_{CP} are given in arbitrary units.

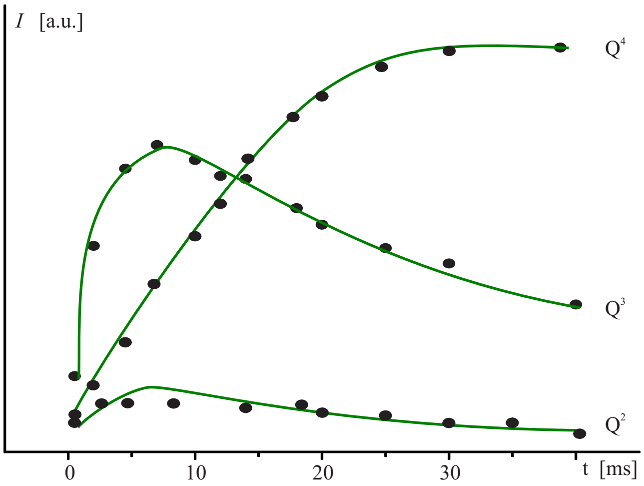

Figure 3-10
Signal intensity I_{CP} as a function of the CP time τ for commercially available ^{29}SiO$_2$ depicted in Figure 3-8.

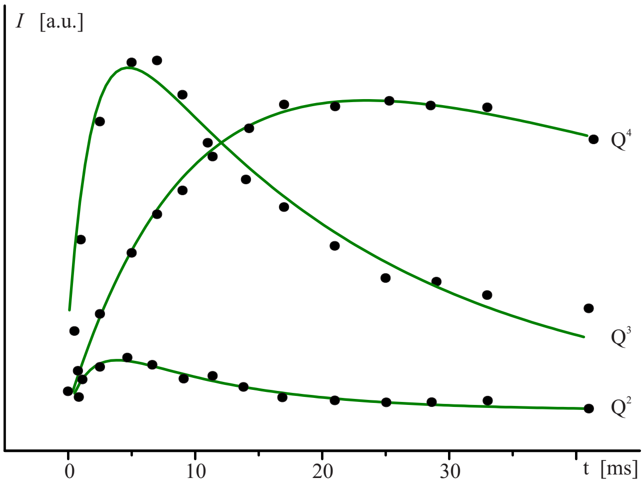

Figure 3-11
Signal intensity I_{CP} as a function of the CP time τ for ^{29}Si isotope labeled, isolated cell walls of *Thalassiosira pseudonana* depicted in Figure 3-9.

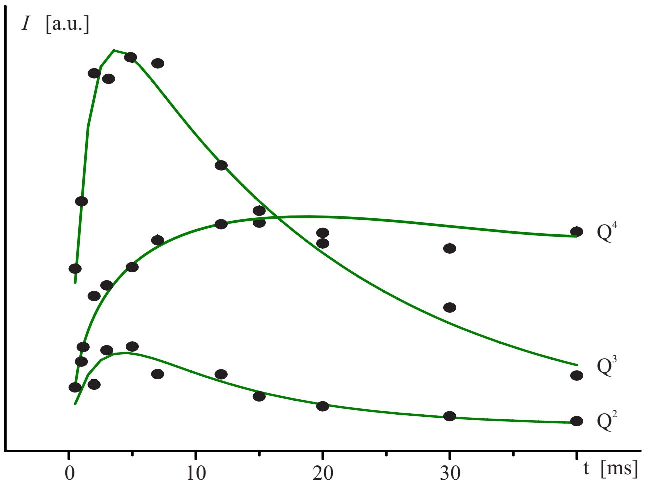

Figure 3-12
Signal intensity I_{CP} as a function of the CP time τ for ^{29}Si isotope labeled, isolated cell walls of *Chaetoceros didymum*.

In order to extract the relevant time constants $T_{1\rho}^{\mathrm{H}}$ and T_{CP}, the data points were fitted using equation 3.2. Table 3-6 gives a list of the time constants $T_{1\rho}^{\mathrm{H}}$ and T_{CP} obtained from Figures 3-10–3-12. The Table also includes the values for a silica gel (natural abundance of ^{29}Si) taken from the literature [Maciel, 1980]. The values of the Q^2 could not be reliably determined due to the low signal-to-noise ratio of the Q^2 group signal in the corresponding spectra. For all samples, the cross polarization buildup time T_{CP} of the Q^3 groups is shorter than for the Q^4 groups. This is consistent with the environment of the Q^n groups: for Q^3 groups one silanol group is bound to the center Si atom and a direct polarization transfer takes place from the proton. The silicon atom in a Q^4 group is connected to four O-Si groups and the nearest hydroxyl group is at least four bonds away. Therefore, a polarization transfer is only possible for long CP times or due to homonuclear spin diffusion processes between ^{29}Si atoms, particularly in case of the ^{29}Si isotope labeled samples. However, there is a difference in T_{CP} between the synthetic samples and the extracted cell walls. The cell walls exhibit shorter T_{CP} times than the silica gel or $^{29}SiO_2$. There is no difference in the 1D $\pi/2$-pulse spectra of these samples (all spectra exhibit the same Q-group ratio) which indicates that the silica composition is the same in all four compounds. Especially, the polarization transfer to the Q^4 groups is much faster for the cell wall samples suggesting the presence of other ^{1}H close to the Q^4 groups. An explanation for this cross polarization behavior could be the intercalation of organic material (e.g. silaffines, polyamines) in the bulk silica of the cell walls during cell wall biogenesis. This is consistent with the so-called phase separation model which describes a possible mechanism for cell wall growth templated by organic molecules [Sumper, 2002]. The observed difference between the spin-lattice relaxation time $T_{1\rho}^{\mathrm{H}}$ of the biological samples and the synthetic samples can also be ascribed to the presence of organic molecules in the former material.

	T_{CP} [ms]			$T_{1\rho}^{\mathrm{H}}$ [ms]		
	Q^2	Q^3	Q^4	Q^2	Q^3	Q^4
C. didymum	(2.1)	1.7	6.1	10.9	19.2	-
T. pseudonana	(1.8)	1.9	8.9	10.4	21.4	71.6
silica gel	2.3	2.9	12.7	20.3	22.1	21
SiO_2	2.4	2.4	17.1	18.7	27.3	-

Table 3-6
$T_{1\rho}^{\mathrm{H}}$ and T_{CP}.

^{29}Si isotope labeling allowed the recording of 2D HETCOR spectra [Christiansen, 2006] [Brunner, 2007]. This experiment allows the measurement of the chemical shift of both the ^{1}H species and the ^{29}Si species involved in the polarization transfer. This experiment was performed on two samples of ^{29}Si isotope labeled cell walls of *Thalassiosira pseudonana*. The cell walls were isolated using the method described by Kröger *et al.* [1999] (see Chapter 3.3.3) but were not freeze-dried. After isolation of the cell walls, an aliquot of the samples was dried for 40 hours at 200 °C under vacuum (dried sample). Another aliquot was measured without further treatment (not dried sample). The 2D ^{29}Si{^{1}H} HETCOR spectra are depicted in Figure 3-13 (not dried sample) and Figure 3-14 (dried sample).

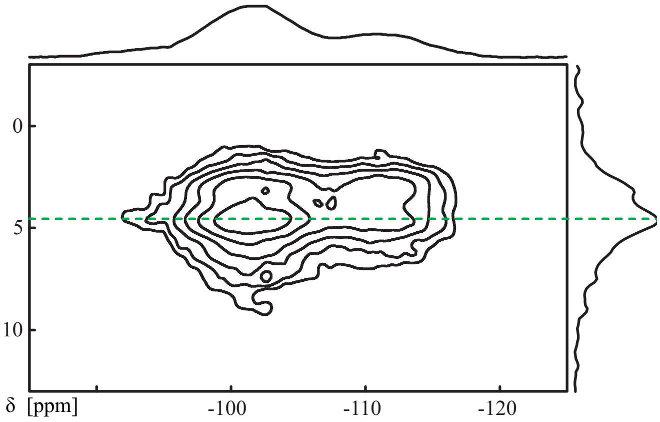

Figure 3-13
^{29}Si{^{1}H} HETCOR spectrum of not dried isolated cell walls of *Thalassiosira pseudonana*. The F_2 and F_1 projections are shown at the top and the right side of the 2D spectrum, respectively. The green line indicates the chemical shift of adsorbed water at ca. 4.8 ppm.

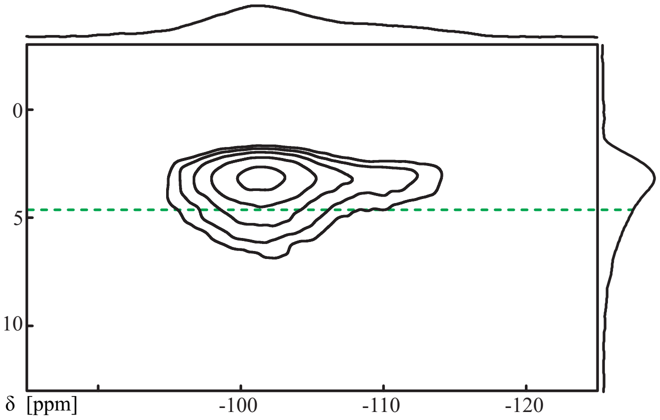

Figure 3-14
^{29}Si{^{1}H} HETCOR spectrum of dried isolated cell walls of *Thalassiosira pseudonana*. The F_2 and F_1 projections are shown at the top and the right side of the 2D spectrum, respectively. The green line indicates the chemical shift of adsorbed water at ca. 4.8 ppm.

The spectra were found to be strongly dependent on the sample hydration state: In dried samples, polarization transfer takes place from ^{1}H-nuclei of the silanol groups $\delta = 3-4$ ppm [Maciel, 1996] to neighboring ^{29}Si-nuclei. Therefore, Q^3 and Q^2 groups with their closely attached hydroxyl groups are mainly detected in the ^{1}H-^{29}Si HETCOR spectrum of the dried sample whereas the Q^4 group signal is strongly suppressed. In not dried samples, the adsorbed water molecules significantly contribute to the ^{29}Si{^{1}H} cross polarization. It is, however, surprising that a significant ^{29}Si{^{1}H} cross polarization transfer from the adsorbed water to Q^4 groups is also observed (indicated by the green line in the spectra). These units are expected to be located in the bulk SiO_2 which should be inaccessible for water. This observation can be explained by two possible assumptions: (i) Water penetrates into the bulk SiO_2 of diatom cell walls or (ii) ^{29}Si-^{29}Si spin diffusion takes place from the Q^2 and Q^3 groups located at the outer surface to the Q^4 groups in the bulk during the CP time since the samples are ^{29}Si isotope labeled. In any case, a pronounced influence of sample hydration upon the ^{29}Si{^{1}H} CP MAS NMR spectra must be stated.

Most of the solid-state NMR studies on diatoms described in the literature were performed on freeze-dried samples (see Table 3-4 and 3-5). However, test experiments on a silicic acid - protein solution revealed that the polymerization state of the silica is changed by the freeze-drying procedure. Bovine albumin (0.0005 M) which is known to be highly soluble was solubilized in a silicic acid solution (0.05 M) prepared using TMOS as silica source [Iler, 1979]. Figure 3-15 shows the resulting spectra of this experiment. The top spectrum was measured on a freshly prepared silicic acid - protein solution. Apart from the background signal of the glass NMR tube, only narrow Q-group signals due to lowly polymerized silica species are visible in the spectrum. The bottom spectrum was recorded after freeze-drying the sample. The spectrum reveals only signals due to highly polymerized silica species (Q^3 and Q^4). This experiment shows that lowly condensed silicon species are transformed into species of a higher condensation state after freeze-drying the sample. That means, the ^{29}Si MAS NMR signals of freeze-dried cells are not necessarily representative for the biologically relevant state of the silicon species.

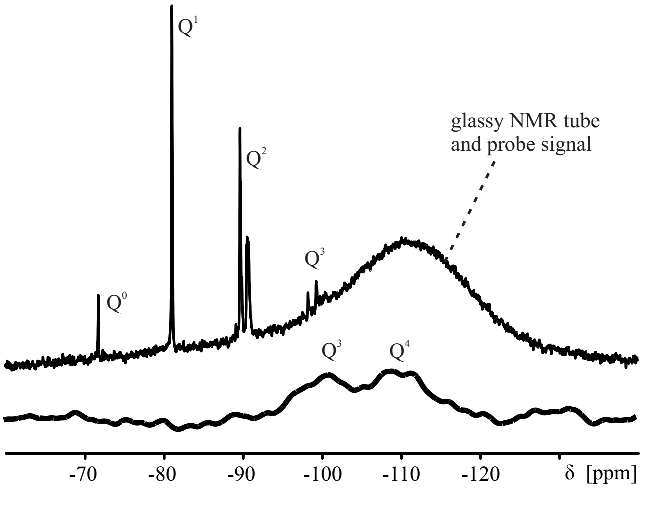

Figure 3-15
^{29}Si liquid-state NMR spectrum of a freshly prepared silicic acid - protein sample (top) and ^{29}Si solid-state MAS spectrum of the same sample after freeze-drying (bottom).

The relative intensities of the different Q-group signals, especially the so-called Q_4/Q_3 ratio, were found to depend on the samples and their pretreatment, also in directly excited spectra. Freeze-dried, complete diatom cells usually exhibit a lower Q_4/Q_3 ratio than extracted, cleaned cell walls [Bertermann, 2003]. This observation can be interpreted as a spectroscopic hint for the presence of silicon species in a lower condensation state within the cells rather than in the bulk cell wall material and poses the question of the silicon metabolism of diatom cells.

Organo-silicon complexes, which are assumed to be formed in siliceous biominerals, are of special interest. This interest is based on the fact that various organic components were found in close contact with the inorganic phase of silica biomaterials. Organic-silicon compounds placed inside the bulk silica of biominerals can only be identified in a 1D solid-state ^{29}Si NMR experiment if the chemical shift is outside the chemical shift area of the Q^2, Q^3, and Q^4 groups. Otherwise, the relevant signals are generally covered by the signals of the abundant inorganic bulk silica. A rather uncommon signal at -65 ppm was detected in the ^{29}Si{^{1}H} CP MAS NMR spectra of freeze-dried diatom samples [Gendron-Badou, 2003]. An assignment to Q^0 species can be ruled out since the samples are freeze-dried. Furthermore, the signal is very broad and an unequivocal assignment is prevented by the low signal to noise ratio. This signal and the above mentioned transient signal ($\delta = -131$ ppm) detected by Kinrade *et al.* [2002] are the only examples of such organo-silicon compounds verified by ^{29}Si NMR on diatoms.

As already mentioned above, diatom cell walls contain various organic molecules. Part of them, in particular, the coat proteins are removed by treatment with EDTA and SDS [Kröger, 1996]. Other biomolecules are tightly bound to the silica framework and resist the EDTA/SDS treatment. Two types of molecule were identified in the non-EDTA/SDS extractable organic material which are capable of initiating and accelerating silica precipitation from silicic acid solutions *in vitro*; namely silaffins and long-chain polyamines. Solid-state NMR spectroscopy allows one to study these various biomolecules embedded into their natural siliceous environment. Extracted cell wall material from several diatom species were investigated by solid-state ^{13}C NMR spectroscopy [Christiansen, 2006] [Brunner, 2007] [Vrieling, 2003]. A ^{13}C MAS NMR spectrum of ^{13}C isotope labeled cell walls extracted from *Thalassiosira pseudonana* is shown in Figure 3-16. A variety of signals is observed since the organic material in the cell walls consists of a variety of different macromolecules such as silaffins, polyamines, and sugar moieties: The intense signal at 160-190 ppm is due to the carbonyl groups of the amino acid residues. The alkyl carbon signals are found between 10-60 ppm, N- and O- alkyl signals occur at 40-90 ppm. Among others, the C-N signals of the polyamines are also observed in this region. The major portion of the C-O signals are ascribed to sugars. Finally, the signals of lower intensity can be assigned to acetal groups originating from polysaccharides (95-110 ppm) and aromatic carbon atoms (120-140 ppm). Qualitatively, the ^{13}C MAS NMR spectrum of *Thalassiosira pseudonana* is similar to the one recorded by Christiansen *et al.* [2006]. The given assignment is further corroborated by ^{13}C{^{1}H} CP (Figure 3-17) and ^{13}C{^{1}H} HETCOR (Figure 3-18) experiments. Note, that the HETCOR experiment was performed under phase-modulated Lee-Goldburg [Vinogradov, 1999] proton decoupling.

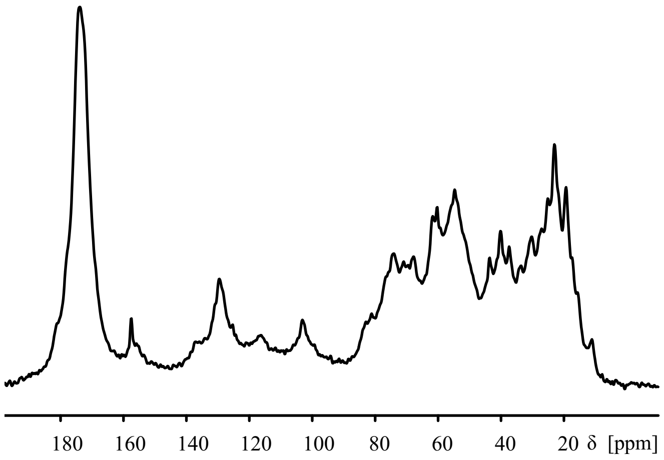

Figure 3-16
^{13}C solid-state NMR spectrum of cell walls of *Thalassiosira pseudonana*. The spectrum was recorded by Katharina Lutz.

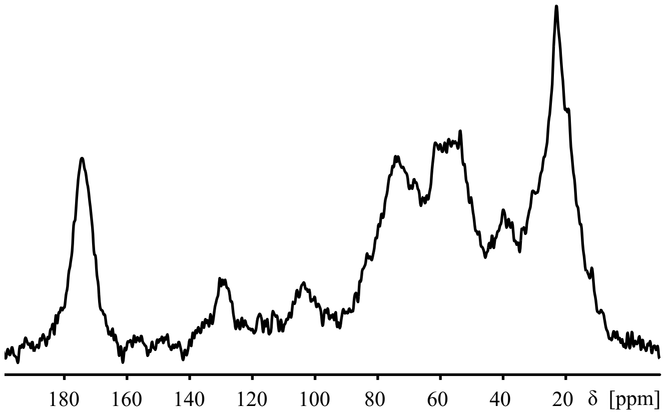

Figure 3-17
$^{13}C\{^1H\}$ solid-state CP NMR spectrum of cell walls of *Thalassiosira pseudonana*. The spectrum was recorded by Katharina Lutz.

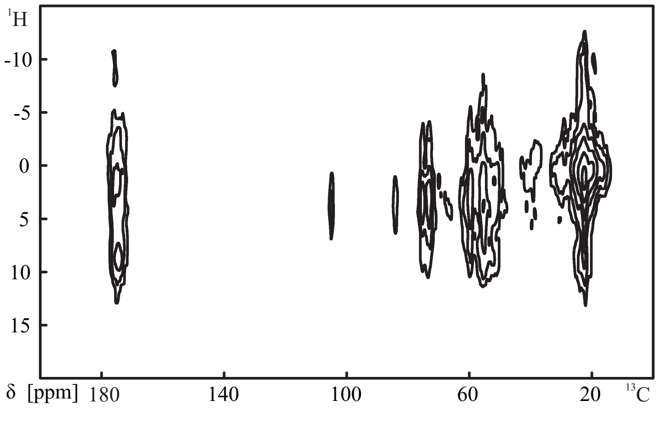

Figure 3-18
2D $^{13}C\{^1H\}$ HETCOR NMR spectrum of cell walls of *Thalassiosira pseudonana* with Lee-Goldburg decoupling during the ^1H evolution time. The spectrum was recorded by Katharina Lutz.

3.7 ^{29}Si NMR Studies Concerning the Silicon Metabolism of Diatoms

Cell division and cell cycle of diatoms are tightly associated with the cellular silicon metabolism. The presence of silicon is one major limiting factor for the reproduction rate of diatoms [Martin-Jezequel, 2000]. Diatom growth is the main reason for the low abundance of silicon in seawater which exhibits an average concentration of ca. 70 μM [Hildebrand, 2000]. In surface waters, where diatoms often occur, silicon levels can be lower than 10 μM [Thamatrakoln, 2007]. In contrast, intracellular concentrations of silicic acid can be several hundred mM depending on the species [Martin-Jezequel, 2000] [Martin-Jezequel, 2003]. Therefore, diatoms must possess a very efficient uptake and storage system which can accumulate and maintain such a high intracellular silicon concentration. Diatoms take up silicon predominantly in the form of monosilicic acid. Specific silicic acid-binding proteins located at the cell wall of diatoms were discovered which are capable of transporting silica into the cells [Hildebrand, 1997]. The activity of these silicon transporter proteins (SITs) is largely controlled by intracellular processes and not by protein levels [Thamatrakoln, 2007]. On the other hand, intracellular silicon transport is rather poorly understood. The synthesis of new valves takes place in a highly specialized intracellular vesicle, the silica deposition vesicle (SDV) [Drum, 1964]. Tightly bound to the inorganic silica framework of the valves, specific biomolecules were extracted and identified from different diatoms species (silaffins, polyamines) [Kröger, 1999] [Kröger, 2000] [Kröger, 2001] [Sumper, 2005]. Interestingly, the composition of these organic components is different for different diatom species [Sumper, 2006a]. It was also shown that these molecules are capable of inducing and accelerating silica precipitation *in vitro* [Kröger, 2002] [Lutz, 2005] [Sumper, 2006a]. These molecules are, therefore, assumed to play a crucial role in the silica biogenesis and to be responsible for the design of the cell walls [Perry, 2000] [Patwardhan, 2005]. However, little is known about the storage mechanism of silicon after uptake from the environment and before deposition inside the SDV. Intracellular pools of soluble silicon were first identified by Werner [1966]. These pools account for a sizable fraction of up to 50 % of the total silicon content of the cells corresponding to a silicon concentration between 19 and 680 mM. [Martin-Jezequel, 2000] [Martin-Jezequel, 2003] [Hildebrand, 2000]. The pool sizes differ between the different diatom species as well as during the cell cycle. The pool size is also correlated with the time lag between silicon uptake from the seawater and deposition in the cell walls: Diatom species in which uptake and deposition occur almost simultaneously do not build up a sizeable pool. On the other hand, in *Thalassiosira weissflogii* [Brzezinski, 1994] or *Ethmodiscus* [Villareal, 1999], uptake and deposition are temporally decoupled and the amounts of silica inside the cells completely account for the production of new valves shortly before cytokinesis. However, the calculated concentrations depend on the estimation and measurements of the internal cell water content as well as on the assumption that the silica pool is only existent in the form of monosilicic acid inside the cells. Pool concentrations of 438-638 mM in *Navicula pelliculosa* were reported by Sullivan estimating the cell water concentration to about 20 % (by weight) [Sullivan, 1979]. New direct measurements of the cell water (85 %) and silicic acid content result in intracellular concentrations between 58 and 162 mM for this species [Hildebrand, 2000]. Although the discrepancies are rather large, all results indicate an internal silicon concentration well beyond saturation (1-5 mM) [Iler, 1979] in many diatom species [Martin-Jezequel, 2000] [Martin-Jezequel, 2003]. This large difference between internal and external silicon concentration suggests the existence of a special storage state of the silica accumulated inside the diatom cell. Several concepts are discussed in the literature:

In most cases, the silicon concentration was measured using the molybdate method which is only capable of directly detecting mono- or disilicic acid. [Iler, 1979]. If it is assumed that these test results reflect the true composition of the accumulated silica inside the living cells and it is further assumed that the molybdate test do not change the state of the analyzed samples, then this high monosilicic acid concentration has to be maintained by an interaction of monosilicic acid with other cell components. Werner [1966] and Azam [1974] found that 80 % of the soluble silicon in *Nitzschia alba* was precipitable with trichloroacetic acid suggesting an association and stabilization of the intracellular silica with organic components. However, until now, no organosilicon compound was verified in diatoms except for a very transient and diminutive species identified with liquid-state NMR techniques [Kinrade, 2002](see below). However, it has to be considered that in the case of the molybdate assay, the diatom cells have to be destructed and the intracellular contents are substantially diluted, chemical treated, and, in some cases, heated to 100 °C which may dissolve polymerized forms of silica into molybdate reactive monomeres.

Another possible silicon storage mechanism would be some kind of pre-polymerization of silicic acid inside the cells [Sullivan, 1979]. However, also partially polymerized forms of intracellular silicon would still require some type of stabilization at such high silica concentrations preventing unregulated silica autopolymerization inside the cells. A huge amount of colloidal silica located inside the cytoplasm would disrupt cellular membranes and re-solubilization or transport mechanisms for the polymerized silica inside the living diatoms cells are not uncovered until now. On the other hand, an enzyme (silicase), able to degrade amorphous silica, was found in the demosponge *Suberites domuncula* [Schröder, 2003]. A mechanism which leads to a stabilized silica sol was proposed by Sumper [2004]. He demonstrated that a monosilicic acid solution shows a completely different precipitation behavior in the presence of polyamines and phosphate. Monosilicic acid rapidly polymerizes at neutral *pH* resulting in a sol, which then solidifies to a gel [Iler, 1979]. In a polyamine - phosphate - monosilicic acid system, however, particles with a defined diameter appear within a few minutes. These particles are then prevented from further growth. Furthermore, he showed that such a polyamine stabilized sol could serve as silica source for the formation of silica structures composed of hexagons which are known from valve silica pattern of some diatom species.

Schmid and Schulz [1979] proposed the existence of special silicon-storing vesicles since they observed certain cytoplasmic vesicles fusing with the developing SDV. Such silica containing vesicles were recently found during the formation of the siliceous spicules of sponges [Schröder, 2007]. Until now, however, there is no evidence for the presence of silicon inside these vesicles observed in diatoms. Even if they did contain silica, this silica has also to be stabilized by some mechanism discussed above.

The different silica storing and deposition mechanisms are illustrated in Figure 3-19.

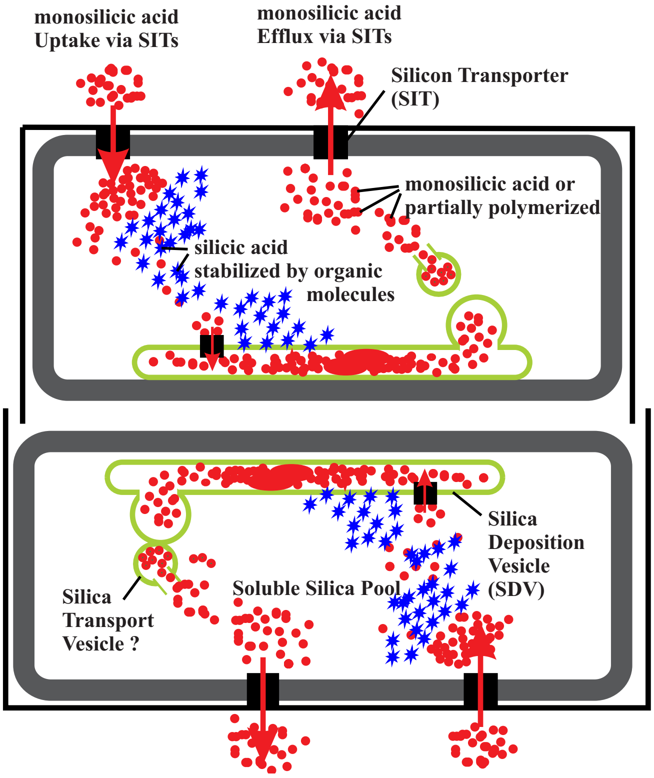

Figure 3-19
Proposed mechanisms of silicic acid uptake, intracellular transport and deposition in dividing diatom cells. Adapted from [Hildebrand, 2000]. The dark outer lines represent the silicified cell walls of the mother cell. The thick grey lines represent the plasma membrane of each daughter cell. All other organelles are labeled in the Figure.

Besides the above mentioned molybdate method, the radioactive isotope analogue ^{68}Ge is used as tracer for Si in radioassay experiments [Chisholm, 1978]. In contrast to the molybdate test, this method can also applied to investigate intact cells but it suffers from the fact that there is no possibility to distinguish between different condensation states of silica or if the silica is bound to organic species. Therefore, neither the molybdate test nor the ^{68}Ge method seem to be qualified to clarify the existence and composition of internal silicon storage pools in diatoms. Owing to the drawbacks of the above mentioned methods, the silicon metabolism of diatoms can, therefore, only be studied on integer, untreated cells. A ^{29}Si liquid-state NMR spectroscopic study on intact diatom cells was carried out by Kinrade et al. [2002]. In this experiment a culture of the freshwater diatom *Navicula pelliculosa* was synchronized by silicon starvation, fed with a ^{29}Si enriched silicate solution and then studied by ^{29}Si liquid-state NMR spectroscopy. Apart from the dominant signal at -71 ppm due to free monosilicic acid, a weak transient signal at -131 ppm was detected only after six hours of silica accumulation. When the initial culture medium was enriched in ^{15}N, the signal at -131 ppm narrowed significantly. Owing to the chemical shift and the narrowing effect, the latter signal was ascribed to an organosilicon complex containing a hexavalent silicon center coordinated to at least one nitrogen atom. But this experiment suffers from two problems: (i) ^{29}Si liquid-state NMR spectroscopy is not able to detect slowly tumbling or immobilized species such as silicic acid attached to organic components or pre-polymerized silicon species. (ii) Besides the control of the cell population and the silicon concentration, no attempt was made to verify the synchronism and development stages of the cell culture. Therefore, an assignment of the observed transient and putative organo-silicon signal to a distinct development stage of the cell is not possible and it remains ambiguous if this silicon species is involved in the silica uptake, storage, or deposition during the silica metabolism of the cell.

Therefore, one goal of this work was the development of a new experiment allowing the examination of the silicon metabolism of diatoms on integer cells. In the following, a new method is presented using solid-state ^{29}Si MAS NMR spectroscopy in combination with confocal laser fluorescence microscopy which is able to give answers about the silica metabolism temporalily related to certain development stages of the dividing cell. Solid-state ^{29}Si NMR spectroscopy in combination with magic angle spinning offers the great advantage to detect all silicon species present in the samples without damaging the cells. Preliminary tests on polysilicic acid solutions (see above) showed that the polymerization state of the silica is changed during the freezedrying of the samples. Therefore, in contrast to former ^{29}Si NMR studies on diatoms (see above), a much gentler method for sample preparation, preventing the application of any freeze-drying or chemical procedure, was used for this experiment.

3.7.1 Experiments on Stephanopyxis turris: Proof of Principles

The first series of experiments was carried out on the diatom species *Stephanopyxis turris*. *Stephanopyxis turris* is known to possess a silica pool composed of monosilicic acid as it was shown by the molybdate test [Martin-Jezequel, 2000] [Martin-Jezequel, 2003].

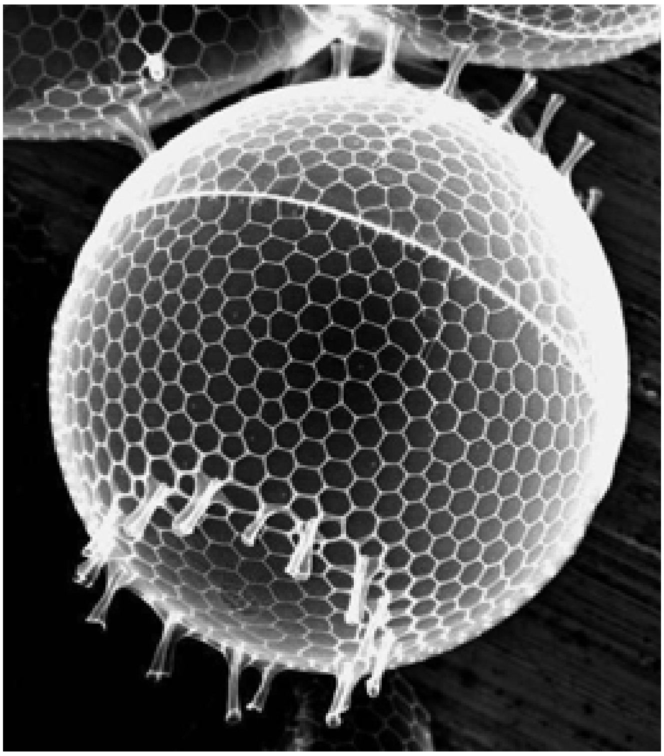

Figure 3-20
Scanning electron microscopic image of the isolated siliceous cell wall of *Stephanopyxis turris*. Image provided by Prof. Dr. M. Sumper, Regensbrug.

The cells were cultivated in two transparent, autoclaved 20 L plastic containers. Initial experiments made use of silicon in natural abundance of ^{29}Si in the culture medium. The initial SiO_2 level in the culture medium was 2 mg/L and the culture was grown until no silicic acid was detected in the medium anymore. In case of *Stephanopyxis turris*, it is difficult to determine the cell concentration in the medium because this species is known to form chains of cells with different lengths which affect the counting procedure. After 48 h, silicon starvation was terminated by the addition of a freshly prepared 96.74 % enriched $Na_2{}^{29}SiO_3$ solution. The growth and development of the cell culture was monitored under the light microscope. After addition of ^{29}Si, the silica concentration increased to about 4.5 mg/L. Subsequently, the culture was kept under normal growth conditions and aliquots of 6 L were harvested in intervals of 2 houres by using a sieve. The sample were then transferred into home-made container insets exactly fitting into a 7 mm MAS NMR rotor and immediately shock-frozen in liquid nitrogen. The MAS rotors were stored at -20 °C until the ^{29}Si MAS NMR spectroscopic measurements were made. The NMR experiments were carried out at ca. 0 °C preventing the samples from unfreezing.

Figure 3-21 shows the progress of the silica concentration as well as the *pH* of the culture medium during the experiment. Owing to the difficulties of the cell counting process, a satisfactory determination of the cell density could not be performed. Therefore, a check of the growth and synchrony of the cell culture was only possible by light microscopy. It was found that the cells are affected by the silica starvation procedure. At the end of the starvation period only single, elongated cells in different developmental stages were observed in the medium. In addition, a lot of the cells exhibit a deformed shape. However, the cells recovered their common shape after addition of fresh silica and cell chains were formed, confirming the onset of growth and cell division in the cell culture.

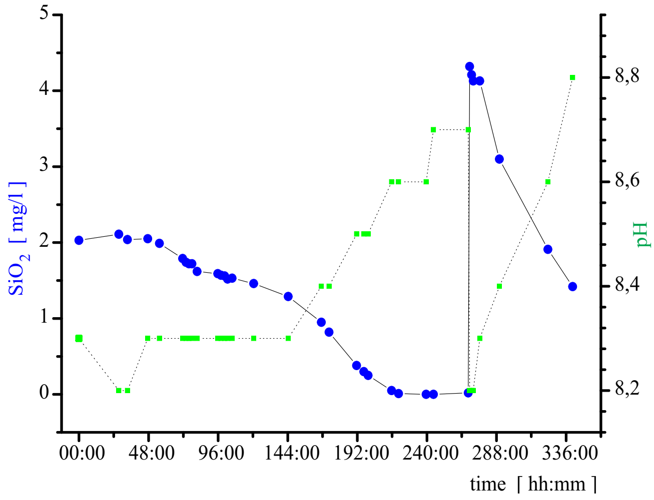

Figure 3-21
Blue: silicon concentration in the culture medium measured by the molybdate test method. Green: *pH* of the culture medium.

Figure 3-22 displays the single-pulse ^{29}Si MAS NMR spectra of the samples collected after ^{29}Si addition. All spectra exhibit the signals characteristic for amorphous silica with signals at δ = -111 ppm (Q^4-groups), δ = -102 ppm (Q^3-groups) and δ = -91 ppm (Q^2-groups) [Engelhardt, 1987]. Strikingly, a sudden increase of the intensities in the spectrum occurs between 6 hours 8 hours. At the same time, the first culture container was emptied and the samples were taken from the second one. Therefore, the differences are assumed to be due to a difference in the growth rate of the two cell cultures.

Nevertheless, this experiment series was the ”proof of principle” showing that it is possible to measure integer diatom cells without any pretreatment of the cells and, therefore, without modifying the silica species inside the cells. However, it turned out that this experiment suffers from two problems. All the spectra exhibit a poor signal to noise ratio although each spectrum takes two days for signal accumulation. One possible way to achieve a better signal to noise ratio is to increase the amount of sample in the MAS rotor. This is accomplished by spinning down the cells directly into the rotor container. A sample of *Stephanopyxis turris* cells was centrifuged 5 min at 4100 g and afterwards examined by light microscopy. The images revealed that *Stephanopyxis turris* cells do not resist the centrifugation process. Most of the cells were damaged and the cell culture did not grow up after transfer into a new culture medium. Therefore, *Stephanopyxis turris* cells are not appropriate for this kind of sample treatment. Furthermore, cell counting of the *Stephanopyxis turris* culture was also not possible due to the above mentioned reasons and the synchrony of the cell culture was also not achieved at the end of the silica starvation period. Therefore, another diatom species was chosen for the next experiment series and a number of improvements of the experimental procedure were made (see below).

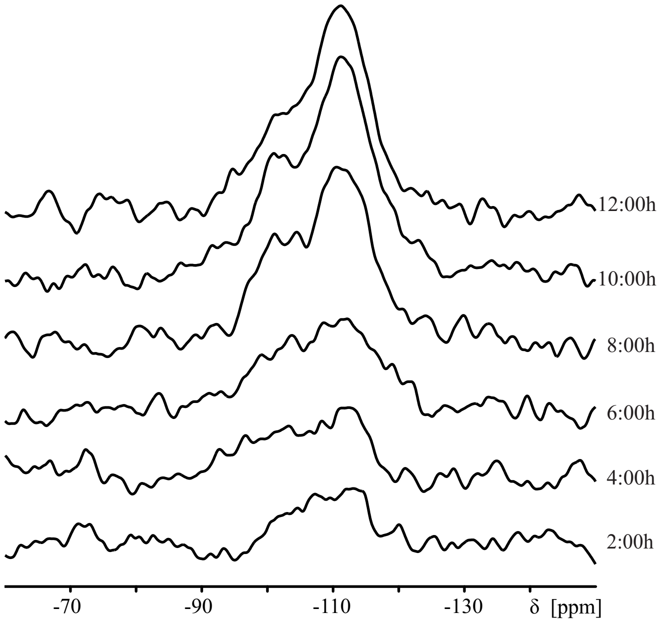

Figure 3-22
Solid-state ^{29}Si NMR spectra of the different developmental stages of dividing diatom cells.

3.7.2 Experiments on Thalassiosira pseudonana

The diatom species *Thalassiosira pseudonana* was chosen for the next series of experiments. Although *Thalassiosira pseudonana* does not belong to the diatoms with the largest known silicon-storage pools, this species has other advantages: The diatom species *Thalassiosira pseudonana* is a well established and characterized model system [Armbrust, 2004] [Sumper, 2008] which is known to be robust enough to withstand the required centrifugation procedure. Centrifugation of the samples cannot be avoided. Despite the fact that ^{29}Si-enriched samples were used, the signal-to-noise ratio of the ^{29}Si MAS NMR spectra is insufficient without centrifugation (see above). As it was shown by Frigeri *et al.* [2006], a centrifuged culture of *Thalassiosira pseudonana* inoculated into fresh artificial sea water continued to grow up. Microscopic investigations have shown that the cells were not damaged under the centrifugal forces (g-forces) applied for the harvesting process. Therefore, diatom cells could be directly centrifuged into the MAS rotors .

The samples were shock-frozen afterwards in liquid nitrogen in order to prevent the silicon species from further condensation. The samples were kept frozen during the entire measurement, also under MAS where the g-forces are higher than during the aforementioned centrifugation procedure. In addition, laser fluorescence microscopic studies were performed to monitor the developmental state of the cell culture and the formation of the new siliceous girdle bands and valves.

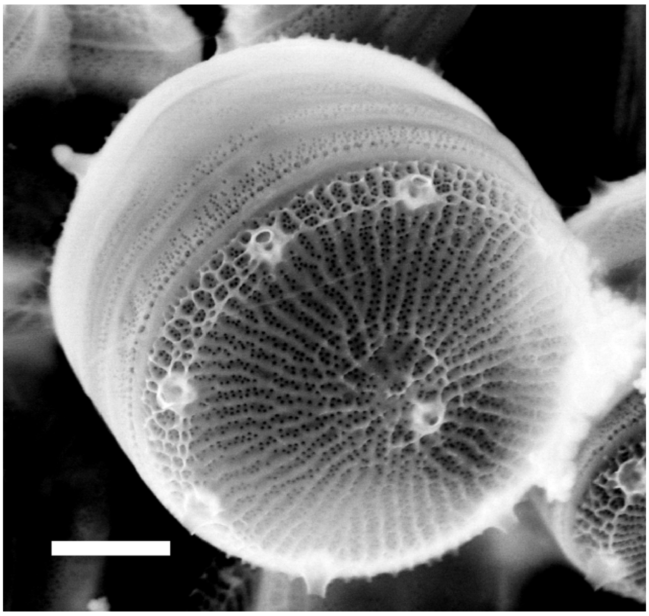

Figure 3-23
Scanning electron microscopic image of isolated cell walls of *Thalassiosira pseudonana*. Scale bar: 1 μm. Image provided by Prof. Dr. M. Sumper, Regensburg.

The diatom species *Thalassiosira pseudonana* was cultured in a 200 L home-made aquarium (fabricated from Gerhard Lehmann) containing 60 L of axenic culture medium. The culture medium used during the starvation phase initially contained ^{28}Si isotope enriched sodium silicate ($Na_2{}^{28}SiO_3$) as silicon source. The initial SiO_2 level in the culture medium was 6.5 mg/L and the culture was grown to a final cell concentration of 10^6 mL^{-1} until no silicic acid was detected in the medium. After 24 h, silicon starvation was terminated by the addition of 20 L of fresh culture medium containing 96.74 % enriched $Na_2{}^{29}SiO_3$ to achieve a final SiO_2 level of 6.2 mg/L and a cell concentration of $7 \cdot 10^5$ mL^{-1} in the culture medium. After termination of the silicon starvation period by the addition of NMR active ^{29}Si, aliquots of 6 L were harvested in intervals of ca. 40 min and centrifuged (in two steps at 0 °C: 15 min at 15,900 g and 5 min at 4100 g) directly into home-made container insets exactly fitting into a 7 mm MAS NMR rotor in order to obtain the highest possible cell density in the rotor. The insets were shock-frozen in liquid nitrogen and stored immediately at -20 °C. For the ^{29}Si MAS NMR studies, the frozen samples were transferred into the pre-cooled MAS probe. This ensures that the shock-frozen samples are kept frozen during the transfer as well as the measurement in order to prevent the silicon species from further condensation. In addition to the ^{29}Si solid-state NMR experiments, the synchronized cell culture was monitored by confocal laser fluorescence microscopy. For this experiment, the fluorescence dye Lyso-Tracker Yellow HCK-123 (Merck) was added to the cell culture shortly before the end of the silicon starvation period. Samples were taken in intervals of ca. 40 min and were examined without further treatment.

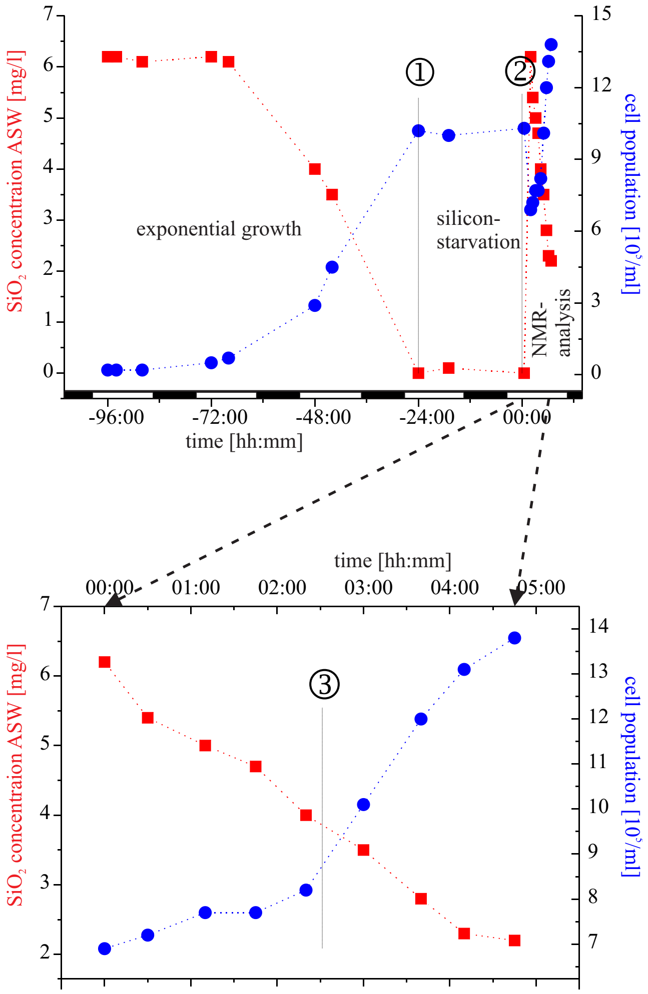

Figure 3-24
Red: silicon concentration in the culture medium measured by the molybdate test method. Blue: growth curve for the algal culture; cell populations were determined with a counting chamber. ① Start of the silicon starvation period. ② End of the silicon starvation period and addition of NMR active ^{29}Si. Note that the measured absolute number of cells is lower than before the addition of fresh culture medium. The decrease is explained by the experimental error of ca. 5% for the counting procedure. ③ Start of cell separation.

The growth curve of the *Thalassiosira pseudonana* cell population and the silicon concentration of the culture medium are shown in Figure 3-24. It shows an increase of the cell population up to a value of 10^6 mL^{-1} after 72 h. At the same time, the silicon concentration in the medium drops down completely (① in Figure 3-24). During the following silicon starvation phase, the cell density remains constant and, due to the lack of silicon, cells are kept in special, silicon dependent states of the cell division cycle [Brzezinski, 1990] [Brzezinski, 1994]. In our experiments, the majority of the diatom population rests in a stage shortly before new frustule formation starts as it was observed for other species [Brzezinski, 1990]. This causes the synchronization of the life cycle which was confirmed by the determination of the cell density and microscopic observations. After 24 h, silicon starvation was terminated by the addition of fresh ^{29}Si enriched culture medium (② in Figure 3-24). Figure 3-24 (bottom) also shows that the cells almost immediately start to take up the freshly added silicon. After a delay of about 2:30 h, cell division and separation rapidly starts (③ in Figure 3-24, bottom).

Figure 3-25 displays the single-pulse ^{29}Si MAS NMR spectra of the samples collected after ^{29}Si addition. A first control sample was taken before the addition of ^{29}Si (Figure 3-25, 0:00 h). All spectra, except for the control sample, exhibit the signal pattern characteristic for hydrated amorphous silica with signals at δ = -111 ppm (Q^4-groups), δ = -102 ppm (Q^3-groups), and δ = -91 ppm (Q^2-groups) [Engelhardt, 1987]. A minor signal at δ = -73 ppm corresponding to monosilicic acid (Q^0) and a weak, transient signal at δ = -121 ppm were detected in one of the spectra (Figure 3-25, bottom: P/H). This signal was assigned to an pentavalent (P) or hexavalent (H) silicon species.

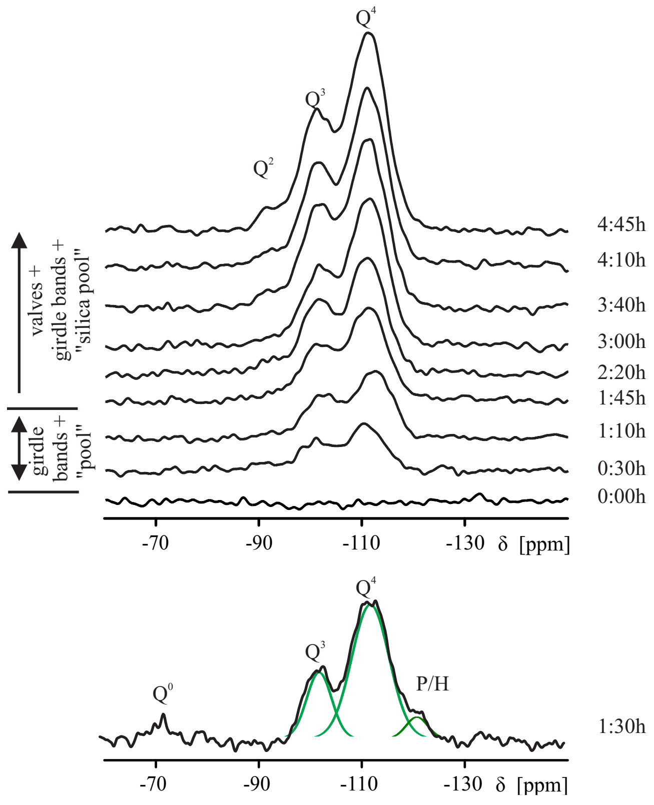

Figure 3-25
Solid-state ^{29}Si NMR spectra of the different developmental stages of dividing diatom cells. Bottom: P/H indicates the NMR signal of five- or six-coordinated silicon atoms.

Figure 3-26 displays the ^{29}Si content of the diatom samples centrifuged into the 7 mm MAS rotor and the silicon amount which was taken up by the diatoms at the same time from the culture medium. The amount of silicon in the MAS rotor was determined by referencing the NMR signals to a SiO_2 standard sample of known weight. The amount of silicon taken up from the culture medium was determined by molybdate tests.

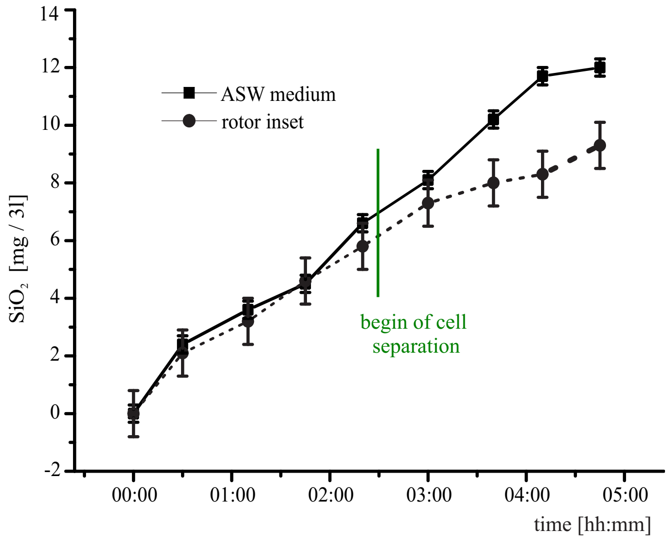

Figure 3-26
Circles/dotted line: time-dependence of the ^{29}Si content inside the MAS rotors measured by quantitative ^{29}Si NMR. Squares/solid line: time dependence of the amount of silicon taken up from the culture medium measured by the molybdate test method.

Samples for fluorescence spectroscopy (Figure 3-27) were taken at 0:30 h, 1:00 h (not shown), 1:30 h, 2:00 h, 2:30 h (not shown), 3:30 h, and 4:30 h (not shown). Both, the auto-fluorescence signals of the chloroplasts (Figure 3-27, red signals, left column) as well as the emitted light of the fluorescence dye (Figure 5, green signals, middle column) were detected simultaneously. The emission bands of both fluorescence signals partially overlap owing to the wide emission range of the chloroplasts. Therefore, signals which are observable in both fluorescence channels are assigned to chloroplasts whereas signals appearing only in the low wavelength area are assigned to the fluorescence dye. After 0:30 h (Figure 3-27, first row), only a few cells were detected which already started to build up new girdle bands. The bulk of the cell culture ($<$ 70 %) did not show any fluorescence due to freshly synthesized silica. For samples taken after 1:00 h or 1:30 h, almost all of the cells exhibited green fluorescence sites (white arrows, Figure 3-27, second row) indicating the synthesis of new girdle bands. After 2:00 h, the formation of new valves started as can be seen from a new fluorescence signal in the middle of the cells (Figure 3-27, third row). The following pictures taken at 2:30 h, 3:30 h, and 4:50 h almost exclusively show cells with freshly synthesized, complete valves ($>$ 90 %). During that time, cells in two different stages of development were simultaneously identified: daughter cells which are still attached to each other (Figure 3-27, fourth row) as well as separated, single daughter cells (image not shown).

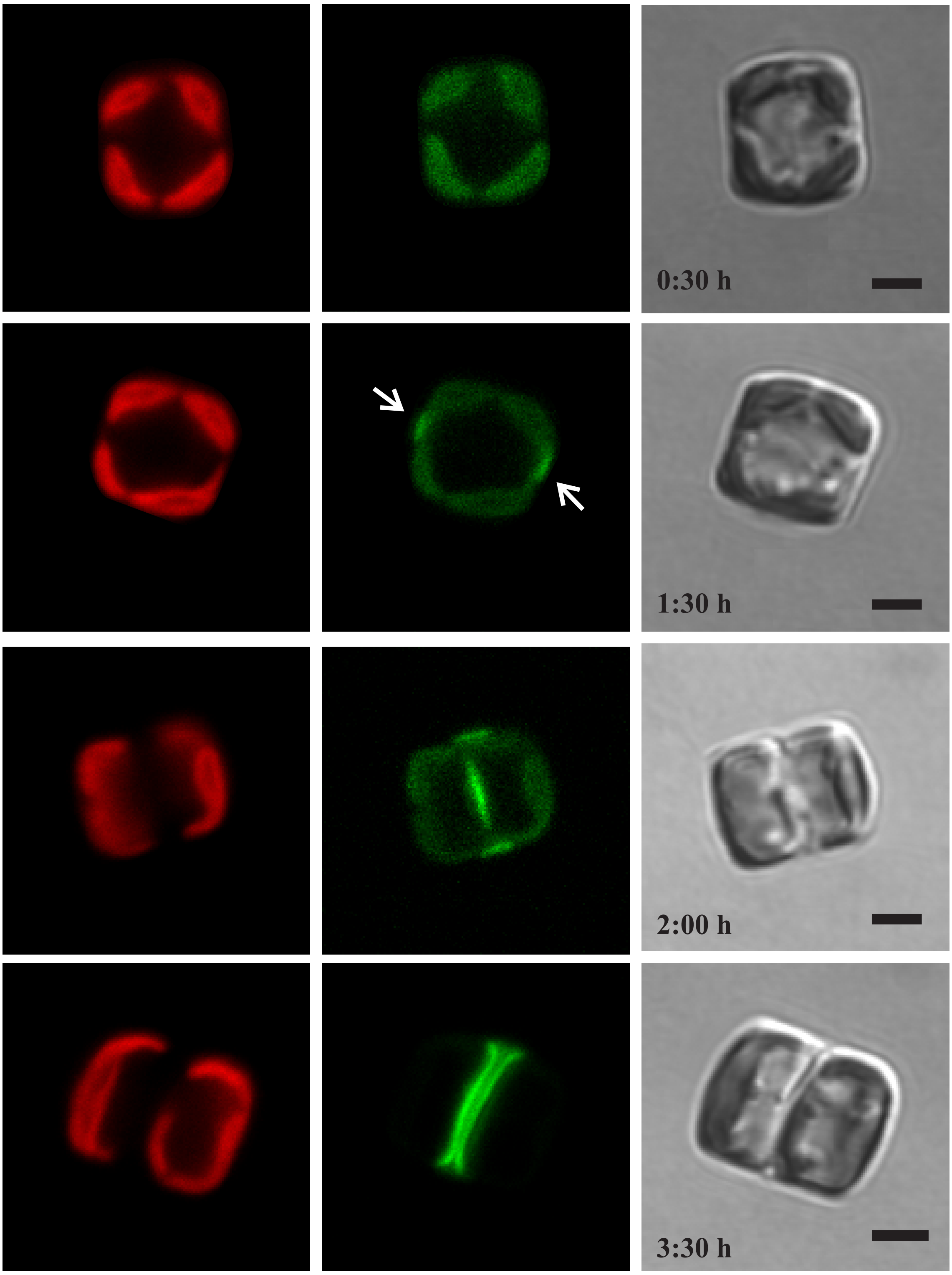

Figure 3-27 Confocal fluorescence microscopic pictures of single diatom cells characteristic for the various developmental stages. Red: auto-fluorescence of the chloroplasts. Green: fluorescence of stained accumulated silica inside the cells (and partially of chloroplasts). Scale bar: 2 μm.

In order to differentiate ^{29}Si NMR signals of the intracellular silicon-storage pool or newly polymerized silica from the ”background” signal of the already existing cell walls which were synthesized before the silicon starvation phase, diatoms were grown up in a ^{28}Si isotope enriched culture medium. After the silicon-starvation period, NMR active ^{29}Si isotope enriched culture medium was added to the culture medium. Therefore, the signals of the Q^n groups in Figure 3-25 are completely assigned to the silicon species formed after the silicon-starvation period. A comparison of fluorescence microscopic pictures (Figure 3-27) with NMR data (Figure 3-25) and growth curves (Figure 3-24) allows an unambiguous assignment of the NMR spectra to the developmental stages of the synchronized diatom culture. Based on these observations, the spectra representing the samples during the first 90 minutes only exhibit signals of the girdle bands and silicon stored within the cells. However, the signals of the following spectra include signals due to silicon located in the girdle bands, silicon possibly stored in a pool as well as newly synthesized valves. A quantitative analysis of the Q^n signals of the different ^{29}Si MAS NMR spectra yields additional information about the degree of condensation and maturation of the silicified cell components. The results of the analysis of the Q^4 and Q^3 groups are displayed in Figure 3-30. It is striking that isolated and purified cell walls exhibit a higher degree of condensation than integer diatoms at all times. The difference is particularly obvious during the first 90 minutes. Bertermann et al. [2003] also detected a difference in the Q^4/Q^3 ratio of complete freeze-dried cells and extracted cell walls. In order to show that the extraction procedure does not influence the chemical state of the cell wall silica, they investigated extracted and purified cell walls of different diatom species by solid-state ^{29}Si NMR using the same purification method as in this work and a gentler method. The solid-state NMR spectra of the two sets of samples did not show any differences relative to each other indicating that the extraction/purification process does not change the cell wall silica chemically. It was, therefore, concluded that the difference in the Q^4/Q^3 ratio seen in Figure 3-30 between integer cells and extracted cell walls is real and not an artifact due to the cell wall extraction procedure. The comparison of the amount of silicic acid taken up from the culture medium (measured with the molybdate method) and the amount of silicon found in the MAS rotors (measured against an external SiO_2 standard) shows that the entire amount of silicic acid taken up from the culture medium is ”NMR-visible” within the experimental error (see Figure 3-26). That means, the ^{29}Si MAS NMR spectra shown in Figure 3-25 represent the entire amount of silicon contained in the cells and the presence of ”NMR-invisible” species can be ruled out. The deviations observed beyond 3 h are due to the fact that cell division rapidly starts at this time. It is then impossible to centrifuge the entire amount of cells collected from the culture medium into the MAS rotor insets, i.e., some material is lost. Molybdate test studies have shown that *Thalssiosira pseudonana* builds up only a relatively small soluble silicic acid pool in contrast to other diatom species [Martin-Jezequel, 2000, and references therein]. The complete absence or small magnitude of the silicic-acid signal at -71 ppm in Figure 3-25 is consistent with these earlier observations. The ^{29}Si NMR chemical shift of monosilicic acid remains almost unchanged if hydrogen bonds as was shown by Sahai and Tossell [2001]. In other words, monosilicic acid hydrogen bonded to organic components of the cell would be indistinguishable from ”free” monosilicic acid in the ^{29}Si NMR spectra. However, monosilicic acid is only observed at an extremely low concentration in just one of the spectra (see Figure 3-25). Monosilicic acid hydrogen bonded to organic compounds can, therefore, be excluded to be a significant and stable silicon-storage pool. That means, monosilicic acid can only exist transiently and must be transformed into other silicon species rapidly after its uptake from the seawater. These considerations are also true for disilicic acid, which gives rise to a characteristic signal at ca. 80 ppm. The aforementioned difference in the Q^4/Q^3 ratio of integer cells and extracted cell walls (see Figure 3-30) indicates the presence of some amount of silicon different from cell wall silica. The corresponding signals would then be superimposed with the signals due to girdle bands and valves as indicated in Figure 3-25. The weak and transient signal observed at -121 ppm (Figure 3-25, bottom) lies outside the common range of four-coordinated silicon species [Engelhardt, 1987] [Christiansen, 2006] and does not occur in the spectra of isolated cell walls of *Thalassiosira pseudonana* (cf. Figure 3-7). It was described by Iler [1979] that the polymerization of silica is likely to proceed via a fugacious higher-coordinated intermediate state. This could explain why the signal is not seen in all spectra (Figure 3-25, top). Therefore, this signal was assigned to a five- or six-coordinated silicon complex (P/H) [Kinrade, 1999] [Sahai, 2002]. That is similar to the signal found by Kinrade et al. [2002] for the diatom *Navicula pelliculosa*. No other signals outside the range of four-coordinated silicon have been detected. Therefore, at the given experimental sensitivity, the existence of stable organo-silicon complexes which are built out of a six-coordinated silicon species or silicon species directly bonded to carbon can be excluded due to the characteristic chemical shifts of these compounds [Kinrade, 1999] [Sahai, 2002]. However, the chemical shift range of four-coordinated silica encompasses also four-coordinated organosilicon complexes with Si-O-C bonds as well as five-coordinated silicon, which are supposed to be part of the silicon metabolism by several authors [Hecky, 1973] [Lobel, 1996] [Kinrade, 2002]. These compounds cannot unequivocally be differentiated from Si-O-Si bound groups solely by the chemical shifts observed in 1D ^{29}Si NMR spectra. However, even if such a complex occurs, it is not present in a uniform state which would give rise to a narrow line in the ^{29}Si NMR spectrum. Moreover, 1D ^{29}Si{^{1}H} cross-polarization (CP) experiments (see Figure 3-9) revealed an identical CP spectrum as it is commonly observed for pure silica [Maciel, 1980]. This indicates that the majority of the silicic acid transported into the *Thalassiosira pseudonana* cells is not stored as a well-defined and stable organo-silicon complex; an observation which does-of course-not exclude the presence of short-lived complexes as intermediate states, in particular for species such as *Navicula salinarum* where the two dimensional expansion of the valves takes place at a time scale of only ca. 15 min [Hazelaar, 2005]. It is, therefore, suggested that the silicic acid rapidly forms pre-polymerized silica species. Silica sols are known to be stabilized by polyamines as it was already demonstrated *in vitro* [Sumper, 2004] (see also section 3.7) and may act as the basis for the development of new girdle bands and valves during the cell division cycle since the presence of polyamines in diatoms was shown earlier [Kröger, 2000]. The silica sol nanospheres would only deliver the common signals due to four-coordinated Q groups in the ^{29}Si NMR spectra. Figure 3-28 shows a ^{29}Si MAS NMR spectrum of a silica precipitate composed of silica nanospheres (precipitate 1) [Sumper, 2004]. The precipitate was obtained by adding a freshly prepared solution of monosilicic acid to a phase-separated poly(allylamine)/phosphate mixture (formed by mixing solutions of sodium phosphate (*pH* 6.8) and poly(allylamine)). Silica formation was allowed to proceed for 12 minutes at 25 °C. The signals appearing in the ^{29}Si MAS NMR spectrum can be assigned to the different Q^n species. Note that the intensity ratio of the Q-group signals is entirely different from that found for extracted cell walls or complete cells (cp. Figure 3-7). The spectra of precipitate 1 is characterized by an huge amount of lower polymerized silica species Q^3 and Q^2.

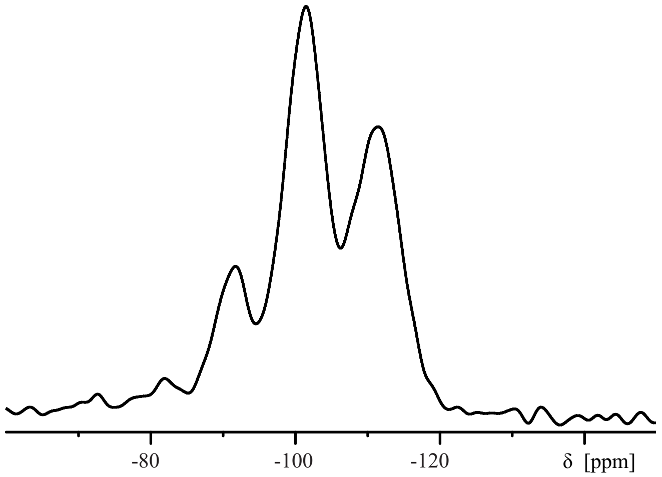

Figure 3-28
Solid-state ^{29}Si NMR spectrum of precipitate 1. The spectrum was recorded by Prof. Dr. E. Brunner at the 750 MHz solid-state spectrometer of the University of Leipzig.

A second precipitate is be prepared by using the polyamine stabilized sol as silica source [Sumper, 2004]. The silica pattern observed by scanning electron microscopy resemble the structure of diatom cell walls. The degree of silica condensation (determined by the Q-group intensity ratio of the spectrum (Figure 3-29) is higher than that of the polyamine stabilized sol and closer to that of natural cell walls.

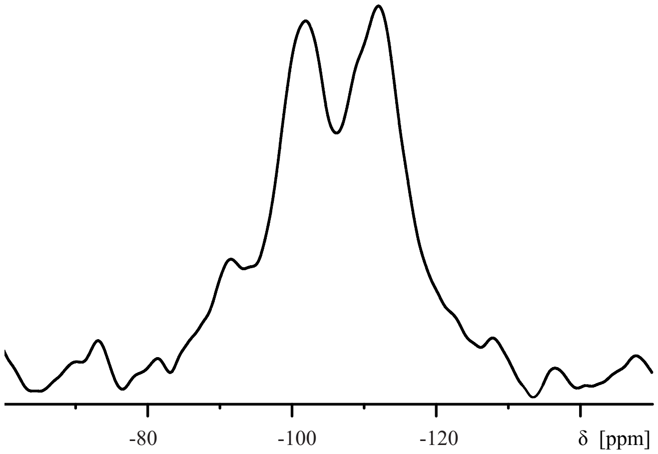

Figure 3-29
Solid-state ^{29}Si NMR spectrum of precipitate 2. The spectrum was recorded by Prof. Dr. E. Brunner at the 750 MHz solid-state spectrometer of the University of Leipzig.

Several authors reported that the siliceous valves of diatoms are built from silica nanospheres [Schmid, 1979] [Crawford, 2001] [Fuhrmann, 2004]. Recently, Hildebrand et al. [2006] observed the formation of network-like cell wall substructures at different scales of structural organization in *Thalassiosira pseudonana* during the process of valve formation. If these substructures consist of pre-condensed silica species – maybe of the aforementioned silica sol particles – the ^{29}Si MAS NMR spectra should exhibit only the common signals in agreement with our observations.

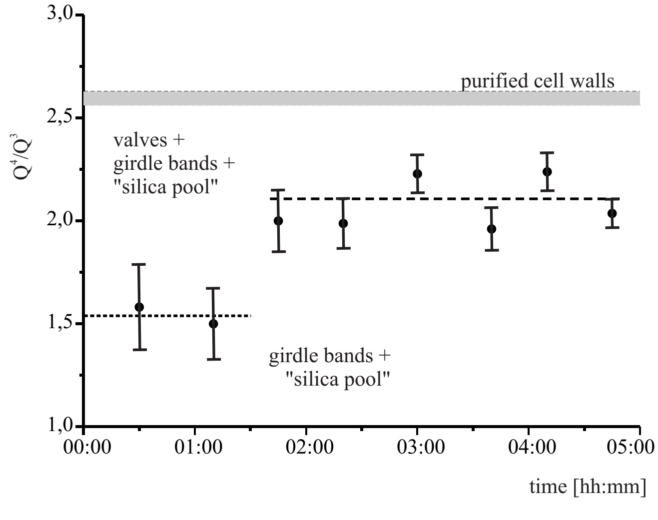

Figure 3-30
Time-dependence of the Q^4/Q^3 group signal intensity ratio determined for the spectra shown in Figure 3-25. The experimental error is indicated. The grey bar on top shows the Q^4/Q^3 ratio measured for extracted cell walls. Note that the width of the bar determines the experimental error which is much lower than for the centrifuged, integral cells due to the much better signal-to-noise ratio obtained for the extracted cell walls.

In summary, the diatom species *Thalassiosira pseudonana* does not store silica in form of well-defined and stable organo-silicon complexes. Instead, the observed ^{29}Si MAS NMR spectroscopic investigations are consistent with the presence of pre-condensed silica species. The described solid-state ^{29}Si NMR spectroscopic technique has been proven to be useful and applicable to study integer diatom cells and will be applied to other diatom species in the future.

4 NMR Spectroscopic Studies of Phosphorus Chalcogenide - Copper Halide Systems

4.1 Introduction

The first part of the present Chapter 4.3-4.7 deals with the nuclear magnetic resonance (NMR) spectroscopic investigation of molecular phosphorus chalcogenide cage compounds P_4X_3 (X = S, Se) and their copper halide CoY (Y = Cl, I, Br) adducts. The structural analysis of such compounds is usually accomplished by single crystal X-ray diffraction methods. Yet, single crystal X-ray analysis can be ambiguous if the studied systems contain nuclei of similar weight as in case of sulfur and phosphorus. Moreover, single and manually separated crystals are used for X-ray diffraction providing only information about a part of the prepared sample. If the sample contains impurities or other phases, single crystal X-ray diffraction will fail to detect such species. Solid-state NMR spectroscopy is an element-selective and quantitative method capable of providing valuable information about the composition of the examined compounds. Additionally, NMR spectroscopy is also applicable to glasses and mixtures of compounds and is also sensitive to dynamic processes. ^{31}P solid-state NMR MAS spectroscopy has proven to be a very valuable tool for the examination of phosphorus-copper systems [Chan, 2001] [Reiser, 2002] [Brunklaus, 2003a] [Brunklaus, 2003b]. In particular, the large and characteristic J-coupling pattern of copper coupled phosphorus atoms provides an unambiguous structural information.

The second part of this chapter (4.8) describes the application of two dimensional singe quantum (SQ) and double quantum (DQ) NMR spectroscopic experiments to phosphorus-sulfur cage systems. Two dimensional ^{31}P solid-state NMR spectroscopic methods and pulse sequences provide a powerful approach by exploiting tailored spin-spin interactions under high resolution MAS conditions and gives detailed information about the structure and connectivity of the analyzed compounds [Iuga, 2007, and references therein]. In most cases, fast MAS is the prerequisite obtaining high resolution spectra in solid-state NMR spectroscopy. At the same time, MAS attenuates anisotropic interactions providing geometrical and structural information of the sample. This drawback can be overcome by using special recoupling pulse sequences in which radio frequency (rf) pulses are applied in synchrony with the sample spinning rate (CRAMPS - combined rotation and multiple pulse spectroscopy [Gerstein, 1996]). In this chapter dipolar (RFDR [Bennett, 1992]) and scalar (R-TOBSY [Chan, 2001] [Reiser, 2002] [Brunklaus, 2003a] [Brunklaus, 2003b]) recoupling sequences are applied and discussed. Furthermore, the application of DQ excitation schemes – scalar (refocused-INADEQUATE [Lesage, 1999] [Fayon, 2002]) and dipolar (POST-C7 [Lee, 1995] [Hohwy, 1998] [Fayon, 2003]) – is demonstrated and discussed.

4.2 General Remarks

All compounds examined in sections 4.3 to 4.7 were prepared and crystallographically analyzed by Andreas Biegerl [Biegerl, 2007a] [Biegerl, 2007b]. Preparation and structural verification of the samples discussed in section 4.8 were made by Diana Hoppe [Hoppe, 2008]. The 1D spectra were acquired by performing simple 90 degree experiments or using rotor-synchronized spin echo experiments to avoid severe baseline distortion. Owing to the long ^{31}P T_1 relaxation times of the measured samples (partially > 60 s), a series of 30 presaturation $\pi/2$-pulses with short delays of 1 μs were applied before the pulse experiments. This permits the implementation of shorter relaxation delays assuring that the spin system exhibits the same starting condition for each consecutive scan which is particularly important in the case of 2D experiments in order to avoid artefacts. All solid-state NMR spectra were referenced using powered solid $NaH_2PO_4 \cdot H_2O$ as an external reference sample. The experiments were conducted on a Bruker Avance 300 spectrometer at 7.05 T corresponding to a Larmor frequency of 121.495 MHz for ^{31}P. The 2.5 mm standard probe (Bruker, Karlsruhe) allows sample spinning rates of up to 35 kHz. Typical ^{31}P $\pi/2$-pulse lengths for single pulse excitation were set to $2.5 - 3.5$ μs. The excitation power was reduced during recoupling experiments according to the permitted duty cycle in order to avoid damages of the probe. The spectra were deconvoluted and fitted using the program DMfit [Massiot, 2002]. The given integrated intensities of the different signals also include the intensities of the spinning sidebands.

4.3 Tetraphosphorus Trisulfide and Tetraphosphorus Triselenide

P_4S_3 was taken as the starting compound for the preparation of the examined compounds $(P_4S_3)(CuI)$, $(P_4S_3)(CuI)_3$, $(P_4S_3)_2(CuCl)_3$, $(P_4S_3)_3(CuCl)_7$, $(P_4S_3)(CuBr)$, and $(P_4S_3)(CuBr)_3$. A commercial sample of P_4S_3 was obtained from Riedel de Häen. It was purified with boiling water and recrystallized from a toluene solution [Biegerl, 2007a] [Biegerl, 2007b]. Figure 4-1 schematically shows a P_4S_3 cage.

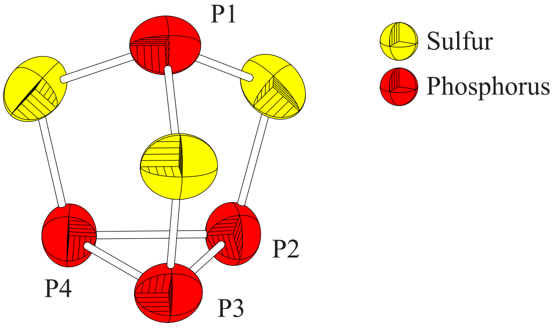

Figure 4-1
The P_4S_3 cage as taken from the crystal structure of $(P_4S_3)(CuI)$. The ellipsoids represent 90 % of the spatial probability distribution of the electrons.

A ^{31}P liquid-state NMR spectrum of P_4S_3 dissolved in carbon disulfide (CS_2) is shown in Figure 4-2. Identification and assignment of the peaks were carried out by the analysis of the J-coupling pattern and by the integrated areas of the two signal groups at $\delta = 65.1$ ppm and $\delta = -125.8$ ppm. The signal at $\delta = 65.1$ ppm exhibits a quartet splitting with relative intensities of 1:3:3:1 indicating a coupling to three magnetically equivalent ^{31}P nuclei (AX_3–system). The other signal group shows a 1:1 doublet splitting corresponding to a coupling to a group of magnetic equivalent spin-1/2 nuclei. The J-coupling constant of both splittings was $^2J(^{31}P,^{31}P) = 70.1$ Hz and the integrated areas of the two signal groups showed a ratio of 1:3.4. Thus, an assignment of the peaks at $\delta = 65.1$ ppm to the apical phosphorus atom P1 and the signals at $\delta = -125.8$ ppm to the three magnetically equivalent basal phosphorus atoms P2, P3, P4 is straightforward (see Table 4-1). The chemical shifts and coupling constants agree very well with the values given in the literature [Blachnik, 1984]. The deviation of the integrated area value 1:3.4 from the expected value of 1:3 of the two signal groups is caused by the use of 30 degree excitation pulses in combination with short repetition delays, which leads to a loss of signal intensity for the apical phosphorus signal at $\delta = 65.1$ ppm due to longer a T_1 relaxation time.

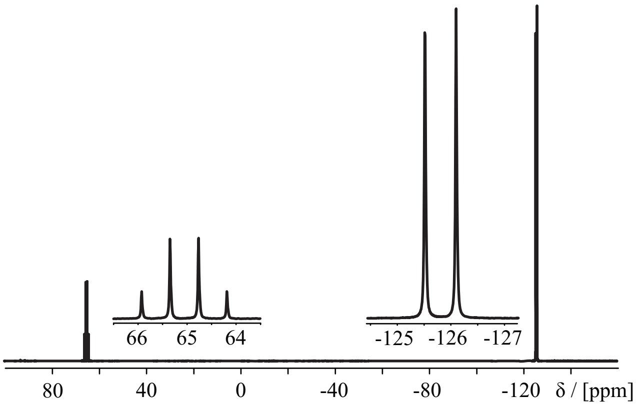

Figure 4-2
^{31}P liquid-state NMR spectrum of P_4S_3 dissolved in carbon disulfide CS_2. The insets show a blow-up of the signal groups. The extracted NMR parameters are summarized in Table 4-1. The spectrum was recorded by the analytical section of the chemical department of the University of Regensburg.

A ^{31}P MAS NMR spectrum of solid powered P_4S_3 was also recorded and is shown in Figure 4-3. Comparison with the ^{31}P liquid-state NMR spectrum and measurement of the integrated areas (1:3) easily allow the assignment (see Table 4-1). Owing to the residual linewidth of more than 200 Hz, a line splitting due to the $^{2}J(^{31}P,^{31}P)$ coupling is neither observed for the signal of the apical phosphorus atom P1 at $\delta = 80.5$ ppm nor for the signal of the three basal phosphorus atoms P2, P3, P4 at $\delta = -102.8$ ppm.

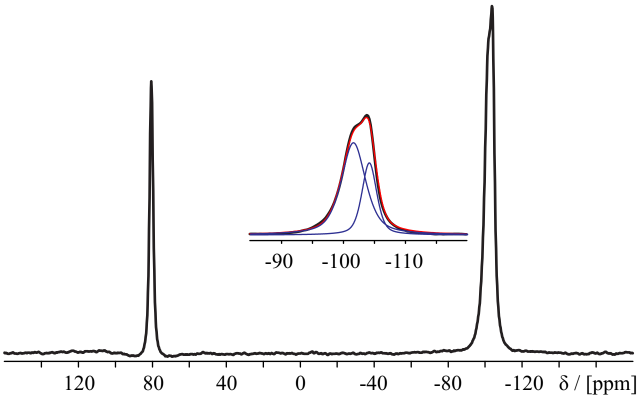

Figure 4-3
^{31}P MAS NMR spectrum of solid pulverized P_4S_3 at a sample spinning rate of 35 kHz and a temperature of T = 295 K. The inset shows a magnification and deconvolution of the upfield range of the spectrum. The extracted NMR parameters are summarized in Table 4-1.

In contrast to previous studies [Eckert, 1989], both phosphorus sites (the apical as well as the basal) are well resolved, even for slow sample spinning rates (Figure 4-4). P_4S_3 is known to undergo a first order phase transition at 314 K from a rigid ordered crystalline phase (α-P_4S_3) to an orientationally disordered plastic phase (β-P_4S_3) [Bougeard, 1998]. The crystal structure of α-P_4S_3 is known to contain two crystallographically inequivalent molecules in the unit cell which were observed in a previous study [Eckert, 1989] by two different and resolved signals in the chemical shift region of the apical atom. In our study, only one signal is seen for the apical phosphorus atom, although the set temperature inside the stator was 295 K which is well below the phase transition point for P_4S_3 of 314 K. The spectral resolution with a line width of 275 Hz is sufficient to resolve the two lines. It is known that high sample spinning rates heat the sample due to air friction. Therefore, the sample could be changed into the β-conformation which shows only one signal for the apical phosphorus atom P1 [Andrew, 1998].

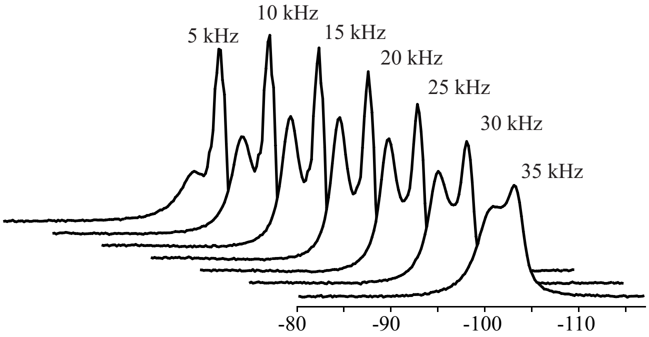

Figure 4-4
Section (basal phosphorus atoms) of the ^{31}P MAS NMR spectra of P_4S_3 for different sample spinning rates.

A deconvolution of the signal of the basal phosphorus atoms at $\delta = -102.8$ ppm suggests the existence of two magnetically non equivalent phosphorus sites at $\delta = -101.6$ ppm and $\delta = -104.1$ ppm (see inset Figure 4-3). This was not seen in previous NMR studies of P_4S_3. Moreover, these signals show a different behavior for different sample spinning rates (Figure 4-4). Figure 4-5 shows spectra of P_4S_3 at T = 275 K (black curve) and T = 310 K (red curve), both at a sample spinning rate of 20 kHz. In contrast to the apical phosphorus peaks of α- / β-P_4S_3 and the basal phosphorus peak of β-P_4S_3, the line broadening of the basal phosphorus peak of α-P_4S_3 (black arrow) is significantly higher. The reason for this behavior is the molecular reorientation of the α-P_4S_3 molecules about their C_3 symmetry axis. As a result of these jumps, the transverse magnetization is not refocused after a full rotor period, and an effective line narrowing due to MAS can not be achieved [Eckert, 1989].

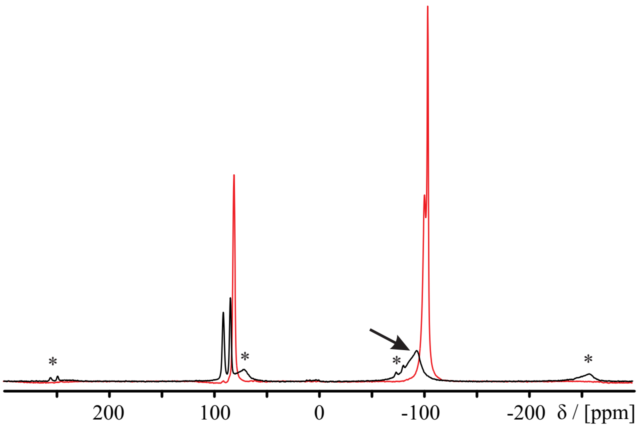

Figure 4-5
Black: Spectrum of α-P_4S_3 at T = 275 K. Red: Spectrum of β-P_4S_3 at T = 310 K. Both at a sample spinning rate of 20 kHz. The spinning sidebands are indicated by asterisks.

P_4S_3		δ [ppm]	J(P,P) [Hz]	%
liquid-state NMR				
	apical	65.1	70.1 (1:2:2:1)	22.7
	basal	-125.8	70.1 (1:1)	77.3
β-P_4S_3				
	apical	80.5	–	25.0
	basal	-104.1	–	75.0
		-101.6		
α-P_4S_3				
	apical	90.4	–	23.5
		83.5	–	76.5
	basal	-93.8	–	

Table 4-1
liquid-state and solid-state ^{31}P NMR parameters of P_4S_3.

P_4Se_3 was used for the preparation of $(P_4Se_3)(CuI)$. Red phosphorus and grey selenium were filled in a silica glass ampoule. The ampoule was air sealed and the mixture was tempered. P_4Se_3 was then purified with chloroform ($CHCl_3$) [Biegerl, 2007c].

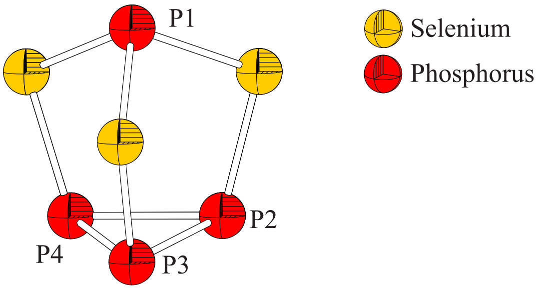

Figure 4-6
The P_4Se_3 cage as taken from the crystal structure of α-P_4Se_3. The ellipsoids represent 90 % of the spatial probability distribution of the electrons.

The liquid-state ^{31}P NMR spectrum of P_4Se_3 dissolved in deuterated benzene (C_6D_6) is shown in Figure 4-7. The overall structure of the spectrum is the same as in case of P_4S_3. Two signal groups are identified: A doublet centered at $\delta = -112.2$ ppm for the three basal phosphorus atoms P2, P3, P4 and a quartet centered at $\delta = 31.8$ ppm for the apical phosphorus atom P1. The assignment was done in the same way as in case of P_4S_3 (see Table 4-2). A J-coupling between the apical and the three basal phosphorus atoms of $^2J(^{31}P,^{31}P) = 71.8$ Hz was measured. Additional satellite peaks due to coupling to the rare selenium 1/2 spins are visible in the spectrum.

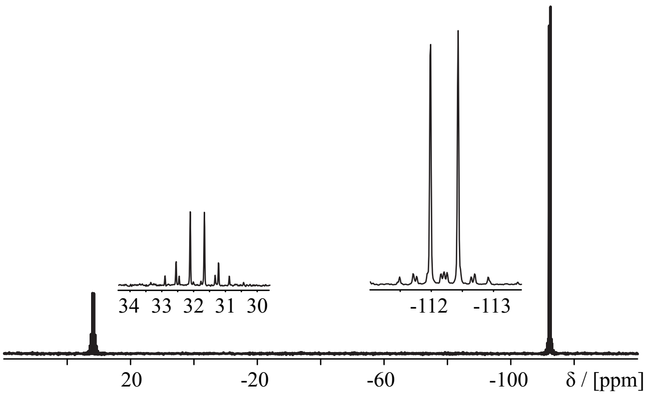

Figure 4-7
^{31}P liquid-state NMR spectrum of P_4Se_3 dissolved in C_6D_6. The insets show a blow-up of the signals. The extracted NMR parameters are summarized in Table 4-2. The spectrum was recorded by the analytical section of the chemical department of the University of Regensburg.

In agreement with the structure, the ^{31}P MAS NMR spectrum of α-P_4Se_3 (Figure 4-8) revealed two different signal groups at $\delta = -67.0$ ppm assigned to the basal phosphorus atoms and at $\delta = 79.2$ ppm assigned to the apical phosphorus atom. According to the two different crystallographic positions of the apical phosphorus atom in the unit cell, two different peaks at $\delta = 81.2$ ppm and $\delta = 77.2$ ppm are visible in the spectrum. Furthermore, a line distortion of the basal peak is apparent. Similar to P_4S_3, solid P_4Se_3 also exists in at least two different phases [Sergi, 1995]. The transition temperature between the ordered, low temperature crystal phase α-P_4Se_3 and the plastic crystalline phase β-P_4Se_3 is 356 K which is significantly higher than the adjusted temperature (T = 295 K) inside the stator.

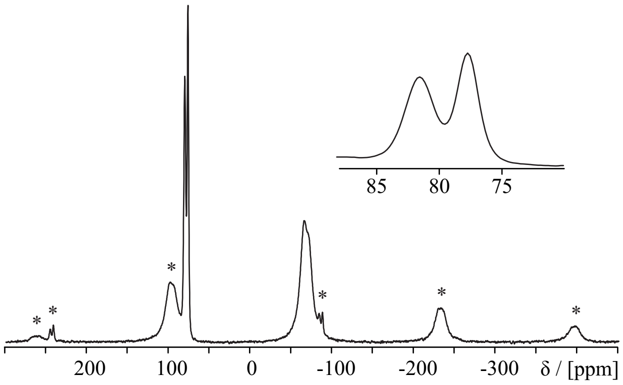

Figure 4-8
^{31}P MAS NMR spectrum of P_4Se_3 at 20 kHz sample spinning rate. The spinning sidebands are marked with asterisks. The inset shows an expansion of the chemical shift region of the apical phosphorus atom.

P_4Se_3	δ [ppm]	J(P,P) [Hz]	%
liquid-state NMR			
apical	31.8	71.8 (1:3:3:1)	24.4
basal	-112.2	71.8 (1:1)	75.6
α-P_4Se_3			
apical	81.2, 77.2	–	24.1
basal (α)	-67.0	–	75.9

Table 4-2
liquid-state and solid-state ^{31}P NMR parameters of P_4Se_3.

4.4 Tetraphosphorus Trisulfide - Copper Iodide Systems

Synthesis and Crystal Structure: The $(P_4S_3)(CuI)_n$ compounds were prepared by layering a solution of P_4S_3 in dichloromethane (CH_2Cl_2) with a solution of CuI in acetonitrile (CH_3CN). A mixture of yellow transparent platelets of the composition $(P_4S_3)(CuI)$ (1) and prisms of the composition $(P_4S_3)(CuI)_3$ (2) has formed within one day. The ratio of the products can be tuned by varying the concentrations of the educts. The compounds were separated manually and their structures were determined by X-ray diffraction [Biegerl, 2007a] [Biegerl, 2007b]:

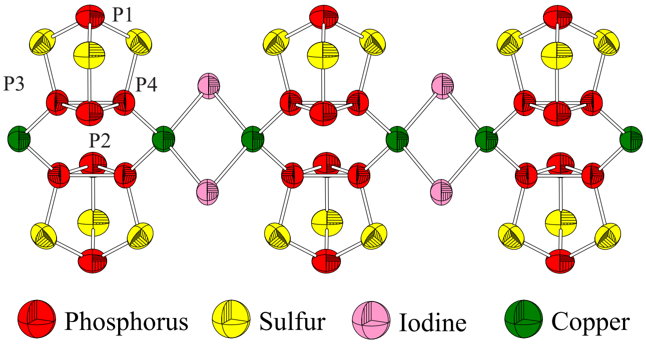

Figure 4-9
Detail of the 1D-structure of $[(P_4S_3)(CuI)]_n$. The chain runs parallel along the crystallographical a-axis. The ellipsoids represent 90 % of the spatial probability distribution of the electrons.

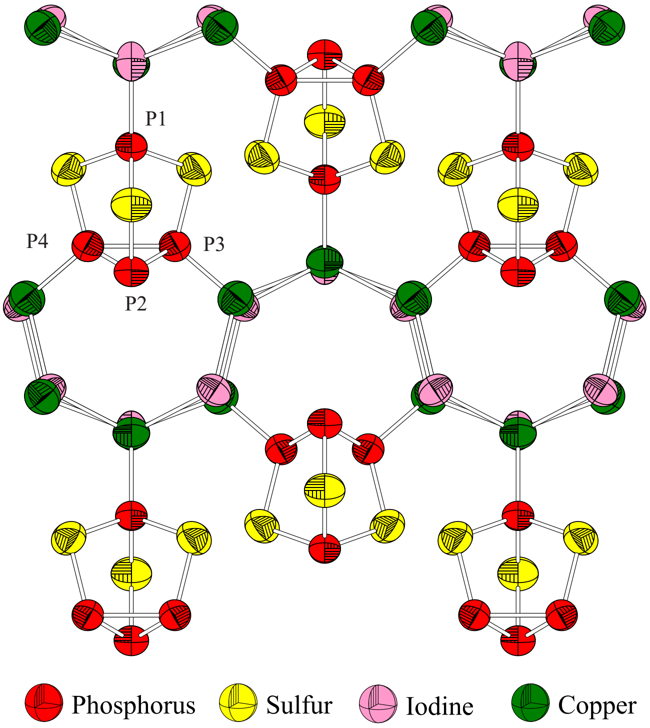

Figure 4-10
A cutout of the structure of $(P_4S_3)(CuI)_3$ seen along the crystallographical c-axis. The ellipsoids represent 90 % of the spatial probability distribution of the electrons.

Compound (1) crystallizes in the orthorhombic space group Cmca with lattice parameters $a = 7.845$ Å, $b = 21.772$ Å, and $c = 10.305$ Å. The structure is composed of linear chains, in which two P_4S_3 molecules serve as bridges for planar Cu_2I_2 rings. ^{31}P solid-state NMR experiments (see Figure 4-11) confirm that the two copper atoms of the Cu_2I_2 rings are connected to two of the three basal phosphorus atoms of (P_4S_3) (see Figure 4-9).

The unit cell of compound (2) exhibits the orthorhombic space group Pnma and the lattice parameters $a = 19.252$ Å, $b = 10.082$ Å, and $c = 7.080$ Å. Viewed along the c-axis, the main structural elements are $[\mathrm{CuI}]_n$ layers that are separated by P_4S_3 molecules (Figure 4-10). The connection between the P_4S_3 molecules and $[\mathrm{CuI}]_n$ layers is established by both, one apical phosphorus atom and two basal phosphorus atoms as it is verified by ^{31}P solid-state NMR spectroscopy (see below) [Biegerl, 2007a] [Biegerl, 2007b].

^{31}P solid-state NMR spectroscopy: ^{31}P solid-state MAS NMR spectra and deconvoluted curves of compound (1) and (2) are shown in Figure 4-11 and 4-12, respectively. The spectrum of compound (1) shows two different signals, located at $\delta = 113.8$ ppm and a superimposed signal group at $\delta = -85$ ppm. The single peak located at $\delta = 113.8$ ppm is assigned to the uncoordinated apical phosphorus atom of the P_4S_3 molecule and is shifted 33.3 ppm downfield with respect to the apical phosphorus atom in the β-P_4S_3 structure. Deconvolution and simulation of the signals located at $\delta = -85$ ppm reveal a multiplet at $\delta = -82.7$ ppm and a single peak at $\delta = -95.3$ ppm (inset Figure 4-11). The typical fourfold J-splitting of the mutliplet with a J-coupling constant $J(\mathrm{Cu,P}) = 912$ Hz indicates the presence of a direct bonding between a basal phosphorus atom and a copper atom. The integrated intensities of the deconvoluted spectrum (see Table 4-3) show that two of the three basal phosphorus atoms are coupled to copper. These results, in combination with the crystal structure, reveal that the sulfur atoms are not bound to copper atoms and that the connection of the P_4S_3 molecules to the CuI rings takes place via a coupling of two basal phosphorus atoms.

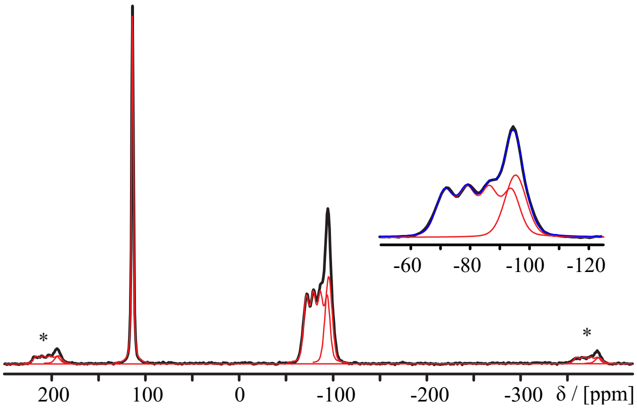

Figure 4-11
^{31}P MAS NMR spectrum of (P_4S_3)(CuI) (black line) and deconvoluted peaks (red lines) at a sample spinning rate of 35 kHz. The spinning sidebands are indicated by asterisks. The good agreement between fit (blue line) and spectrum (black line) is seen at the inset.

The ^{31}P MAS NMR spectrum of compound (2) shown in Figure 4-12 is characterized by two distinct signals at $\delta = 82.2$ ppm and $\delta = -94.9$ ppm.

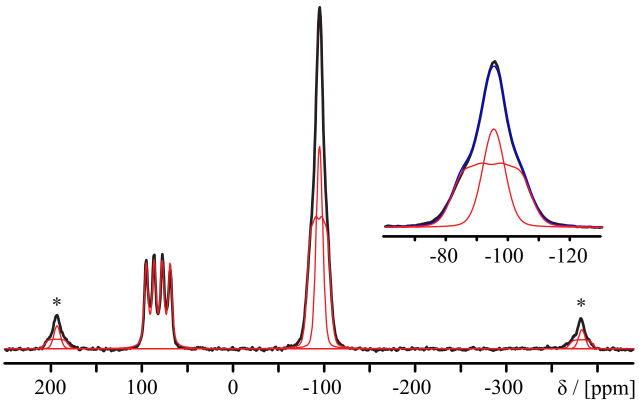

Figure 4-12
^{31}P MAS NMR spectrum of $(P_4S_3)(CuI)_3$ (black line) and deconvolution (red lines) at sample spinning rate of 35 kHz. The spinning sidebands are marked with asterisks. The signal at $\delta = -94.9$ ppm exhibits a broadening of the base which is best fitted by assuming two different peaks at the same chemical shift (see inset).

The multiplet at $\delta = 82.2$ ppm is assigned to the apical phosphorus atom of P_4S_3 due to the characteristic chemical shift which is close (1.7 ppm downfield shifted) to the chemical shift value of β-P_4S_3 (see Table 4-3). Moreover, the J-splitting pattern ($J(Cu,P) = 1067$ Hz) proves the existence of a direct bonding to copper which is consistent with crystallographic data. A closer inspection of the signal at $\delta = -94.9$ ppm reveals a broadening of the NMR signal base suggesting a superposition of signals with the same chemical shift. Indeed, a deconvolution of the line uncovers the existence of a single peak superimposed by a multiplet ($J(Cu,P) = 780$ Hz). Both signals are located at the same chemical shift at $\delta = -94.9$ ppm. The simulation and integration (see Table 4-3) is in agreement with the crystallographic results, which predict the coupling of two magnetically equivalent atoms to the $[CuI]_n$ network.

	δ [ppm]	J(P,P) [Hz]	%
(1) $(P_4S_3)(CuI)$			
P1	113.3	-	24.6
P2	-95.3	-	21.8
P3/P4	-82.7	912	53.5
(2) $(P_4S_3)(CuI)_3$			
P1	82.2	1067	25.5
P2	-94.9	-	27.8
P3/P4	-94.9	780	46.7

Table 4-3
solid-state ^{31}P NMR parameters of $(P_4S_3)(CuI)$ and $(P_4S_3)(CuI)_3$.

4.5 Tetraphosphorus Trisulfide - Copper Chloride Systems

Synthesis and Crystal Structure: Solutions of P_4S_3 dissolved in dichloromethane (CH_2Cl_2) and CuCl dissolved in acetonitrile (CH_3CN) were layered within a narrow tube. After the diffusion-process, bright yellow needles of the composition $(P_4S_3)_3(CuCl)_7$ (3) and transparent yellow platelets of the composition $(P_4S_3)_2(CuCl)_3$ (4) were obtained. The ratio of the products (3) and (4) could be varied by changing the ratio of the educts P_4S_3 and CuCl. Sulfur elemental analysis shows that the compounds were not absolutely pure and traces of the other educts are also present in the sample [Biegerl, 2007a] [Biegerl, 2007b]. The ratio of both compounds was determined by ^{31}P MAS NMR spectroscopy and sulfur elemental analysis.

Compound (3) crystallizes in the trigonal space group P31c. The 3D structure is formed by stacks of P_4S_3 cages interconnected by three differently coordinated types of copper atoms. One edge of the cage is connected to a stack of hexagonal $(CuCl)_3$ rings, and the other is connected to planar ribbons of CuCl. The third coordination of the P_4S_3 cage is built by a chain of $(CuCl)_n$ which possess a threefold symmetry seen along the c-axis (Figure 4-13)

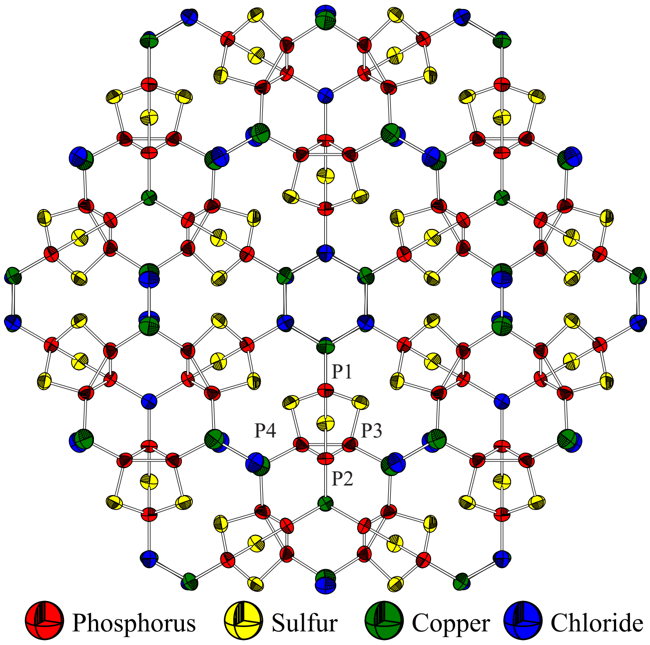

Figure 4-13
Representation of the structure of $(P_4S_3)_3(CuCl)_7$ seen along the crystallographical c-axis. The ellipsoids represent 90 % of the spatial probability distribution of the electrons.

Compound (4) has an orthorhombic unit cell with space group Pmna. Unlike compound (3), the P_4S_3 cages of (4) are connected by three edges to CuCl ribbons. The crystal structure is shown in Figure 4-15.

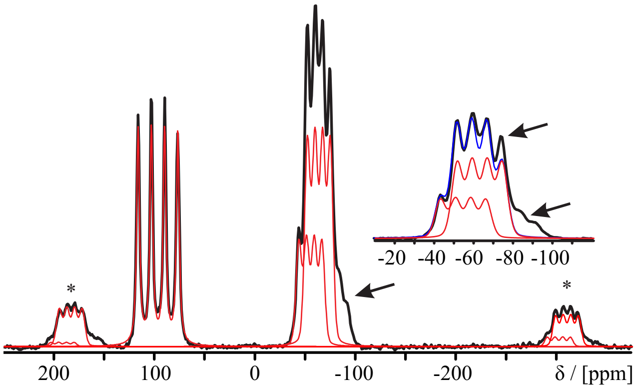

Figure 4-14

^{31}P MAS NMR spectrum of $(P_4S_3)_3(CuCl)_7$ (black line) and deconvolution (red lines) at a sample spinning rate of 30 kHz. The spinning sidebands are marked with asterisks. The arrows indicate trace amounts of compound (4) $(P_4S_3)_2(CuCl)_3$. The inset shows a magnification of the chemical shift section of the basal phosphorus atoms.

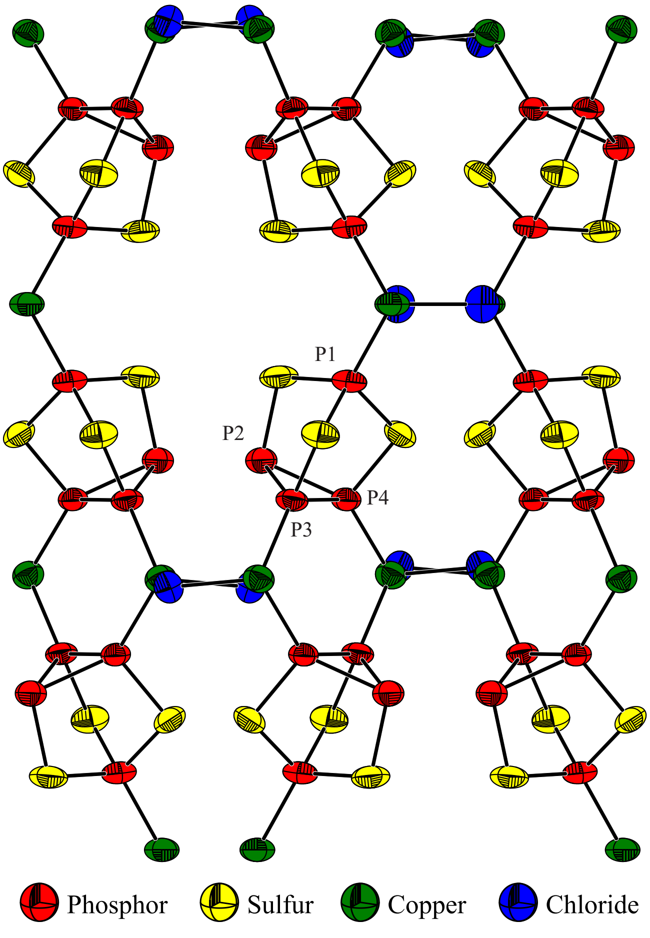

Figure 4-15

X-ray structure of $(P_4S_3)_2(CuCl)_3$ seen along the crystallographical a-axis. The ellipsoids represent 90 % of the spatial probability distribution of the electrons.

^{31}P solid-state NMR spectroscopy: The spectrum of (3) is shown in Figure 4-14. The quartet at $\delta = 97.0$ ppm is assigned to the apical phosphorus atom of the P_4S_3 cage. It is 16.5 ppm downfield shifted with respect to β-P_4S_3. The simulated J coupling J(Cu,P) amounts to 1600 Hz and indicates a direct coupling between the apical phosphorus atom and a copper atom. Deconvolution and fitting of the other signal at $\delta = -63.0$ ppm reveal a superposition of two quartets at $\delta = -55.0$ ppm ($J(\mathrm{Cu,P}) = 935$ Hz) and $\delta = -63.1$ ppm ($J(\mathrm{Cu,P}) = 925$ Hz) with an integrated intensity ratio of 1:2. The fitting results (see Table 4-4) of the spectrum agree with the crystallographic data and verify that the P_4S_3 cage of compound (3) is connected by all four phosphorus atoms to copper atoms. This is the first report of such a coordination [Biegerl, 2007a]. The spectrum shows that the sample of (3) also contains some other phosphorus species, which are labeled with black arrows. This substance is identified as compound (4) by fitting the spectrum with the ^{31}P solid-state NMR parameters extracted from compound (4) and sulfur elemental analysis.

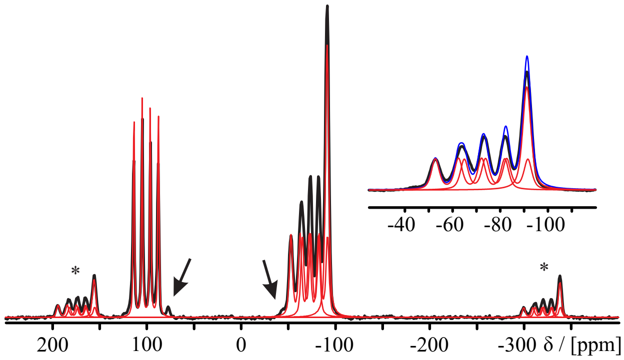

Figure 4-16
^{31}P MAS NMR spectrum of $(P_4S_3)_2(CuCl)_3$ (black line) and deconvolution (red lines) at a sample spinning rate of 30 kHz. The spinning sidebands are marked with asterisks. The arrows indicate trace amounts of compound $(P_4S_3)_3(CuCl)_7$. The inset shows a magnification of the basal chemical shift section. Blue line: Fitted curve.

The spectrum of compound (4) is presented in Figure 4-16. The single quartet at $\delta = 100.8$ ppm is assigned to the apical phosphorus atom which exhibits a $J(\mathrm{Cu,P})$ coupling of 1055 Hz to the bound copper atom. Deconvolution and fitting of the remaining signal group located at $\delta = -75$ ppm reveals a superposition of three distinct signals. Two of them at $\delta = -67.3$ ppm and $\delta = -78.3$ ppm possess a quartet pattern with $J(\mathrm{Cu,P}) = 1180$ Hz and $J(\mathrm{Cu,P}) = 1080$ Hz, respectively. These peaks are assigned to two copper bound basal phosphorus atoms. Interestingly, the chemical shift as well as the coupling constant of both coupling phosphorus atoms are different. The remaining area of this signal group is fitted by a single peak at $\delta = -91.1$ ppm and is assigned to one unbound basal phosphorus atom of the P_4S_3 cage. This assignment is further supported by the integrated area ratio of 1:1:1:1 of the four identified signals (see Table 4-4).

	δ [ppm]	J(P,P) [Hz]	%
(3) $(P_4S_3)_3(CuCl)_7$			
P1	97.0	1600	27.6
P2	-55.0	935	22.1
P3/P4	-63.1	925	50.3
(4) $(P_4S_3)_2(CuCl)_3$			
P1	100.8	1055	23.2
P2	-67.3	1180	26.9
P3	-78.3	1080	26.0
P4	-91.1	-	23.9

Table 4-4
solid-state ^{31}P NMR parameters of $(P_4S_3)_3(CuCl)_7$ and $(P_4S_3)_2(CuCl)_3$.

The obtained NMR data agree with the crystallographic results and show that the sulfur atoms do not participate in the bonding to the connecting CuCl units also in this case. Sulfur elemental analysis reveals that the sample contains some impurities which are also visible in the ^{31}P MAS NMR spectrum (labeled by an asterisk). The byproduct is identified as compound (3) due to its known chemical shifts and J-coupling values.

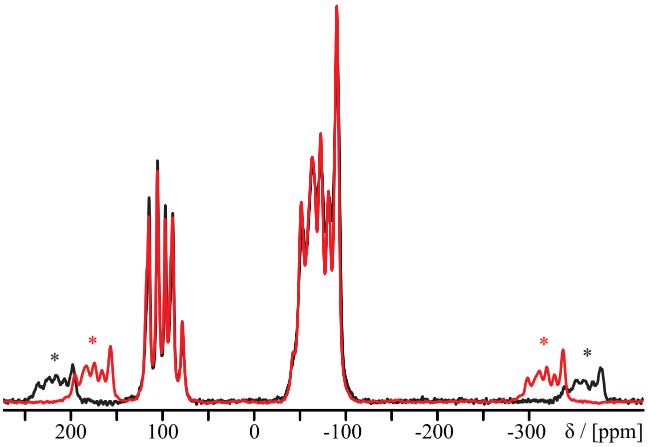

Figure 4-17
Black line: ^{31}P MAS NMR spectrum of a mixture of $(P_4S_3)_3(CuCl)_7$ and $(P_4S_3)_2(CuCl)_3$ at a sample spinning rate of 35 kHz. Red Line: Sum-spectrum of compounds $(P_4S_3)_3(CuCl)_7$ (Figure 4-14) and $(P_4S_3)_2(CuCl)_3$ (Figure 4-16) with a ratio of 40% to 60%.

Another sample was obtained by preparing a mixture of the starting solvents with a P_4S_3 / CuCl ratio of 1:2. Fitting the spectrum with the fitting parameters obtained for compound (3) and (4) (Figure 4-17) results in a good agreement with the original spectrum. Thus the ratio of (3) / (4) in the mixture sample was determined to be 40 % / 60 % which is also in agreement with sulfur elemental analysis.

4.6 Tetraphosphorus Trisulfide - Copper Bromide Systems

Synthesis and Crystal Structure: The compounds $(P_4S_3)(CuBr)$ and $(P_4S_3)(CuBr)_3$ were obtained by layering solutions of P_4S_3 dissolved in dichloromethane (CH_2Cl_2) and CuBr dissolved in acetonitrile (CH_3CN) within a narrow tube. After three days, clusters of light yellow needles of the composition $(P_4S_3)(CuBr)$ (5) deposited at the glass wall of the tube. Furthermore, an orange crystalline deposition was obtained which was analyzed by X-ray diffraction and found to be $(P_4S_3)(CuBr)_3$ (6). Until now, both substances could not be synthesized in their pure form. Crystal structure analysis was done by separating the compound manually and taking one small single crystallite of each [Biegerl, 2007b] [Biegerl, 2007c]. The proposed structures of compound (5) and (6) are shown in Figure 4-18 and 4-19, respectively. It is assumed that they possess the same overall structure as the corresponding compounds (1) and (2) [Biegerl, 2007c].

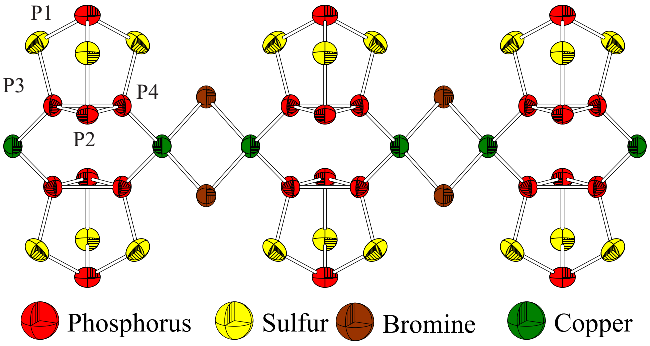

Figure 4-18
Detail of the 1D-X-ray-structure of $(P_4S_3)(CuBr)]$. The chain runs parallel along the crystallographical a-axis. The ellipsoids represent 90 % of the spatial probability distribution of the electrons.

^{31}P solid-state NMR spectroscopy: A spectrum of a mixture of compound (5) and (6) is shown in Figure 4-20. The molar ratio of both substances (5):(6) is determined by sulfur elemental analysis to be 7:3. The spectrum offers two signal groups: One quartet located at $\delta = 100.4$ ppm and a superposition of signals at $\delta = -67$ ppm. Owing to the similar structure, fitting of this spectrum with the parameters used for compound (1) and (2) should have been possible but failed. The signal of the apical phosphorus atom at $\delta = 100.4$ ppm should be composed of a quartet due to the coupling phosphorus atom of compound (6) and a single peak due to the non-coupling phosphorus atom of compound (5) with an integrated intensity ratio of 3:7. Only a quartet ($J(Cu,P) = 1405$ Hz) is visible in the spectrum. In line with the non-coupling apical phosphorus atom, the one non-coupling phosphorus atom of the basis should also lead to an identifiable single peak component in the signal group at $\delta = -67$ ppm.

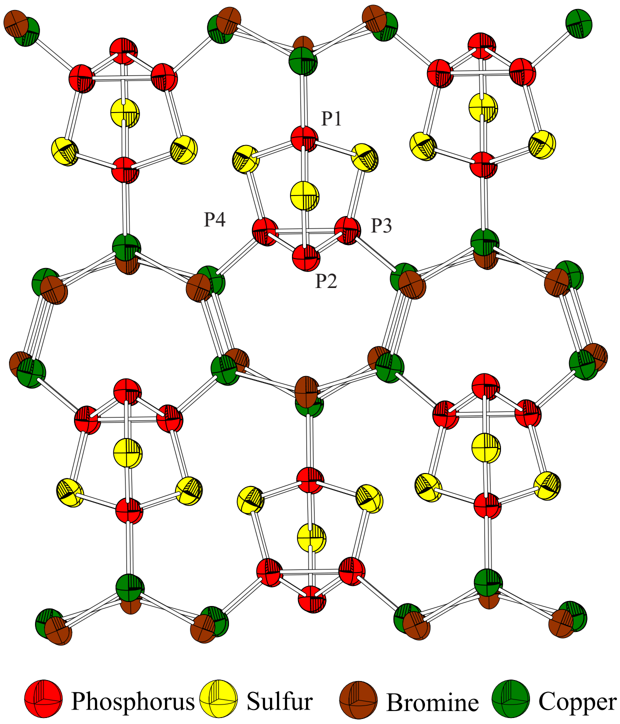

Figure 4-19
Projection of $(P_4S_3)(CuBr)_3$ crystal structure along the c-axis. The ellipsoids represent 90 % of the spatial probability distribution of the electrons.

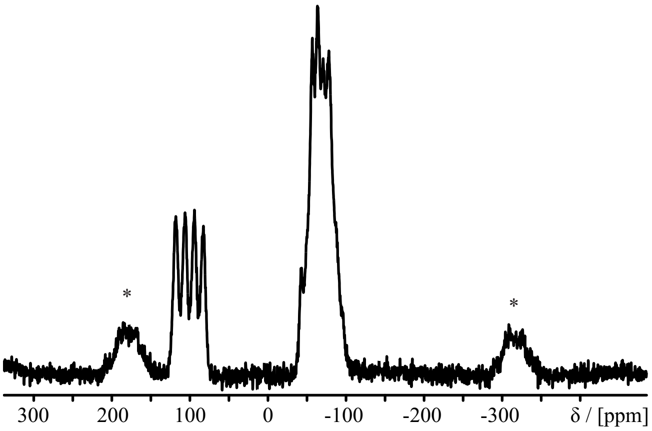

Figure 4-20
^{31}P MAS NMR spectrum of a mixture of $(P_4S_3)(CuBr)$ and $(P_4S_3)(CuBr)_3$ at a sample spinning rate of 30 kHz. The spinning sidebands are marked with asterisks. A deconvolution of the spectrum which is consistent with the crystal-structure was not possible.

However, these single peak components could not be identified in the spectrum. Hence, a reasonable deconvolution of the spectrum consistent with the x-ray structure was not possible. The reason for the failure of fitting the spectra could be the existence of impurities within the sample which could not be identified by single crystal analysis.

4.7 Tetraphosphorus Triselenide - Copper Iodide Systems

Synthesis and Crystal Structure: $(P_4Se_3)(CuI)$ (7) is obtained by layering a solution of P_4Se_3 dissolved in dichloromethane (CH_2Cl_2) with a solution of CuI dissolved in acetonitrile (CH_3CN). A proposed structure of compound (7) is presented in Figure 4-21.

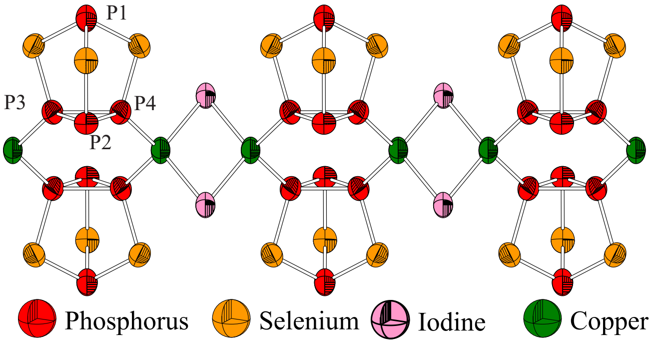

Figure 4-21
Proposed structure element of $(P_4Se_3)(CuI)$. The chain is parallel to the a-axis. The ellipsoids represent 90 % of the spatial probability distribution of the electrons.

^{31}P solid-state NMR spectroscopy: Figure 4-22 represents the ^{31}P MAS NMR spectrum of compound (7). It shows two different signals, one located at $\delta = 52.8$ ppm and another superimposed signal group at $\delta = -85$ ppm. The quartet located at $\delta = 52.8$ ppm is assigned to the copper coupled apical phosphorus atom of the P_4Se_3 molecule. The best fit of the signal group at $\delta = -85$ ppm is obtained by simulating a single peak at $\delta = -67.9$ ppm and two quartets at $\delta = -99.8$ ppm and $\delta = -72.9$ ppm, respectively. All three split signals exhibit the same J-coupling constant of $J(Cu,P) = 870$ Hz.

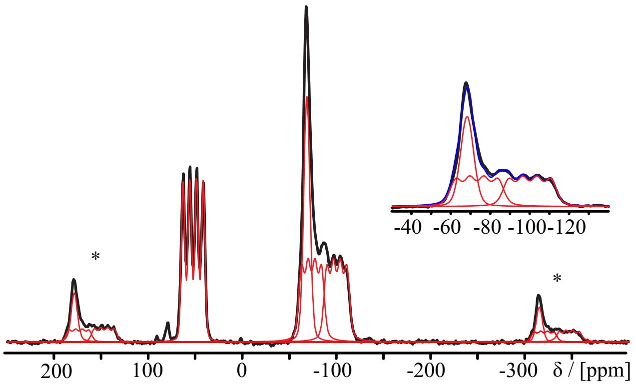

Figure 4-22
^{31}P MAS NMR spectrum of $(P_4Se_3)(CuI)$ at a sample spinning rate of 30 kHz. The spinning sidebands are marked with asterisks. The inset shows a magnification of the basal phosphorus chemical shift section of the spectrum.

The NMR fit results are not in agreement with the proposed crystal structure of $(P_4Se_3)(CuI)$ (Figure 4-21). In fact, the data suggest the existence of another compound in the sample which has a similar structure as $(P_4S_3)(CuI)_3$.

$(P_4Se_3)(CuI)$	δ [ppm]	J(P,P) [Hz]	%
P1	52.8	870	26.1
P2	-67.9	-	24.3
P3	-99.8	870	25.1
P3	-72.9	870	24.5

Table 4-5
solid-state ^{31}P NMR parameters of $(P_4Se_3)(CuI)$.

4.8 Phosphorus Sulfide - Tantalum Chloride system

Synthesis and Crystal Structure: Phosphorus (Hoechst, ultra pure) and sulphur (Alfa Aesar, 99.9995 %) in ratios of P : S = 4 : 4 and 4 : 5 were heated up to 330 °C for two days, then cooled down. The brittle yellow mass formed was ground and used without further purification. Under dry conditions, the phosphorus sulphide mixtures and Ta_2Cl_{10} (HC Starck, 99.999 %) were filled into Schlenk flasks. CS_2 (Aldrich, $>$ 99 %, distilled from P_4O_{10}) and *n*-hexane (Acros, 95 %, distilled from Na_2SO_4) were added. After several weeks at room temperature the liquid phases were removed. Beside greenish-yellow columnar crystals of $(TaCl_5)_2(\beta\text{-}P_4S_4)$ light-yellow platelike crystals of $(TaCl_5)(\alpha\text{-}P_4S_5)$ were separated from the residue. A picture of the basic unit of the single crystal – the $(TaCl_5)_2\beta\text{-}(P_4S_4)$ molecule – is shown in Figure 4-23. The (P_4S_4) cage is connected to two $(TaCl_5)$ units by two of the three basal phosphorus atoms.

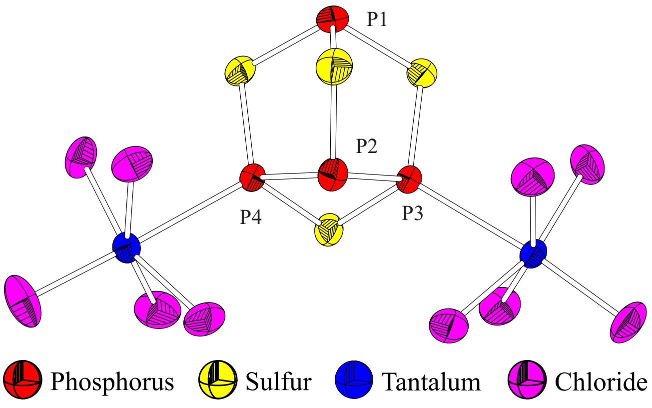

Figure 4-23
$(TaCl_5)_2\beta\text{-}(P_4S_4)$ molecule as taken from the crystal structure of $(TaCl_5)_2\beta\text{-}(P_4S_4)$. The ellipsoids represent 50 % of the spatial probability distribution of the electrons .

The assignment of the signals was done on a ^{31}P liquid-state NMR spectrum (Figure 4-24). The spectrum reveals three resonance groups at $\delta = 216.7$ ppm, $\delta = 168.2$ ppm, and $\delta = 94.1$ ppm. Owing to the J-splitting-pattern and the integrated area ratios of the peaks (given in Table 4-6), the signals are assigned to the apical phosphorus atom P1 at $\delta = 216.7$ ppm, the middle basal phosphorus atom P2 at $\delta = 94.1$ ppm and the two basal phosphorus atoms P3/P4 connected to the ($TaCl_5$) groups at $\delta = 168.2$ ppm. A J-coupling pattern is not seen in the ^{31}P solid-state MAS NMR experiment (Figure 4-25). However based on the similar chemical shifts in the ^{31}P liquid-state NMR spectrum and the integrated area ratio, the assignment is transferred to the ^{31}P solid-state MAS NMR spectrum (see Table 4-6).

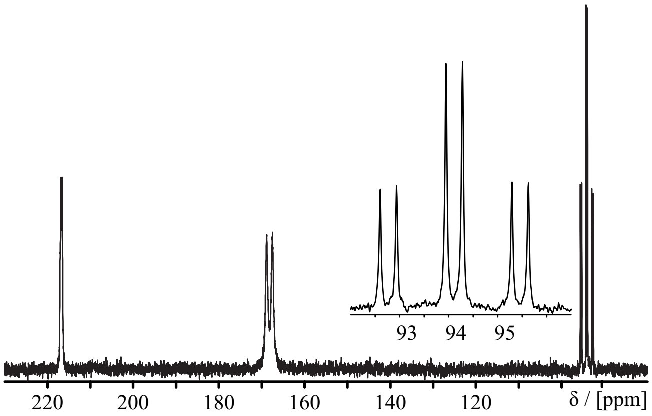

Figure 4-24
^{31}P liquid-state NMR spectrum of $(TaCl_5)_2\beta$-(P_4S_4) dissolved in carbon disulfide. The insets show a blow-up of the signal group of the middle, basal phosphorus atom. The extracted NMR parameters are summarized in Table 4-6. The spectrum was recorded by the analytical section of the chemical department of the University of Regensburg.

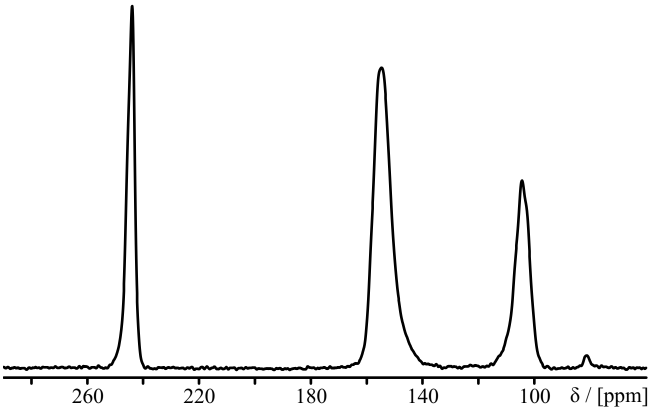

Figure 4-25
^{31}P MAS NMR spectrum of $(TaCl_5)_2\beta$-(P_4S_4) at a sample spinning rate of 25 kHz.

	δ [ppm]	J(P,P) [Hz]	%
liquid-state NMR			
P1	216.7	$^2J(P1,P2) = 22.0$ $^2J(P1,P3/P4) = 54.4$	26.5
P2	94.1	$^2J(P2,P1) = 22.0$ $^1J(P2,P3/P4) = 217.8$	21.6
P3/P4	168.2	$^2J(P3/P4,P1) = 54.4$ $^1J(P3/P4,P2) = 217.8$	51.9
solid-state NMR			
P1	244.0	–	24.9
P2	104.5	–	25.2
P3/P4	154.9	–	49.9

Table 4-6
^{31}P NMR parameters of $(TaCl_5)_2\beta$-(P_4S_4).

The $(TaCl_5)(\alpha\text{-}P_4S_5)$ molecule is shown in Figure 4-26. Unlike $(TaCl_5)_2\beta\text{-}(P_4S_4)$, the phosphorus sulfide cage is only connected to one $(TaCl_5)$ molecule and this connection is linked via a sulfur atom [Hoppe, 2008]. Therefore it is expected that the chemical equivalence of the two basal phosphorus atoms P3 and P4 is abolished. This is verified in the ^{31}P liquid-state (Figure 4-27) and ^{31}P solid-state MAS NMR spectrum (Figure 4-28) where two different signal groups for the P3 and P4 phosphorus atom are identified. In case of the ^{31}P liquid-state NMR spectrum (Figure 4-27) these signals appear at $\delta = 148.0$ ppm and $\delta = 142.6$ ppm and for the ^{31}P solid sate MAS NMR spectrum at $\delta = 165.0$ ppm and $\delta = 157.8$ ppm.

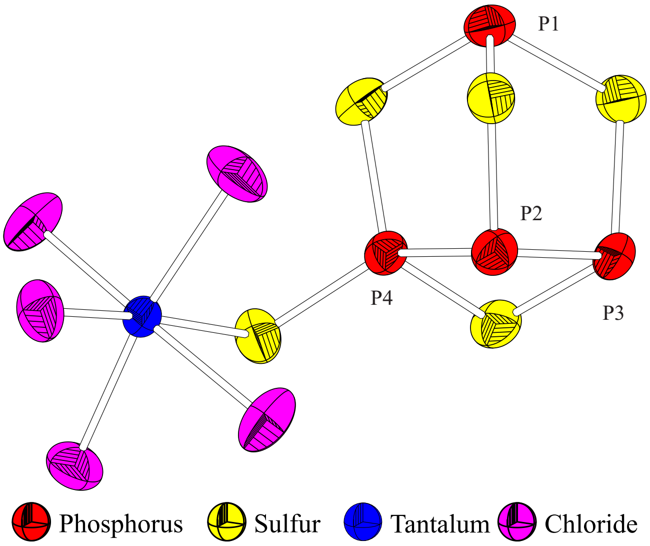

Figure 4-26
$(TaCl_5)(\alpha\text{-}P_4S_5)$ molecule as taken from the crystal structure of $(TaCl_5)(\alpha\text{-}P_4S_5)$. The ellipsoids represent 50 % of the spatial probability distribution of the electrons .

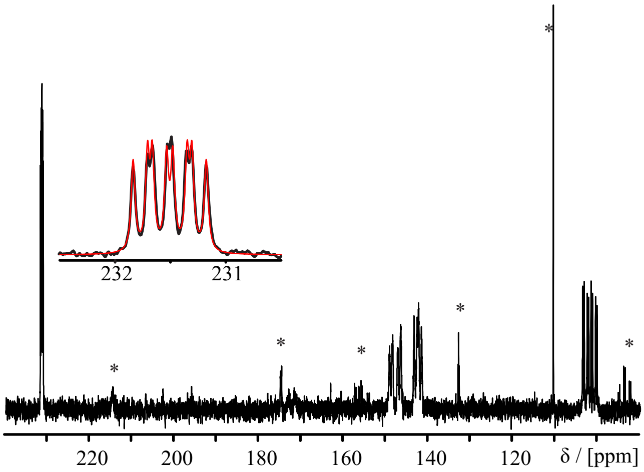

Figure 4-27
^{31}P liquid-state NMR spectrum of $(TaCl_5)(\alpha\text{-}P_4S_5)$ dissolved in carbon disulfide. Decomposition products are indicated with asterisks. The inset shows a blow-up and fit (red line) of the signal group of the apical phosphorus atom. The extracted NMR parameters are summarized in Table 4-7. The spectrum was recorded by the analytical section of the chemical department of the University of Regensburg.

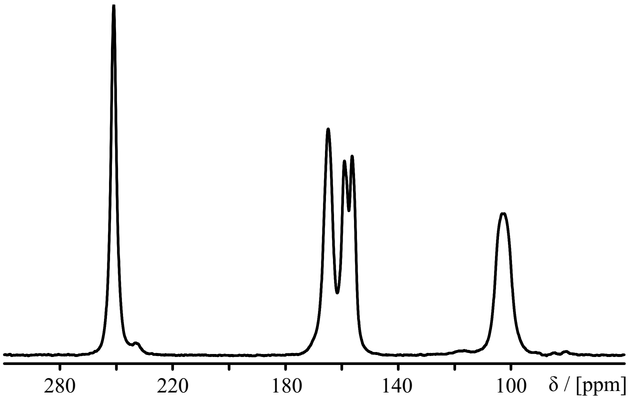

Figure 4-28
^{31}P MAS NMR spectrum of $(TaCl_5)(\alpha\text{-}P_4S_5)$ at a sample spinning rate of 25 kHz.

Table 4-7 gives the chemical shifts and J-couplings of the liquid-state and solid-state phase of $(TaCl_5)(\alpha\text{-}P_4S_5)$.

		δ [ppm]	J(P,P) [Hz]	%
liquid-state NMR				
	P1	231.5	$^2J(P1,P2) = 58$	24.0
			$^2J(P1,P3) = 28$	
			$^2J(P1,P4) = 21$	
	P2	102.0	$^2J(P2,P1) = 58$	26.9
			$^1J(P2,P3) = 313$	
			$^1J(P2,P4) = 174$	
	P3	148.0	$^2J(P3,P1) = 28$	23.0
			$^1J(P3,P2) = 313$	
			$^2J(P3,P4) = 114$	
	P4	142.6	$^2J(P4,P1) = 21$	26.1
			$^1J(P4,P2) = 174$	
			$^2J(P4,P3) = 114$	
solid-state NMR				
	P1	241.1	–	25.5
	P2	102.9	320	24.2
	P3	165.0	–	24.1
	P4	157.8	320	26.3

Table 4-7
^{31}P NMR parameters of $(TaCl_5)(\alpha\text{-}P_4S_5)$.

It is noticeable that there is a particulary large J-coupling $^1J(P2,P3) = 313$ Hz between P2 and P3 in the ^{31}P liquid-state NMR spectrum and $^1J(P2,P3) = 320$ Hz in the ^{31}P solid-state NMR MAS spectrum compared to a J-coupling of $^1J(P2,P4) = 174$ Hz between P2 and P4 in the ^{31}P liquid-state MAS NMR spectrum. For the solid-state structure the distances are 2.24 *Å* and 2.29 *Å* between P2 and P4 and P2 and P4, respectively. Therefore, the difference of both J-couplings can not be explained due to a different bond length or a different geometry. The discrepancy of the J couplings stem from the fact that P4 is additionally connected to a sulfur atom which decreases the charge density from the P2-P4 bond and therefore diminishes the J-coupling whereas P3 is not bound to a sulfur atom outside the phosphorus-sulfur cage. Owing to these considerations, an assignment of the middle downfield peak to the connecting basal phosphorus atom P4 and of the middle upfield signal to the not connecting basal phosphorus atom P3 is possible in the ^{31}P solid-state NMR MAS spectrum as well as in the ^{31}P liquid-state NMR spectrum.

Many phosphorus chalcogenide compounds are not sufficiently soluble or turned out to be unstable in the solvent solutions and the decomposition effects are observable in the ^{31}P liquid-state NMR spectrum as seen in Figure 4-27. In many cases homogeneous and inhomogeneous line broadening covers the J-coupling pattern in solid-state NMR spectroscopy and an assignment or structural information are not accessible a priori from the 1D spectrum. In order to gain deeper insight into the crystal structure, the connectivity inside the phosphorus sulfide cage could be exposed by ^{31}P–^{31}P 2D correlation experiments. The first approach to examine the configuration of the phosphorus sulfide cage is to perform a 2D ^{31}P homonuclear NOESY experiment. As discussed in Chapter 2.4.1, crosspeaks in the NOESY spectrum give information about spacial proximity of the examined nuclei. A prerequisite for the appearance of off-diagonal signals and the spin diffusion process is an overlap of the Zeeman levels. This is accomplished by line broadening processes like a strong dipolar coupling to adjacent protons (proton driven spin diffusion), chemical shift anisotropy or homonuclear dipolar couplings. Additionally there must exist a (residual) dipolar coupling between the involved nuclei. The inorganic phosphorus sulfide-tantalum chloride systems contain no protons and other anisotropic interactions are averaged to zero due to fast sample spinning rates. Hence, the success of this kind of experiment is not guaranteed in our case of high sample spinning rates. The NOESY spectra of $(TaCl_5)_2(\beta\text{-}P_4S_5)$ (Figure 4-29 and Figure 4-30 for long and short mixing times, respectively) exhibit no signals besides the diagonal peaks and give therefore no further information about the structure.

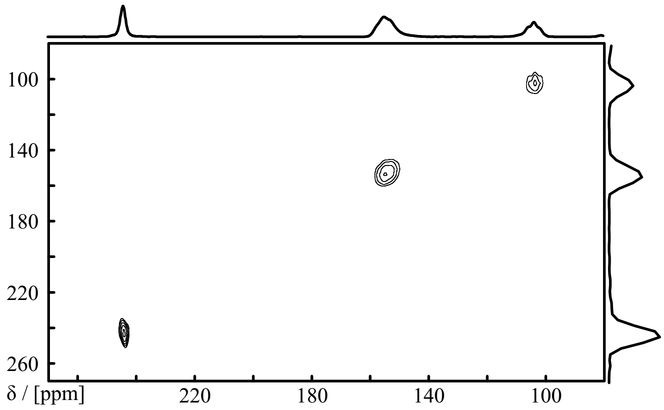

Figure 4-29
2D NOESY MAS NMR spectrum of $(TaCl_5)_2(\beta\text{-}P_4S_4)$ with a long mixing time of 3.2 ms and at a sample spinning rate of 25 kHz. The F_2 and F_1 projections are shown at the top and the right side of the 2D spectrum, respectively.

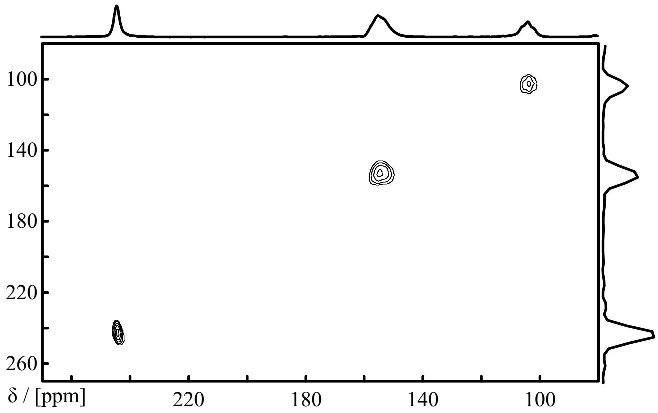

Figure 4-30
2D NOESY MAS NMR spectrum of $(TaCl_5)_2(\beta\text{-}P_4S_4)$ with a short time of 0.64 ms and at a sample spinning rate of 25 kHz. The F_2 and F_1 projections are shown at the top and the right side of the 2D spectrum, respectively.

^{31}P NOESY experiments on $(TaCl_5)(\alpha\text{-}P_4S_5)$ also reveal no new insight into the chemical structure of the phosphorus sulfide cages (see Figure 4-31 and Figure 4-32 for long and short mixing times, respectively).

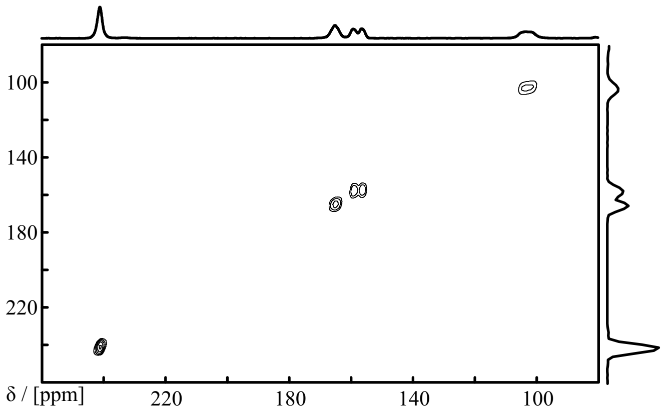

Figure 4-31
2D NOESY MAS NMR spectrum of $(TaCl_5)(\alpha\text{-}P_4S_5)$ with a long mixing time of 3.2 ms and at a sample spinning rate of 25 kHz. The F_2 and F_1 projections are shown at the top and the right side of the 2D spectrum, respectively.

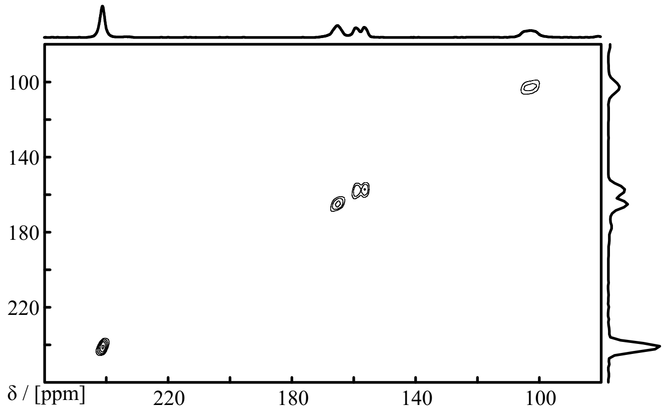

Figure 4-32
2D NOESY MAS NMR spectrum of $(TaCl_5)(\alpha\text{-}P_4S_5)$ with a short mixing time of 0.64 ms and at a sample spinning rate of 25 kHz. The F_2 and F_1 projections are shown at the top and the right side of the 2D spectrum, respectively.

The averaging effect of MAS can be overcome using special recoupling techniques during the mixing time of a 2D correlation experiments. This procedure allows spindiffusion processes while retaining the high resolution of MAS spectra. Figure 4-33 and Figure 4-34 show 2D NOESY-type MAS NMR spectra of $(TaCl_5)_2(\beta\text{-}P_4S_4)$ with RFDR recoupling during the longitudinal spindiffusion period for mixing times of 3.2 ms and 0.64 ms, respectively. The RFDR pulses destroy the averaging effect of MAS and reintroduce the dipolar coupling between the phosphorus nuclei during the mixing time (see Chapter 2.4.2). Both spectra exhibit crosspeaks which indicate spacial vicinity of the correlated nuclei. The distances can are evaluated by varying the mixing time of the 2D experiment as it is seen in the spectra of Figure 4-33 and Figure 4-34. For long mixing times (Figure 4-33) crosspeaks appear between all phosphorus sites in the phosphorus sulfide cage. On the other hand, reducing the mixing time to one fifth compared to the former experiment gives only crosspeaks between the signals of the basal phosphorus nuclei P2 and P3/P4 (Figure 4-34). This is consistent with the distance distribution in the phosphorus sulfide cage. The distance between the basal phosphorus atom P2–P3/P4 amounts to 2.25 Å while the distance between the apical phosphorus atom P1 and the basal phosphorus atoms P2, P3 and P4 is between 3.27 Å and 3.34 Å. Therefore, an assignment of the apical phosphorus atom P1 to the signal at $\delta = 244.0$ ppm is possible without further examination. Owing to the integrated area ratios (see Table 4-6), a definitive assignment of the remaining signals at $\delta = 104.5$ ppm to the middle basal phosphorus atom P2 and the resonance at $\delta = 168.2$ ppm to the two outer basal phosphorus atoms P2 / P3 was done solely on the basis of the solid-state MAS NMR spectra.

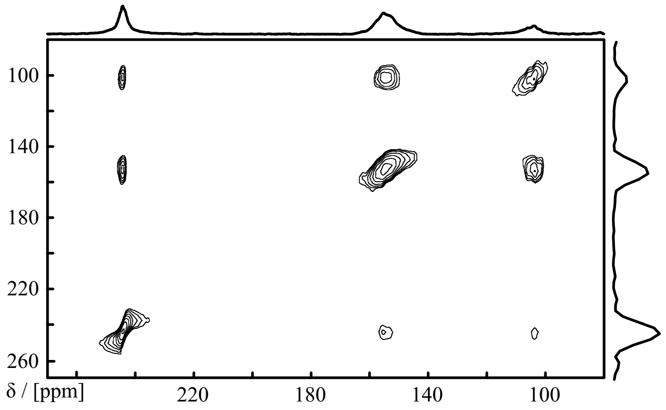

Figure 4-33
2D NOESY-type MAS NMR spectrum of $(TaCl_5)_2(\beta\text{-}P_4S_4)$ with RFDR recoupling during the longitudinal spindiffusion period (mixing time: 3.2 ms, sample spinning rate: 25 kHz). The F_2 and F_1 projections are shown at the top and the right side of the 2D spectrum, respectively.

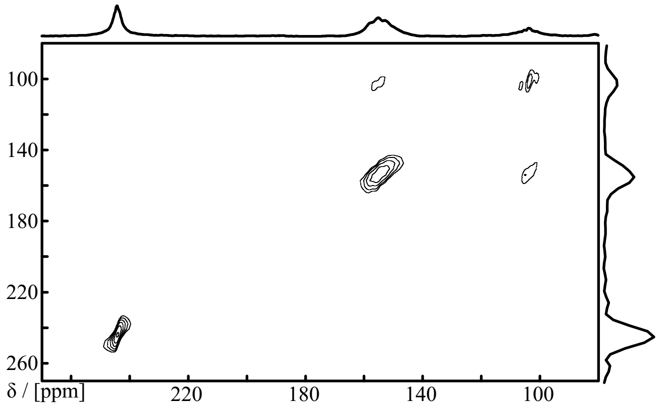

Figure 4-34
2D NOESY-type MAS NMR spectrum of $(TaCl_5)_2(\beta\text{-}P_4S_4)$ with RFDR recoupling during the longitudinal spindiffusion period (mixing time: 0.64 ms, sample spinning rate: 25 kHz). The F_2 and F_1 projections are shown at the top and the right side of the 2D spectrum, respectively.

The same recoupling scheme was also applied to the $(TaCl_5)(\alpha\text{-}P_4S_5)$ sample. The 2D NOESY-type ^{31}P-^{31}P MAS NMR spectra are shown in Figure 4-35 and 4-36. The RFDR-mixing times are 3.2 ms in case of the spectrum in Figure 4-35 and 0.64 ms for the other spectrum in Figure 4-36. In contrast to the two spectra shown above, the spectra of $(TaCl_5)(\alpha\text{-}P_4S_5)$ were recorded performing a more extended phase cycle and an additional presaturation sequence before each consecutive scan. The advantages are obvious in the spectra. The signals in the spectra of $(TaCl_5)_2(\beta\text{-}P_4S_4)$ are distorted and exhibit some antiphase contributions. Note that these contributions are not visible in the shown spectra (Figure 4-33 and 4-34) since only positive contour levels are displayed. On the other hand, these artefacts are not seen in the spectra of $(TaCl_5)(\alpha\text{-}P_4S_5)$ (Figure 4-35 and 4-36).

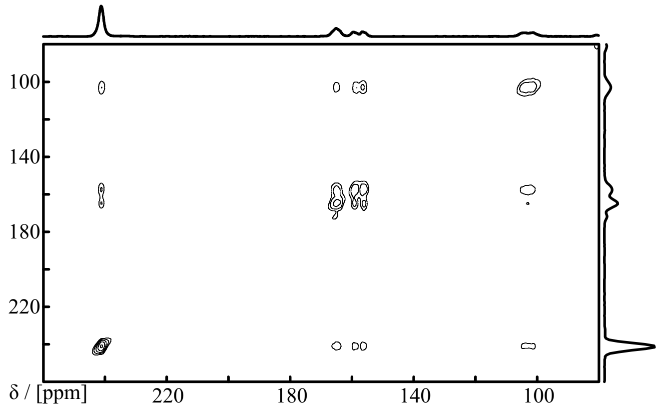

Figure 4-35
2D NOESY-type MAS NMR spectrum of $(TaCl_5)(\alpha\text{-}P_4S_5)$ with RFDR recoupling during the longitudinal spindiffusion period (mixing time: 3.2 ms, sample spinning rate: 25 kHz). The F_2 and F_1 projections are shown at the top and the right side of the 2D spectrum, respectively.

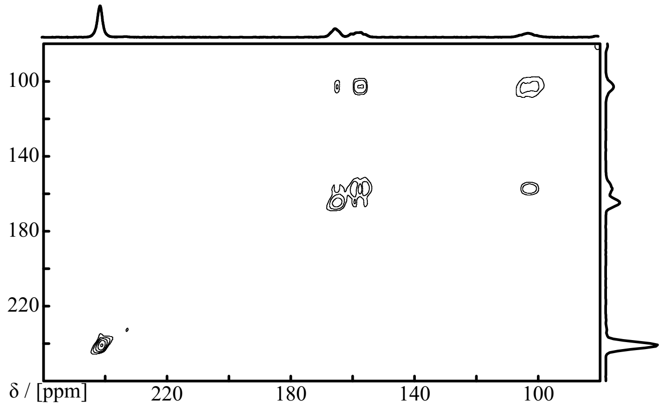

Figure 4-36
2D NOESY-type MAS NMR spectrum of $(TaCl_5)(\alpha\text{-}P_4S_5)$ with RFDR recoupling during the longitudinal spindiffusion period (mixing time: 0.64 ms, sample spinning rate: 25 kHz). The F_2 and F_1 projections are shown at the top and the right side of the 2D spectrum, respectively.

The NOESY experiment and the 2D NOESY-type RFDR experiment exploit the homonuclear dipolar ^{31}P–^{31}P coupling to allow a spin diffusion process. These kinds of experiments can provide valuable information about internuclear distances but do not allow an unambiguous discrimination between real bond connectivities and mere spacial proximities. For instance, proximities of phosphorus atoms of the same P_4S_4 cage and phosphorus atoms of different adjacent P_4S_4 cages yield the same signals in the dipolar driven spectrum if the distances are comparable. Therefore, a discrimination of intermolecular and intramolecular contacts is not possible solely due to NOESY-type experiments. Direct connectivities which are provided by chemical bonds can be detected and investigated by the application of special recoupling schemes which selectively exploit the indirect scalar coupling. Brunklaus [Chan, 2001] [Brunklaus, 2003b] [Reiser, 2002] has developed a new TOBSY-like (total through-bond correlation spectroscopy) experiment in which the polarization transfer is mediated only by the J-coupling (see Chapter 2.4.3). This new pulse sequence, R-TOBSY, was successfully applied to phosphorus based clusters and phosphorus chalcogenide cage compounds to explore direct bond connectivities [Brunklaus, 2003a] [Brunklaus, 2003b]. Figure 4-37 and Figure 4-38 show a ^{31}P homonuclear R-TOBSY SQ correlation experiment of $(TaCl_5)_2(\beta\text{-}P_4S_4)$ for a R-TOBSY mixing time of 4.8

ms and 0.96 ms, respectively. The basic requirement for R-TOBSY measurements is a non-zero scalar coupling constant. Theoretically, a maximum polarization transfer is expected at a mixing time $\tau_{mix} = (2J)^{-1}$. As two-bond J-couplings ^{2}J are generally much smaller than direct J couplings ^{1}J, a discrimination of the direct bound basal phosphorus atoms P2–P3/P4 and the bonding between basal and apical phosphorus atoms P1–P2/P3/P4 should be possible by varying the mixing time. The spectra Figure 4-37 and Figure 4-38 demonstrate this fact very well. While for long mixing times (Figure 4-37) crosspeaks are visible between all phosphorus resonances, for short mixing times (Figure 4-38) only crosspeaks between the basal phosphorus atoms appear in the spectrum.

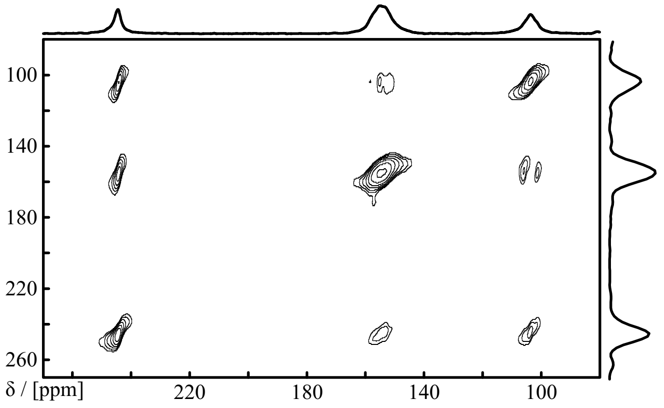

Figure 4-37
2D SQ-SQ correlation MAS NMR spectrum of $(TaCl_5)_2(\beta\text{-}P_4S_4)$ with R-TOBSY recoupling during the mixing period (mixing time: 4.8 ms, sample spinning rate: 25 kHz). The F_2 and F_1 projections are shown at the top and the right side of the 2D spectrum, respectively.

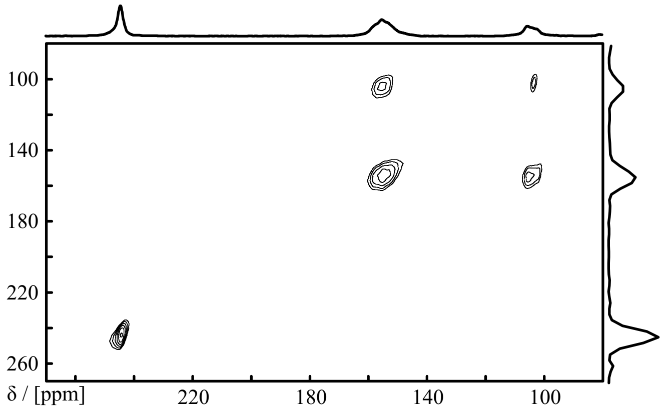

Figure 4-38
2D SQ-SQ correlation MAS NMR spectrum of $(TaCl_5)_2(\beta\text{-}P_4S_4)$ with R-TOBSY recoupling during the mixing period (mixing time: 0.96 ms, sample spinning rate: 25 kHz). The F_2 and F_1 projections are shown at the top and the right side of the 2D spectrum, respectively.

The same experiment was also applied to $(TaCl_5)(\alpha\text{-}P_4S_4)$. Figure 4-39 and Figure 4-40 show the resulting spectra for a mixing time of 4.8 ms and 0.96 ms, respectively.

NOESY-type and TOBSY-type SQ-SQ correlation experiments suffer from a number of limitations. They can only provide distance and connectivity information of nuclei with different chemical shifts and an interpretation of the spectra can be complicated, if the spin diffusion process is transferred by a third interaction partner [Iuga, 2007, and references therein]. A more selective approach which can overcome these limitations is the application of DQ techniques [Munowitz, 1986]. The basic concept of these kinds of experiments is explained in Chapter 2.5. The difference between the SQ and DQ approach is that in a DQ experiment only resonances of interacting nuclei are selected and any signal coming from isolated nuclei is filtered. A correlation between the nuclei can be established by a dipolar coupling or a J-coupling.

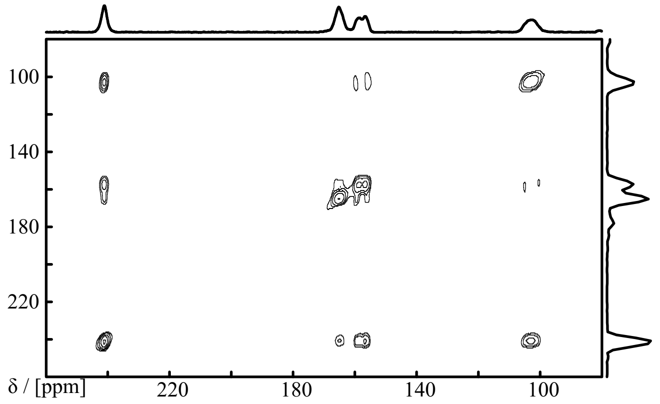

Figure 4-39
2D SQ-SQ correlation MAS NMR spectrum of $(TaCl_5)(\alpha\text{-}P_4S_5)$ with R-TOBSY recoupling during the longitudinal spindiffusion period (mixing time: 4.8 ms, sample spinning rate: 25 kHz). The F_2 and F_1 projections are shown at the top and the right side of the 2D spectrum, respectively.

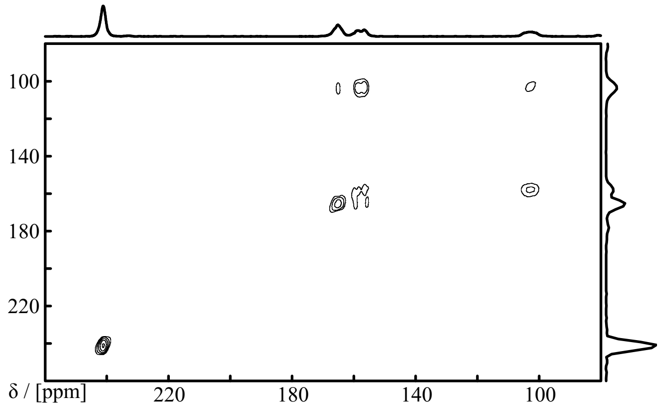

Figure 4-40
2D SQ-SQ correlation MAS NMR spectrum of $(TaCl_5)(\alpha\text{-}P_4S_5)$ with R-TOBSY recoupling during the longitudinal spindiffusion period (mixing time: 0.96 ms, sample spinning rate: 25 kHz). The F_2 and F_1 projections are shown at the top and the right side of the 2D spectrum, respectively.

.

Figure 4-41 shows a SQ-DQ refocused INADEQUATE [Lesage, 1999] [Sakellariou, 2002] spectrum of $(TaCl_5)_2(\beta\text{-}P_4S_4)$, in which the J-coupling is used for DQ excitation (see Chapter 2.5.1).

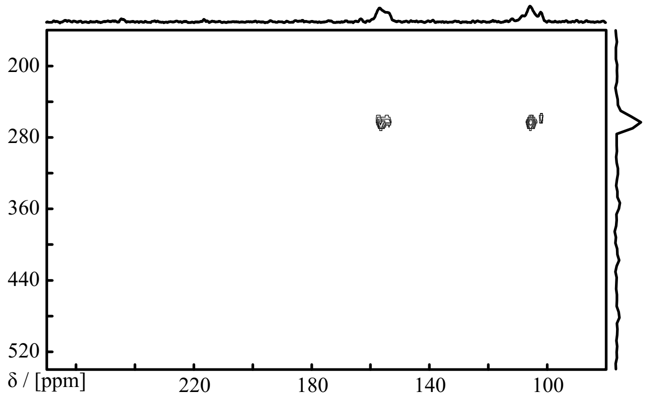

Figure 4-41
2D SQ-SQ refocused INADEQUATE MAS NMR spectrum of $(TaCl_5)_2(\beta\text{-}P_4S_4)$ with a DQ evolution time of 0.8 ms and at a sample spinning rate of 25 kHz. The F_2 and F_1 projections are shown at the top and the right side of the 2D spectrum, respectively.

Owing to high sample spinning rates, heteronuclear decoupling and the used phase cycle, only ^{31}P-^{31}P J-coupled nuclei give rise to a signal. The different chemical sites can be identified easily from their isotopic chemical shift in the SQ dimension. Information about connectivities is found in the DQ dimension in which the signals occur at the sum of the isotopic chemical shifts of the involved phosphorus sites. In spectrum Figure 4-41 only the signals of coupled spins P2-P3 are visible. In analogy to the TOBSY experiments, the performance of an INADEQUATE experiment depends on the size of the J-coupling. Only signals due to the comparatively large ^1J coupling between P2 and P3/P4 are visible in the spectrum while signals due to the smaller ^2J couplings between the basal and apical phosphorus atoms are not excited. Theoretically, signals originating from these weak J-couplings could also be excited by extending the DQ excitation period. However, after a 90 degree pulse the DQ excitation takes place in the x/y plane of the rotating frame which means that the transverse relaxation time T_2 is the limiting factor. In case of the refocused INADEQUATE experiment, the efficiency depends on the ratio T_2'/T_2^*, where T_2' is the transverse dephasing time measured in a spin echo experiment and T_2^* is the apparent relaxation time deduced from the linewidth [Lesage, 1999].

In analogy to the J-coupling driven INADEQUATE experiment, the dipolar coupling can also be used to excite multi-quantum transitions. Under high sample spinning rate conditions the dipolar coupling has to be reintroduced as it was already mentioned in the introduction. It turned out that a particulary useful and promising recoupling technique is the method of R- and C-symmetry based pulse sequences developed in the Levitt group [Carravetta, 2000] [Brinkmann, 2001] [Levitt, 2002]. One member of these kinds of pulse sequences is the afore mentioned R-TOBSY pules scheme, which eliminates all interactions allowing only the isotropic J-coupling to persist. In the same way dipolar couplings can be reintroduced under fast MAS using the principles of R- and C- symmetries. In the following experiment the POST-C7 pulse sequence was used (see Chapter 2.5.2) [Lee, 1995] [Hohwy, 1998].

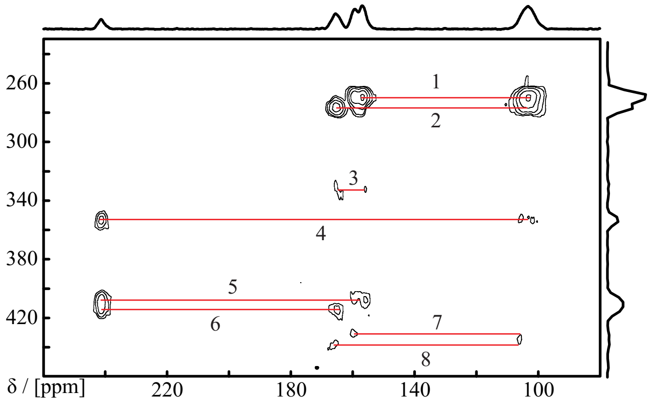

Figure 4-42
2D SQ-DQ correlation MAS NMR spectrum of $(TaCl_5)(\alpha\text{-}P_4S_5)$ with POST-C7 recoupling during the double-quantun excitation and reconversion period. Sample spinning rate: 20 kHz. The F_2 and F_1 projections are shown at the top and the right side of the 2D spectrum, respectively.

The advantage of the dipolar driven excitation method is that the dipolar coupling is normally one order of magnitude larger than the J-coupling and, therefore, more coupling signals are expected in the dipolar driven experiment. Analysis and interpretation of the resulting spectrum accord with the INADEQUATE experiment. While chemical shift information and therefore the assignment is obtained in the SQ dimension of the spectrum, dipolar coupling information is found in the DQ dimension. The SQ-DQ spectrum of $(TaCl_5)\alpha\text{-}(P_4S_5)$ is shown in Figure 4-42. Red lines in Figure 4-42 mark the connectivity of two dipolar coupled spins. All phosphorus-phosphorus contacts of the phosphorus-sulfur cage can be identified in the spectrum and the assignment can be done due to the chemical shifts found in the SQ dimension.

1	P4–P2
2	P3–P2
3	P3–P4
4	P1–P2
5	P1–P4
6	P1–P3
7	spinning sideband of 1
8	spinning sideband of 2

Table 4-8
Assignment of the SQ-DQ correlation MAS NMR spectrum of $(TaCl_5)(\alpha\text{-}P_4S_5)$ shown in Figure 4-42.

4.9 Discussion of ^{31}P–^{63,65}Cu Coupling Constants

The indirect scalar coupling (or J-coupling) is a rich source of local structural information. Through bond connectivities and corresponding J-coupling values have proven to be very sensitive to internuclear distances [Karplus, 1963], bond angles [Karplus, 1963] [Contreras, 2000a] and the nature of the chemical bond [Contreras, 2000b]. They are routinely used for structure determination of proteins and peptides [Wüthrich, 1976] in liquid-state NMR. In solids, other dominant interactions often cover and truncate the present J-couplings. As a result, J-couplings are usually not resolved in 1D spectra of solids and 2D methods have to be applied to analyze J-couplings [Sakellariou, 2002].

One exception are the heteronuclear J-couplings between phosphorus and copper in inorganic solids. The J-coupling values range from 500 Hz to 2000 Hz in these compounds [Brunklaus, 2003b] and can therefore be identified in many cases in the 1D ^{31}P MAS NMR spectra. ^{63}Cu and ^{65}Cu are quadrupolar nuclei with spin 3/2. Large quadrupolar coupling constants are known to cause large linebroadening and linesplitting in the spectra of dipolar- or J-coupled spin 1/2 nuclei [Alarcón, 1993]. In particular, the spacings of the J-coupling quartets $\Delta\nu_i$ could be irregular requiring a detailed lineshape simulation for the analysis of such spectra (see Figure 4-43) [Gobetto, 1992] [Olivieri, 1992] [Asaro, 1997].

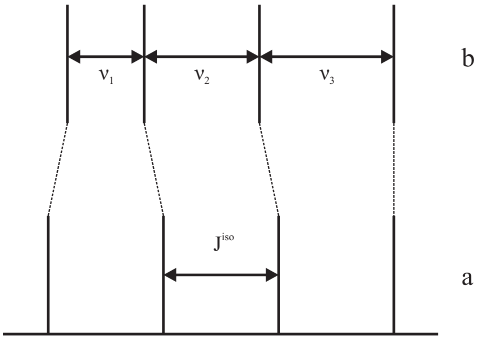

Figure 4-43
Line splitting of a ^{31}P NMR signal araising from a coupling to a copper nucleus. a) regular splitting, b) irregular splitting.

The compounds analyzed in this work exhibit none of these perturbations in the spectrum suggesting that the quadrupole coupling is small compared to the nuclear Zeeman interaction of copper [Asaro, 1997, and refernces therein]. A vanishing quadrupole coupling constant represents a spherically symmetric charge distribution around the copper nucleus as it is expected for the copper centers examined in this work, at least for the copper atoms bound to the apical phosphorus atoms. For the following discussion, only J-coupling values of the apical phosphorus atoms are taken into account. For these values, a tetrahedrally symmetric environment of the copper atom is given and a regular J-pattern is clearly observable in the spectrum. In the literature, also irregular spacings $\Delta\nu$ of the J-coupling quartets are reported. In such cases $<\Delta\nu>=(1/3)(\Delta\nu_1+\Delta\nu_2+\Delta\nu_3)$ has been used for the approximination of J^{iso} [Gobetto, 1992] (see Chapter 2.2.2). Table 4-9 gives an overview over some $^1J^{iso}(^{31}P,^{63,65}Cu)$ coupling values collected in the literature and in this work. Only phosphorus-copper-halogen compounds with four coordinated copper atoms are taken into account.

copper coordination	J(P,Cu) [Hz]	reference
P_1CuBr_3	1405	[this work]
P_2CuCl_2	1055	[this work]
P_1CuCl_3	1600	[this work]
P_1CuI_3	1067	[this work]
P_2CuI_2	882	[Brunklaus, 2003a]
P_1CuI_3	1232	[Brunklaus, 2003a]
P_1CuI_3	1221	[Brunklaus, 2003a]
P_3CuCl	927, 900	[Barron, 1987]
P_3CuBr	933, 923	[Barron, 1987]
P_3CuI	920, 916	[Barron, 1987]
P_3CuCl	940	[Diesveld, 1980]

Table 4-9
Table of $^1J^{iso}(^{31}P,^{63,65}Cu)$-coupling values.

These compounds are different with respect to the type and number of halogen atoms (X = Cl, Br, I) bound to the copper atom and the number and bond length of the bound phosphorus atoms (P): P_nCuX_{4-n} , $1 < n < 4$; the results are depicted in Figure 4-44. The magnitudes of the corresponding scalar coupling constants $^1J(^{31}P,^{63,65}Cu)$ show a strong correlation with the number of neighboring phosphorus atoms with a general tendency of $^1J(^{31}P,^{63,65}Cu)$ to decrease with increasing phosphorus atom coordination. The influence of the halogen ligand bound to the copper atom is also nicely illustrated in Figure 4-44.

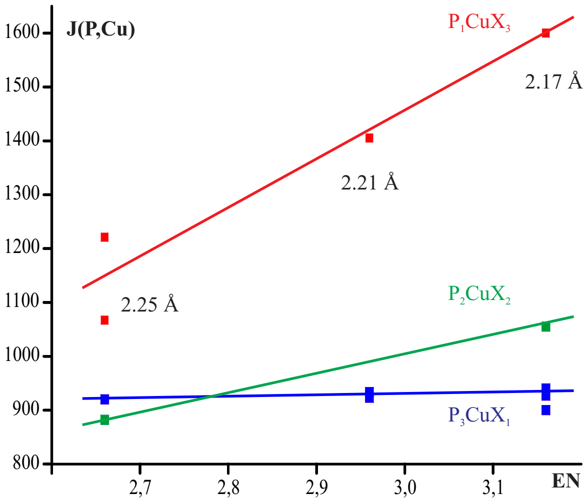

Figure 4-44
Dependency of the J(P,Cu)-coupling values on the copper coordinated halides and number of phosphorus atoms. The numbers given for the P_1CuX_3 curve (red) in the graph specify the copper-phosphorus bond length taken from crystallographic data.

For a given number of phosphorus ligands, the scalar coupling constants $^1J(^{31}P,^{63,65}Cu)$ increase with increasing electronegativity (EN) of the halogen atom (EN(Cl) = 3.16, EN(Br) = 2.96, EN(I) = 2.66), particulary in the case of P_1CuX_3. In the same way $^1J(^{31}P,^{63,65}Cu)$ increase with decreasing copper-phosphorus bond length which is also correlated to the halogen ligand X.

5 Summary

5.1 NMR Spectroscopic Studies on Diatoms

The characterization of the siliceous cell walls of diatoms as well as the study of the silica metabolism of diatoms greatly benefits from extended previous ^{29}Si studies of silica based materials. ^{29}Si chemical shifts as well as other results of previous NMR spectroscopic studies concerning the biological silica biomineralilazion process are summarized in Chapter 3.4 and 3.5. Isolated cell walls of diatoms were examined with solid-state NMR spectroscopic techniques in order to characterize the composition of the cell walls, especially with respect to the presence of organic components enclosed in the inorganic silica matrix. 1D ^{29}Si NMR MAS spectra of isolated ^{29}Si isotopic enriched cell walls of different diatoms species show no significant differences compared to ordinary commercially available silica. ^{29}Si{^{1}H} CP MAS NMR spectroscopic studies of commercially available silica and of ^{29}Si isotope labeled isolated cell walls allowed to compare these materials with respect to their cross polarization behavior. The determined time constants T_{CP} and $T_{1\rho}^{\mathrm{H}}$ describing the cross polarization process show a significant difference between the biological samples and the synthetic silica. The cross polarization process time constant as well as the ^{1}H relaxation rate is much faster for the cell wall samples suggesting the presence of organic moieties in the bulk silica of the cell walls. 2D ^{29}Si{^{1}H} HETCOR studies revealed that the spectra strongly depend on the hydration state of the samples which could be explained by the presence of cavities in the bulk silica material which are water accessible. The organic material could also directly be detected by 1D ^{13}C and 2D ^{13}C{^{1}H} HETCOR experiments. Most of the previous solid-state NMR spectroscopic studies of integer diatom cells and cell walls documented in the literature are performed on freeze dried samples. However, test experiments on silica solutions and freeze dried samples reveal a pronounced influence of the freeze drying process upon the silica species and their chemical state.

The silica metabolism of diatoms was examined by ^{29}Si solid-state NMR spectroscopy in combination with confocal laser fluorescence microscopy. These experiments were performed on integer diatoms using a new methodology based on much gentler methods than in previously reported experiments. Fluorescence microscopy allowed the assignment of the measured spectra to distinct developmental stages of the dividing cells. It was shown that the diatom species *Tha-*

lassiosira pseudonana does not store silica in the form of well-defined and stable organo-silicon complexes. Instead, the observed ^{29}Si MAS NMR spectroscopic investigations are consistent with the presence of pre-condensed silica species.

5.2 NMR Spectroscopic Studies of Phosphorus Chalcogenide - Copper Halide Systems

The aim of this solid-state ^{31}P NMR spectroscopic study was the determination of the structure of copper halide-P_4S_3/Se_3 compounds. Single crystal X-ray analysis of such compounds can be ambiguous if the studied systems contain nuclei of similar weight as in case of sulfur and phosphorus. An accurate determination of the structure became possible by the use of solid-sate ^{31}P NMR spectroscopy. In particular, the J(^{31}P,^{63,65}Cu) coupling pattern in the spectrum gives an unambiguous evidence of the phosphorus–copper binding in the examined compounds. The solid-state structures demonstrate an unexpected ligand versatility of the P_4S_3 molecule. This molecule interacts through two ($(P_4S_3)(CuI)$), through three ($(P_4S_3)(CuI)_3$, $(P_4S_3)_2(CuCl)_3$), or, for the first time, through all of the phosphorus atoms ($(P_4S_3)_3(CuCl)_7$) with copper. Sulfur does not play a role in the coordination to copper atoms. Furthermore, the application of 2D solid-state NMR experiments to phosphorus-sulfur cage systems was established. Since high sample spinning rates have to be applied in order get a sufficient resolution in the spectrum, complex recoupling techniques has to be performed. In this work RFDR, POST-C7, R-TOBSY, INADEQUATE experiments were employed. It was shown that these techniques provide valuable information about direct coupling and spatial proximities of the phosphorus atoms in the phosphorus-sulfur cage. However, more information about the examined compounds are provided by the single-quantum double-quantum experiment (POST-C7) which is driven by the dipolar coupling rather than by its J-coupling mediated analogon (refocused INADEQUATE). Furthermore, a correlation between the J(^{31}P,^{63,65}Cu) coupling constant and the electronegativity of the present halides could be found. For a given number of phosphorus ligands, the scalar coupling constants ^{1}J(^{31}P,^{63,65}Cu) increase with the increasing electronegativity of the halogen atom.

6 Publications

- Gröger, C., Lutz, K. and Brunner, E. (**2008**), NMR Studies of Biomineralisation, *Prog. Nuc. Mag. Res.*, **in press**.
- Gröger, C., Lutz, K. and Brunner, E. (**2008**), Biomolecular Self-assembly and its Relevance in Silica Biomineralization, *Cell Biochem. Biophys.* **50**, 23-39.
- Gröger, C., Sumper, M. and Brunner, E. (**2008**), Silicon uptake and metabolism of the marine diatom Thalassiosira pseudonana: Solid-state ^{29}Si NMR and fluorescence microscopic studies, *J. Struct. Biol.* **161**, 55-63.
- Iuga, D., Ader, C., Gröger, C. and Brunner, E. (**2007**), Applications of Solid-State ^{31}P NMR Spectroscopy, *Annual Reports on NMR Spectroscopy* **60**,145-189.
- Biegerl, A., Brunner, E., Gröger, C., Scheer, M., Wachter, J. and Zabel, M. (**2007**), The unexpected versatility of P_4S_3 as a building block in polymeric copper halide networks: 2,3-P, 1,2,3-P and all-P coordination, *Chemistry* **13**, 9270-9276.
- Gregoriades, L.J., Balázs, G., Brunner, E., Gröger, C., Wachter, J., Zabel, M. and Scheer, M. (**2007**), An unusual building block for supramolecular aggregates: the mixed group 15/16 element ligand complex $[(Cp^*Mo)_2(\mu,\eta^3\text{-}P_3)(\mu,\eta^2\text{-}PS)]$, *Angew. Chem. Int. Ed. Engl.* **46**, 5966-5970.
- Lutz, K., Gröger, C., Sumper, M. and Brunner, E. (**2005**), Biomimetic silica formation: analysis of the phosphate-induced self-assembly of polyamines, *Phys. Chem. Chem. Phys.* **7**, 2812-2815.
- Gröger, C, Möglich, A, Pons, M, Koch, B, Hengstenberg, W, Kalbitzer, HR, Brunner, E (**2003**), NMR-spectroscopic mapping of an engineered cavity in the I14A mutant of HPr from Staphylococcus carnosus using xenon, *J. Am. Chem. Soc.* **125**, 8726-8727.

7 Bibliography

L. Addadi, S. Weiner (1992). Control and Design Principles in Biological Mineralization. *Angewandte Chemie International Edition in English* 31, 153–169.

S. Alarcón, A. Olivieri, R. Harris (1993). Quadrupole effects of spin-3/2 nuclei on the solid-state magic-angle spinning nuclear magnetic resonance spectra of spin-1/2 nuclei. Deviations from first-order theory and implications concerning the sign of the indirect coupling constant. *Solid State Nuclear Magnetic Resonance* 2, 325–334.

E. Andrew, A. Bradbury, R. Eades (1958a). Nuclear Magnetic Resonance Spectra from a Crystal rotated at High Speed. *Nature* 182, 1659.

E. Andrew, A. Bradbury, R. Eades (1958b). Removal of Dipolar Broadening of Nuclear Magnetic Resonance Spectra of Solids by Specimen Rotation. *Nature* 183, 1802–1803.

E. R. Andrew, W. S. Hinshaw, A. Jasinski (1998). An AB_3 high-resolution spectrum in the solid state: ^{31}P in P_4S_3. *Chemical Physics Letters* 24, 399–400.

E. Armbrust, J. Berges, C. Bowler, B. Green, D. Martinez, N. Putnam, S. Zhou, A. Allen, K. Apt, M. Bechner, M. Brzezinski, B. Chaal, A. Chiovitti, A. Davis, M. Demarest, J. Detter, T. Glavina, D. Goodstein, M. Hadi, U. Hellsten, M. Hildebrand, B. Jenkins, J. Jurka, V. Kapitonov, N. Kröger, W. Lau, T. Lane, F. Larimer, J. Lippmeier, S. Lucas, M. Medina, A. Montsant, M. Obornik, M. Parker, B. Palenik, G. Pazour, P. Richardson, T. Rynearson, M. Saito, D. Schwartz, K. Thamatrakoln, K. Valentin, A. Vardi, F. Wilkerson, D. Rokhsar (2004). The genome of the diatom Thalassiosira pseudonana: ecology, evolution, and metabolism. *Science* 306, 79–86.

F. Asaro, A. Camus, R. Gobetto, A. Olivieri, G. Pellizer (1997). 63Cu-31P coupling constants and 63Cu quadrupole couplings from 31P CP/MAS spectra of copper (I)–phosphine complexes with aryldithiocarboxylates or benzoate. *Solid State Nuclear Magnetic Resonance* 8, 81–88.

F. Azam, B. Hemmingsen, B. Volcani (1974). Role of silicon in diatom metabolism. *Archives of Microbiology* 97, 103–114.

E. Baeuerlein, P. Behrens, M. Epple (2007). *Handbook of Biomineralization, Vol. 1-3*. Wiley-VCH, Weinheim.

M. Baldus, B. Meier (1996). Total Correlation Spectroscopy in the Solid State. The Use of Scalar Couplings to Determine the Through-Bond Connectivity. *Journal of Magnetic Resonance A* 3, 65–69.

M. Baldus, R. Iuliucci, B. Meier (1997). Probing Through-Bond Connectivities and Through-Space Distances in Solids by Magic-Angle-Spinning Nuclear Magnetic Resonance. *Journal of the American Chemical Society* 119, 1121–1124.

P. Barron, D. J.C., P. Healy, E. L.M., C. Pakawatchai, V. Patrick, W. A.H. (1987). Lewis-base adducts of Group 11 metal(I) compounds. Part 28. Solid-state phosphorus-31 cross-polarization magic-angle spinning nuclear magnetic resonance and structural studies on the mononuclear 3: 1 adducts of triphenylphosphine with copper(I) halides. *Journal of the Chemical Society, Dalton Transactions* 1987, 1099–1987.

A. Bax, R. Freemann, S. Kampsell (1980). Natural Abundance 13C-13C Coupling Observed via Double-Quantum Coherence. *Journal of the American Chemical Society* 102, 4849–4851.

A. Bax, R. Freemann, A. Frenkiel (1981). An NMR Technique for Tracing Out the Carbon Skeleton of an Organic Molecule. *Journal of the American Chemical Society* 103, 2102–2104.

A. Bennett, C. Rienstra, M. Auger, K. Lakshmi, G. R.G. (1995). Heteronuclear decoupling in rotating solids. *Journal of Chemical Physics* 103, 6951–6958.

A. Bennett, C. Rienstra, J. Griffiths, W. Zhen, P. Lansbury, R. Griffin (1998). Homonuclear radio frequency-driven recoupling in rotating solids. *Journal of Chemical Physics* 108, 9463–9479.

A. E. Bennett, J. H. Ok, R. G. Griffin, S. Vega (1992). Chemical shift correlation spectroscopy in rotating solids: Radio frequency-driven dipolar recooupling and longitudinal exchange. *Journal of Chemical Physics* 96, 8624–8627.

R. Bertermann, R. Tacke (2000). Solid-State 29Si VACP/MAS NMR Studies of Silicon-Accumulating Plants: Structural Characterization of Biosilica Deposits. *Zeitschrift für Naturforschung B* 55b, 459–462.

R. Bertermann, N. Kröger, R. Tacke (2003). Solid-state 29Si MAS NMR studies of diatoms: structural characterization of biosilica deposits. *Analytical and Bioanalytical Chemistry* 375, 630–634.

A. Biegerl (2007b). P(4)S(3) als Ligand in Kupfer(I)-Halogenid-Koordinationspolymeren. *Diploma thesis* .

A. Biegerl (2007c). Personal information .

A. Biegerl, E. Brunner, C. Gröger, M. Scheer, J. Wachter, M. Zabel (2007a). The Unexpected Versatility of P(4)S(3) as a Building Block in Polymeric Copper Halide Networks: 2,3-P, 1,2,3-P and all-P Coordination. *Chemistry* 13, 9270–9276.

A. Bielecki, A. Kolbert, M. Levitt (1989). Frequency-Switched Pulse Sequences: Homonuclear Decoupling and Dilute Spin NMR in Solids. *Chemical Physics Letters* 155, 341–346.

A. Bielecki, A. Kolbert, H. de Groot, R. Griffin, M. Levitt (1990). Frequency-Switched Lee-Goldburg Sequences in Solids. *Advances in Magnetic Resonance* 14, 111–124.

R. Blachnik, U. Wickel, P. Schmitt (1984). ^{31}P-NMR-spektroskopische Untersuchungen an A_4B_3-Molekülen. *Zeitschrift für Naturforschung B* 39b, 1135–1138.

G. Bodenhausen, H. Kogler, R. Ernst (1984). Selection of Coherence-Transfer Pathways in NMR Pulse Experiments. *Journal of Magnetic Resonance* 58, 370–388.

D. Bougeard, Z. Gamba (1998). The ordered, orientationally disordered and glassy phases of ^{31}P. *Molecular Physics* 49, 815–820.

G. Brauer (1975). *Handbuch der präparativen anorganischen Chemie*. Enke Verlag, Stuttgart.

A. Brinkmann, M. Levitt (2001). Symmetry principles in the nuclear magnetic resonance of spinning solids: Heteronuclear recoupling by generalized Hartman-Hahn sequences. *Journal of Chemical Physics* 115, 357–384.

Bruker (2005). *Bruker Almanac 2005*. Bruker.

F. Brunet, B. Cabane, M. Dubois, B. Perly (1991). Sol-gel polymerization studied through silicon-29 NMR with polarization transfer. *The Journal of Physical Chemistry* 95, 945–951.

G. Brunklaus (2003b). Solid State NMR Conectivity Studies in Phsophorus - Based Inorganic Clusters and Networks. *Doctoral thesis* .

G. Brunklaus, J. C. C. Chan, H. Eckert, S. Reiser, T. Nilges, A. Pfitzner (2003a). NMR studies of phosphorus chalcogenide-copper iodide coordination compounds. *Physical Chemistry, Chemical Physics* 5, 2768–2776.

E. Brunner, K. Lutz (2007). Solid-State NMR in Biomimetic Silica Formation and Silica Biomineralization. *Handbook of Biomineralization* p. 19.

E. Brunner, D. Freude, B. Gerstein, H. Pfeiffer (1990a). Residual Linewidths of NMR Spectra of Spin-1/2 Systems under Magic-Angle Spinning. *Journal of Magnetic Resonance* 90, 90–99.

E. Brunner, D. Frenzke, D. Freude, H. Pfeiffer (1990b). The Influence of Homonuclear Dipolar Interaction on the Residual Linewidth of MAS NMR Spectra. *Chemical Physics Letters* 169, 591–594.

M. Brzezinski, D. Conley (1994). SILICON DEPOSITION DURING THE CELL CYCLE OF THALASSIOSIRA WEISSFLOGII (BACILLARIOPHYCEAE) DETERMINED USING DUAL RHODAMINE 123 AND PROPIDIUM IODIDE STAINING. *Journal of Phycology* 30, 45–55.

M. Brzezinski, R. Olsen, S. Chisholm (1990). Silicon availability and cell-cycle progression in marine diatoms. *Marine Ecology Progress Series* 67, 83–96.

J. Buddrus, H. Bauer (1987). Direct Identification of the Carbon Skeleton of Organic Compunds using Double Coherence 13C-NMR Spectroscopy. The INADEQUATE Pulse Sequence. *Angewandte Chemie International Edition* 26, 625–642.

S. Cadars, J. Sein, L. Duma, A. Lesage, T. Phan, J. Baltisberger, S. Brown, L. Emsley (2007). The refocused INADEQUATE MAS NMR experiment in multiple spin-systems: Interpreting observed correlation peaks and optimising lineshapes. *Journal of Magnetic Resonance* 188, 24–34.

M. Carravetta, M. Eden, X. Zhao, A. Brinkmann, M. Levitt (2000). Symmetry principles for the design of radiofrequency pulse sequences in the nuclear magnetic resonance of rotating solids. *Chemical Physics Letters* 321, 205–215.

W. Casey, S. Kinrade, C. Knight, D. Rains, E. Epstein (2004). Aqueous silicate complexes in wheat, Triticum aestivum L. . *Plant, Cell & Environment* 27, 51–54.

T. Casserly, K. Gleason (2005). Density Functional Theory Calculation of 29Si NMR Chemical Shifts of Organosiloxanes. *Journal of the Physical Chemistry B* 13605–13610.

J. Cavanagh, W. Faibrother, A. Palmer III, N. Skelton (1996). *Protein NMR Spectroscopy - Principles and Practice*. Academic Press, San Diego.

J. Chan, G. Brunklaus (2001). R sequences for the scalar-coupling mediated homonuclear correlation spectroscopy under fast magic-angle spinning. *Chemical Physics Letters* 349, 104–112.

S. Chisholm, F. Azam, R. Eppley (1978). Silicic acid incorporation in marine diatoms ma light:dark cycles: Use as an assay for phased cell division. *Limnology and Oceanography* 23, 518–529.

S. Christiansen, N. Hedin, J. Epping, M. Janicke, Y. del Amo, M. Demarest, M. Brzezinski, B. Chmelka (2006). Sensitivity considerations in polarization transfer and filtering using dipole-dipole couplings: implications for biomineral systems. *Solid State Nuclear Magnetic Resonance* 29, 170–182.

R. Contreras, J. Peralta (2000a). Angular dependence of spin-pin coupling constants. *Progress in Nuclear Magnetic Resonance Spectroscopy* 37, 321–425.

R. Contreras, J. Peralta, C. Giribert, M. Ruiz de Azua, J. Facelli (2000b). Advances in Theoretical and Physical Aspects of Spin–Spin Coupling Constants. *Annual Reports on NMR Spectroscopy* 41, 55–184.

S. Crawford, M. Higgins, P. Mulvaney, R. Wetherbee (2001). NANOSTRUCTURE OF THE DIATOM FRUSTULE AS REVEALED BY ATOMIC FORCE AND SCANNING ELECTRON MICROSCOPY. *Journal of Phycology* 543–554.

W. Darley, B. Volcani (1971). Synchronized cultures: Diatoms. *Methods in Enzymology* 23, 85–96.

J. Descles, M. Vartanian, A. El Harrak, M. Quinet, N. Bremond, G. Sapriel, J. Bibette, P. Lopez (2008). New tools for labeling silica in living diatoms. *New Phytologist* 177, 822–829.

A. Detken, E. Hardy, M. Ernst, B. Meier (2002). Simple and efficient decoupling in magic-angle spinning solid-state NMR: the XiX scheme. *Chemical Physics Letters* 356, 298–304.

J. Diesveld, E. Menger, H. Edzes, V. W.S. (1980). High-Resolution Solid-State Phosphorus-31 Nuclear Magnetic Resonance of some Triphenylphosphine Transition-Metal Complexes. *Journal of the American Chemical Society* 102, 7935–1936.

R. Drum, H. Pankratz (1964). Post mitotic fine structure of Gomphonema parvulum. *Journal of Ultrastructure Research* 10, 217–223.

H. Eckert (1992). Structural Characterization of Noncrystalline Solids and Glasses using Solid State NMR. *Progress in Nuclear Magnetic Resonance Spectroscopy* 24, 159–293.

H. Eckert, C. S. Liang, Stucky, G. D. (1989). ^{31}P Magic Angle Spinning NMR of Crystalline Phosphorus Sulfides. Correlation of ^{31}P chemical Shielding Tensors with Local Environments. *Journal of Physical Chemistry* 93, 452–457.

H. Eckert, S. Elbers, J. Epping, M. Janssen, M. Kalwei, W. Strojek, U. Voigt (2004). Dipolar Solid State NMR Approaches Towards Medium-Range Structure in Oxide Glasses. *Topics in Current Chemistry* 246, 195–233.

G. Engelhardt (1996). Silicon-29 NMR of Solid silicates. *Encyclopedia of Nuclear Magnetic Resonance* 7, 4398–4407.

G. Engelhardt, D. Michel (1987). *High-Resolution Solid-State NMR of Silicates and Zeolites*. Wiley, Chichester.

E. Epstein (1994). The anomaly of silicon in plant biology. *Proceedings of the National Academy of Sciences of the United States of America* 91, 11–17.

M. Ernst (2003). Heteronuclear spin decoupling in solid-state NMR under magic angle sample spinning. *Journal of magnetic Resonance* 162, 1–34.

M. Ernst, B. Meier, M. Tomaselli, A. Pines (1998). Time reversal of cross-polarization in solid-state NMR. *Molecular Physics* 95, 849–858.

P. Falkowski, R. Barber, V. Smetacek (1998). Biochemical controls and feedbacks on ocean primary production. *Science* 281, 200–206.

F. Fayon, G. Le Saout, L. Emsley, M. D. (2002). Through-bond phosphorus-phosphorus connectivities in crystalline and disordered phosphates by solid-state NMR. *Chemical Communications* 2002, 1702–1703.

F. Fayon, I. J. King, R. K. Harris, K. B. Gover, J. S. O. Evans, D. Massiot (2003). Charakterization of the Room-Temperature Structure of SnP_2O_7 by ^{31}P Through-Space and Through-Bond NMR Correlation Spectroscopy. *Chemistry of Materials* 15, 2234–2239.

F. Fayon, D. Massiot, M. Levitt, J. Titman, D. Gregory, L. Duma, L. Emsley, S. Brown (2005). Through-space contributions to two-dimensional double-quantum J correlation NMR spectra of magic-angle-spinning solids. *Journal of Chemical Physics* 122, 194313.

J. Freitas, F. Emmerich, T. Bonagamba (2000). High-Resolution Solid-State NMR Study of the Occurrence and Thermal Transformations of Silicon-Containing Species in Biomass Materials. *Chemistry of Materials* 12, 711–718.

L. Frigeri, T. Radabaugh, P. Haynes, M. Hildebrand (2006). Identification of proteins from a cell wall fraction of the diatom Thalassiosira pseudonana: insights into silica structure formation. *Molecular & Cellular Proteomics* 5, 182–193.

R. Fu, J. Hu, T. Cross (2004). Rowards quantitative measurements in solid-state CPMAS NMR: A Lee-Goldburg frequency modulated cross-polarization scheme. *Journal in Magnetic Resonace* 168, 8–17.

T. Fuhrmann, S. Landwehr, M. El Rharbi-Kucki, M. Sumper (2004). Diatoms as living photonic crystals. *Applied Physics B: Lasers and Optics* B 78, 257–260.

B. Fung, A. Khitrin, K. Ermolaev (2000). An improved broadband decoupling sequence for liquid crystals and solids. *Journal of Magnetic Resonance* 142, 97–101.

A. Gendron-Badou, T. Coradin, J. Maquet, F. Fröhlich, J. Livage (2003). Spectroscopic characterization of biogenic silica. *Journal of Non-Crystalline Solids* 316, 331–337.

B. Gerstein (1996). CRAMPS. *Encyclopedia of Nuclear Magnetic Resonance* 3, 1501–1509.

R. Gobetto, R. Harris, D. Apperley (1992). Second-Order Quadrupolar Effects on NMR Spectra of Spin-1/2 Nuclei in Solids, Transmitted by Dipolar Coupling. Compounds Containing ^{55}Mn (S=5/2), ^{59}Co (S=7/2), and ^{93}Nb (S=9/2) . *Journal of Magnetic Resonance* 119–130.

C. Gröger, K. Lutz, E. Brunner (2008). NMR Studies of Biomineralisation. *Progress in Nuclear Magnetic Resonance Spectroscopy* in press.

U. Haeberlen (1976). *High Resolution NMR in Solids - Selective Averaging*. Academic Press.

U. Haeberlen, J. Waugh (1968). Coherent Averaging Effects in Magnetic Resonance. *Physical Review* 175, 175–467.

H. Hamdan, M. Muhid, S. Endud, E. Listiorini, Z. Ramli (1997). ^{29}Si MAS NMR, XRD and FESEM studies of rice husk silica for the synthesis of zeolites. *Journal of Non-Crystalline Solids* 211, 126–131.

R. Harris, C. Knight (1983). Silicon-29 nuclear magnetic resonance studies of aqueous silicate solutions. Part 5. First-order patterns in potassium silicate solutions enriched with silicon-29. *Journal of the Chemical Society, Faraday Transactions* 79, 1525–1538.

P. Harrison, R. Waters, F. Taylor (1980). A broad spectrum artificial sea water medium for costal and open ocean phytoplankton. *Journal of the American Chemical Society* 16, 28–35, http://www3.botany.ubc.ca/cccm/NEPCC/esaw.html.

S. Hartmann, E. Hahn (1962). Nuclear Double Resonance in the Rotating Frame. *Physical Review* 128, 2042–2053.

S. Hazelaar, H. van der Strate, W. Gieskes, E. Vrieling (2005). MONITORING RAPID VALVE FORMATION IN THE PENNATE DIATOM NAVICULA SALINARUM (BACILLARIOPHYCEAE). *Journal of Phycology* 354–358.

R. Hecky, K. Mopper, P. Kilham, E. Degens (1973). The amino acid and sugar composition of diatom cell-walls. *Marine Biology* 19, 323–331.

J. Hennel, J. Klinowski (2005). Magic-Angle Spinning: a Historical Perspective. *Topics in Current Chemistry* 246, 1–14.

M. Hildebrand (2000). Silicic acid transport and its control during dell wall silicification in diatoms. *Bäuerlein, E.: Biomineralization - from biology to biotechnology and medical applications. Wiley-VCH, Weinheim* 170–188.

M. Hildebrand, W. Volcani, G. W., J. Schroeder (1997). A gene family of silicon transporters. *Nature* 385, 688–689.

M. Hildebrand, E. York, J. Kelz, A. Davis, L. Frigeri, D. Allison, M. Doktycz (2006). Nanoscale control of silica morphology during diatom cell wall formation. *Journal of Material Research* 21, 2689–2698.

M. Hohwy, H. J. Jakobsen, M. Eden, M. H. Levitt, N. C. Nielsen (1998). Broadband dipolar recoupling in the nuclear magnetic resonance of rotating solids: A compensated C7 pulse sequence. *Journal of Chemical Physics* 108, 2686–2694.

D. Hoppe (2008). Phosphorchalkogenid-Molekülverbindungen. *Doctoral thesis* .

R. Iler (1979). *The Chemistry of Silica*. John Wiley & Sons, New York.

D. Iuga, C. Ader, C. Gröger, E. Brunner (2007). Applications of Solid-State ^{3}1P NMR Spectroscopy. *Annual Reports on NMR Spectroscopy* 60, 145–189.

J. Jeener, B. Meier, P. Bachmann, R. Ernst (1979). Investigation of exchange processes by two-dimensional NMR spectroscopy. *Journal of Magnetic Resonance* 47, 462–475.

M. Karplus (1963). Vicinal Proton Coupling in Nuclear Magnetic Resonance. *Journal of the American Chemical Society* 85, 2870–2871.

S. Kinrade, C. Knight, D. Pole, R. Syvitski (1998a). Silicon-29 NMR Studies of Tetraalkylammonium Silicate Solutions. 1. Equilibria, (29)Si Chemical Shifts, and (29)Si Relaxation. *Inorganic Chemistry* 37, 4272–4277.

S. Kinrade, C. Knight, D. Pole, R. Syvitski (1998b). Silicon-29 NMR Studies of Tetraalkylammonium Silicate Solutions. 2. Polymerization Kinetics. *Inorganic Chemistry* 37, 4278–4283.

S. Kinrade, J. Del Nin, A. Schach, T. Sloan, K. Wilson, C. Knight (1999). Stable five- and six-coordinated silicate anions in aqueous solution. *Science* 285, 1542–1545.

S. Kinrade, A. Schach, R. Hamilton, C. Knight (2001a). NMR evidence of pentaoxo organosilicon complexes in dilute neutral aqueous silicate solutions. *Journal of the Chemical Society, Chemical Communications* 1564–1565.

S. Kinrade, A. Schach, R. Hamilton, C. Knight (2001b). Aqueous hypervalent silicon complexes with aliphatic sugar acids. *Journal of the Chemical Society, Dalton Transactions* 961–964.

S. Kinrade, A.-M. Gillson, C. Knight (2002). Silicon-29 NMR evidence of a transient hexavalent silicon complex in the diatom *Navicula pelliculosa*. *Dalton Transactions* 2002, 307–309.

S. Kinrade, R. Balec, A. Schach, J. Wang, C. Knight (2004). The structure of aqueous pentaoxo silicon complexes with cis-1,2-dihydroxycyclopentane and furanoidic vicinal cis-diols. *Journal of the Chemical Society, Dalton Transactions* 3241–3243.

C. Knight (1988). A two-dimensional silicon-29 nuclear magnetic resonance spectroscopic study of the structure of the silicate anions present in an aqueous potassium silicate solution. *Journal of the Chemical Society, Dalton Transaction* 1988, 1457–1461.

C. Knight, R. Kirkpatrick, E. Oldfield (1986). The unexpectedly slow approach to thermodynamic equilibrium of the silicate anions in aqueous tetramethylammonium silicate solutions. *Journal of the Chemical Society, Chemical Communications* 1986, 66–68.

C. Knight, R. Kirkpatrick, E. Oldfield (1989). Silicon-29 multiple quantum filtered n.m.r. spectroscopic evidence for the presence of only six single site silicate anions in a concentrated potassium silicate solution. *Journal of the Chemical Society, Chemical Communications* 1989, 919–921.

N. Kröger, C. Bergsdorf, M. Sumper (1996). Frustulins: domain conservation in a protein family associated with diatom cell walls. *European Journal of Biochemistry* 239, 259–264.

N. Kröger, R. Deutzmann, M. Sumper (1999). Polycationic peptides from diatom biosilica that direct silica nanosphere formation. *Science* 286, 1129–1132.

N. Kröger, R. Deutzmann, C. Bergsdorf, M. Sumper (2000). Species-specific polyamines from diatoms control silica morphology. *Proceedings of the National Academy of Sciences of the United States of America* 97, 14133–14138.

N. Kröger, R. Deutzmann, M. Sumper (2001). Silica-precipitating peptides from diatoms. The chemical structure of silaffin-A from Cylindrotheca fusiformis. *Journal of Biological Chemisty* 276, 26066–26070.

N. Kröger, S. Lorenz, E. Brunner, M. Sumper (2002). Self-assembly of highly phosphorylated silaffins and their function in biosilica morphogenesis. *Science* 298, 584–586.

J. Kubicki, P. Heaney (2003). Molecular orbital modeling of aqueous organosilicon complexes: implications for silica biomineralization. *Geochimica et Cosmochimica Acta* 67, 4113–4121.

M. Lee, W. Goldburg (1965). Nuclear-Magneitc-Resonance Line Narrowing by Rotating rf Field. *Physical Review* 140, 1261–1271.

Y. K. Lee, N. D. Kurur, M. Helmle, O. G. Johannessen, N. C. Nielsen, M. H. Levitt (1995). Efficient dipolar recoupling in the NMR of rotating solids. A sevenfold symmetric radiofrequency pulse sequence. *Chemical Physics Letters* 242, 304–309.

A. Lesage, C. Auger, S. Caldrelli, L. Emsley (1997). Determination of Through-Bond Carbon-Carbon Connectivities in Solid-State NMR Using the INADEQUATE Experiment. *Journal of the American Chemical Society* 119, 7867–7868.

A. Lesage, M. Bardet, L. Emsley (1999). Through-bond carbon-carbon connectivities in disorderd solids by NMR. *Journal of the American Chemical Society* 121, 10987–10993.

M. Levitt (2000). *Spin Dynamics*. John Wiley & Sons, Chichester.

M. Levitt (2002). Symmetry-Based Pulse Sequences in Magic-Angle Spinning Solid-State NMR. *Encyclopedia of Nuclear Magnetic Resonance* 9, 165–196.

M. Levitt, A. Kolbert, A. Bielcki, D. Ruben (1993). Highr-resolution ^{1}H NMR in solids with frequnecy-switched multiple-pulse sequences. *Solid State Nuclear Magnetic Resonance* 2, 151–163.

H. Lewis, T. Casserly, K. Gleason (2001). Hot-Filament Chemical Vapor Deposition of Organosilicon Thin Films from Hexamethylcyclotrisiloxane and Octamethylcyclotetrasiloxane. *Journal of the Electrchemical Society* F212.

C.-W. Li, S. Chu, M. Lee. (1989). Characterizing the silica deposition vesicle of diatoms. *Protoplasma* 151, 158–163.

K. Lobel, J. West, L. Hench (1996). Computational model for protein-mediated biomineralization of the diatom frustule. *Marine Biology* 126, 353–360.

I. Lowe (1982). Free Induction Decays of Rotating Solids. *Journal of Magnetic Resonance* 47, 462–475.

K. Lutz, C. Gröger, M. Sumper, E. Brunner (2005). Biomimetic silica formation: analysis of the phosphate-induced self-assembly of polyamines. *Physical Chemistry, Chemical Physics* 7, 2812–2815.

J. Ma, N. Yamaji (2006). Silicon uptake and accumulation in higher plants. *Trends Plant Science* 11, 392–397.

J. Ma, K. Tamai, M. Ichii, G. Wu (2002). A rice mutant defective in Si uptake. *Plant Physiology* 130, 2111–2117.

P.-Y. Mabboux, K. Gleason (2005). Chemical Bonding Structure of Low Dielectric Constant Si:O:C:H Films Characterized by Solid-State NMR. *Journal of the Electrchemical Society* 152, F7.

G. Maciel (1996). Silica Surfaces: Characterization. *Encyclopedia of Nuclear Magnetic Resonance* 7, 4370–4386.

G. Maciel, D. Sindorf (1980). Silicon-29 Nuclear Magnetic Resonance Study of the Surface of Silica Gel by Cross Polarization and Magic-Angle Spinning. *Journal of the American Chemical Society* 102, 7606–7607.

K. MacKenzie, M. Smith (2002). *Multinuclear Solid-State NMR of Inorganic Materials*. Pergamon, Amsterdam 2002.

P. Man (1996). Quadrupolar Interactions. *Encyclopedia of Nuclear Magnetic Resonance* 6, 3838–3847.

S. Mann (2001). *Biomineralization - Principles and Concepts in bioinorganic materials chemistry*. Oxford University Press, Oxford.

S. Mann, C. Perry, R. Williams, C. Fyfe, G. Gobbi, G. Kennedy (1983). The characterisation of the nature of silica in biological systems. *Journal of the Chemical Society, Chemical Communications* 1983, 168–170.

M. Maricq, J. Waugh (1979). NMR in rotating solids. *Journal of Chemical Physics* 70, 3300–3316.

H. Marsman (1981). 29Si-NMR Spectroscopic results. *NMR Basic Principles and Progress* 17, 65–235.

H. Marsmann (1996). Silicon-29 NMR. *Encyclopedia of Nuclear Magnetic Resonance* 7, 4386–4398.

V. Martin-Jezequel, P. Lopez (2003). Silicon - a Central Metabolite for Diatom Growth and Morphogenesis. *Müller, W.E.G.: Progress in Molecular and Subcellular Biology. Springer-Verlag Heidelberg* 33, 99–123.

V. Martin-Jezequel, M. Hildebrand, M. Brezinski (2000). Silicon Metabolism in Diatoms: IMPLICATIONS FOR GROWTH. *Journal of Phycology* 36, 821–840.

D. Massiot, F. Fayon, M. Capron, I. King, S. Le Calvé, J.-O. Alonso, B. Durand, B. Bujoli, Z. Gan, G. Hoatson (2002). Modeling one and two-dimensional solid-state NMR spectra. *Magnetic Resonance in Chemistry* 40, 70–76.

M. Mehring (1983). *Principles of High Resolution NMR in Solids*. Springer Verlag.

G. Metz, X. Wu, S. Smith (1994). Ramped-Amplitude Cross Polarization in Magic-Angle-Spinning NMR. *Journal of Magnetic Resonance A* 110, 219–227.

N. Mitani, J. Ma, T. Iwashita (2005). Identification of the Silicon Form in Xylem Sap of Rice (*Oryza sativa* L.) . *Plant & Cell Phyiology* 46, 279–283.

W. Müller (2003). *Progress in Molecular and Subcellular Biology, Vol. 33*. Springer-Verlag, Berlin.

M. Munowitz, A. Pines (1986). Multiple-Qunatum Nuclear Magnetic Resonace Spectroscopy. *Sience* 233, 525–531.

K. Naka (2007). *Biomineralization*. Springer-Verlag, Berlin.

A. Olivieri (1992). Study of Quadrupole-Pertubed Quartets in the Solid State Magic-Angle Spinning ^{31}P NMR Spectra of Phosphine-Cu(I) Complexes. ^{63}Cu Electric Field Gradients and Anisotropy in the ^{31}P, ^{63}Cu Scalar Couplings. *Journal of the American Chemical Society* 5758–5763.

J. Park, K. Kim, T. Park, E. Park, Y. Kim (2006). Solid-state NMR Spectroscopy of Silicon-treated Rice with Enhanced Host Resistance against Blast. *Analytical Sciences* 22, 645–649.

S. Patwardhan, S. Clarson, C. Perry (2005). On the role(s) of additives in bioinspired silicification. *Chemical Communications* 2005, 1113–1121.

C. Perry (1989b). *Biomineralization, Chemical and Biochemical Perspectives*. VHC, Weinheim, p. 223.

C. Perry, T. Keeling-Tucker (2000). Biosilicification: the role of the organic matrix in structure control. *Journal of Biological Inorganic Chemistry* 5, 537–550.

C. Perry, S. Mann (1989a). *Origin, Evolution and Modern Aspects of Biomineralization in Plans and Animals*. Plenum Press, New York, p. 419.

C. Perry, D. Belton, K. Shafran (2003). *Progress in Molecular an Subcellular Biology, Vol 33*. Springer-Verlag, Berlin, p. 269.

A. Pines, M. Gibby, W. J.S. (1972). Proton-enhanced Nuclear Induction Spectroscopy. A Method for High Resolution NMR of Dilute Spins in Solids. *Journal of Chemical Physics* 56, 1776–1777.

A. Pines, M. Gibby, W. J.S. (1973). Free Induction Decays of Rotating Solids. *Journal of Chemical Physics* 59, 569–590.

S. Reiser, G. Brunklaus, J. Hong, J. Chan, H. Eckert, A. Pfitzner (2002). (CuI)3P4S4: preparation, structural, and NMR spectroscopic characterization of a copper(I) halide adduct with beta-P4S4. *Chemistry* 8, 4228–4233.

B.-J. van Rossum, H. Förster, H. de Groot (1997). High-Field and High-Speed CP-MAS 13C NMR Heteronuclear Dipolar-Correlation Spectroscopy of solids with Frequency-Switched Lee-Goldburg Homonuclear Decoupling. *Journal of Magnetic Resonance* 124, 516–519.

N. Sahai (2004). Calculation of ^{29}Si NMR shifts of silicate complexes with carbohydrates, amino acids, and muhicarboxylic acids: potential role in biological silica utilization. *Geochimica et Cosmochimica Acta* 68, 227–237.

N. Sahai, J. Tossell (2001). Formation energies and NMR chemical shifts calculated for putative serine-silicate complexes in silica biomineralization. *Geochimica et Cosmochimica Acta* 65, 2043–2053.

N. Sahai, J. Tossell (2002). (29)Si NMR shifts and relative stabilities calculated for hypercoordinated silicon-polyalcohol complexes: role in sol-gel and biogenic silica synthesis. *Inorganic Chemistry* 41, 748–756.

D. Sakellariou, L. Emsley (2002). Through-Bond Experiments in Solids. *Encyclopedia of Nuclear Magnetic Resonance* 9, 196–211.

J. Schaefer, E. Stejskal (1976). Carbon-13 Nuclear Magnetic Resonance of Polymers Spinning at the Magic Angle. *Journal of the American Chemical Society* 98, 1031–1032.

A.-M. Schmid, D. Schulz (1979). Wall morphogenesis in deiatoms: deposition of silica by cytoplasmic vesicles. *Protoplasma* 100, 267–288.

C. Schmidt-Rohr, H. Spiess (1999). *Multidimensional Solid-State NMR and Polymeres*. Academic Press, London.

H. Schröder, A. Krasko, G. Le Pennec, T. Adell, M. Wiens, H. Hassanein, M. I.M., W. Müller (2003). Silicase, an enzyme which degrades biogenous amorphous silica: contribution to the metabolism of silica deposition in the demosponge Suberites domuncula. *Müller, W.E.G.: Progress in Molecular and Subcellular Biology. Springer- Verlag Heidelberg* 33, 249–268.

H. Schröder, F. Natalio, I. Shukoor, W. Tremel, U. Schlossmacher, X. Wang, W. Müller (2007). Apposition of silica lamellae during growth of spicules in the demosponge Suberites domuncula: biological/biochemical studies and chemical/biomimetical confirmation. *Journal of Structural Biology* 159, 325–334.

A. Sergi, M. Ferrario, S. R. Elliot, I. R. Mc Donald (1995). Molecular dynamics study of the platic-crystalline phase transition of tetraphosphorus triselenide. *Molecular Physics* 84, 727–742.

K. Shimizu, Y. Del Amo, M. Brzezinski, G. Stucky, D. Morse (2001). A novel fluorescent silica tracer for biological silicification studies. *Chemical Biology* 8, 1051–1060.

K. Simkiss, K. Wilbur (1989). *Biominarlization: Cell Biology and Mineral Deposition*. Academic Press, San Diego.

S. Smith, W. Palke, J. Gerig (1992a). The Hamiltonians of NMR - Part I. *Concepts in Magnetic Resonance* 4, 107–144.

S. Smith, W. Palke, J. Gerig (1992b). The Hamiltonians of NMR - Part II. *Concepts in Magnetic Resonance* 4, 181–204.

C. Sullivan (1979). DIATOM MINERALIZATION OF SILICIC ACID IV. KINETICS OF SOLUBLE Si POOL FORMATION IN EXPONENTIALLY GROWING AND SYNCHRONIZED NAVICULA PELLICULOSA. *Journal of Phycology* 15, 210–216.

M. Sumper (2002). A phase separation model for the nanopatterning of diatom biosilica. *Science* 295, 2430–2433.

M. Sumper (2004). Biomimetic patterning of silica by long-chain polyamines. *Angewandte Chemie International Edition in English* 43, 2251–2254.

M. Sumper, E. Brunner (2006b). Learning from Diatoms: Nature's Tools for the Production of Nanostructured Silica. *Advanced Functional Materials* 16, 17–26.

M. Sumper, E. Brunner (2008). Silica Biomineralization in Diatoms: The Model Organism *Thalassiosira pseudonana* . *ChemBioChem* in press.

M. Sumper, G. Lehmann (2006a). Silica pattern formation in diatoms: species-specific polyamine biosynthesis. *Chembiochem* 7, 1419–1427.

M. Sumper, E. Brunner, G. Lehmann (2005). Biomineralization in diatoms: characterization of novel polyamines associated with silica. *FEBS Letters* 579, 3765–3769.

N. Szeverenyi, M. Sullivan, G. Maciel (1982). Observation of Spin Exchange by Two-Dimensional Fourier Transform ^{1}3C Cross Polarization-Magic-Angle Spinning. *Journal of Magnetic Resonance* 47, 462–475.

R. Tacke, B. Pfrommer, M. Plum, R. Bertermann (1999). New Chiral Zwitterionic λ^5Si-Silicates with an SiO_5 or SiO_4C Framework: Syntheses, Crystal Structures, and Properties. *European Journal of Inorganic Chemistry* 1999, 807–816.

K. Thamatrakoln, M. Hildebrand (2007). Analysis of Thalsassiosira pseudonana Silicon Transporters Indicates Distinct Regulaory Levels and Transport Activity through the cell cycle. *Eucaryotic Cell* 6, 271–279.

P. Treguer, D. Nelson, A. Van Bennekom, D. DeMaster, A. Leynaert, B. Queguiner (1995). The silica balance in the world ocean: a reestimate. *Science* 268, 375–379.

C. Van Den Hoek, D. Mann, H. Johns (1997). *Algae. An Introduction to Phycology*. Cambridge University Press, Cambridge.

A. Vega (1996). Quadrupolar Nuclei in Solids. *Encyclopedia of Nuclear Magnetic Resonance* 6, 3869–3889.

R. Verel, J. van Bekk, B. Meier (1999). INADEQUATE-CR Experiments in the Solid State. *Journal of Magnetic Resonance* 140, 300–303.

T. Villareal, L. Joseph, M. Brzezinski, R. Shipe, F. Lipschultz, M. Altabet (1999). BIOLOGICAL AND CHEMICAL CHARACTERISTICS OF THE GIANT DIATOM *ETHMODISCUS* (BACILLARIOPHYCEAE) IN THE CENTRAL NORTH PACIFIC GYRE. *Journal of Phycology* 35, 896–902.

E. Vinogradov, P. Madhu, S. Vega (1999). High-Resolution Proton solid-state NMR spectroscopy by phase-modulated Lee-Goldburg experiment. *Chemical Physics Letters* 314, 443–450.

E. Vinogradov, P. Madhu, S. Vega (2002). Protonen spectroscopy in solid state nuclear magnetic resonance with windowed phase modulated Lee-Goldburg decoupling sequneces. *Chemical Physics Letters* 354, 193–202.

E. Vrieling, S. Hazelaar, W. Gieskes, Q. Sun, T. Beelen, R. van Santen (2003). Silicon biomineralisation: towards mimicking biogenic silica formation in diatoms. *Progress in Molecular and Subcellular Biology* 33, 301–334.

R. Wasylishen, C. Fyfe (1982). High-Resolution NMR of Solids. *Annual Reports on NMR Spectroscopy* 12, 1–221.

J. Waugh, L. Huber, U. Haeberlen (1968a). Approach to High-Resolution NMR in Solids. *Physical Review Letters* 20, 180–182.

J. Waugh, C. Wang, L. Huber, R. Vold (1968b). Multiple-Pulse NMR Experimetns. *Journal of Chemical Physics* 48, 662–670.

J. Weaver, L. Pietrasanta, N. Hedin, B. Chmelka, P. Hansma, D. Morse (2003). Nanostructural features of demosponge biosilica. *Journal of Structural Biology* 144, 271–281.

S. Weiner, , L. Addadi (1997). Design strategies in mineralized biological materials. *Journal of Materials Chemistry* 7, 689–694.

D. Werner (1966). Die Kieselsäure im Stoffwechsel von Cyclotella cryptica. *Archives of Microbiology* 55, 278–308.

E. Williams (1989). *The Chemistry of Organic Silicon Compounds - Part 1*. Wiley, Chichester.

E. Williams, J. Cargiali (1979). Silicon-29 NMR spectroscopy. *Annual reports on NMR spectroscopy* 9, 221–318.

E. Williams, J. Cargioli (1982). Silicon 29 NMR Spectroscopy. *Annual Reports on NMR Spectroscopy* 12, 221–251.

K. Wüthrich (1976). *NMR in biological research: peptides and proteins*. North-Holland.

C. Zurzolo, C. Bowler (2001). Exploring Bioinorganic Pattern Formation in Diatoms. A Story of Polarized Trafficking. *Plant Physiology* 127, 1339–1345.

8 Acknowledgements

At this point, I would like to express my gratitude to:

- **Prof. Dr. Eike Brunner** for giving me the opportunity to work in his research group on such an interesting and well supervised project. I am very grateful for all his personal help, support and guidance I received during my PhD time in Regensburg. I would like to thank him for all the knowledge and skills he taught me and for his patience even if something went wrong.
- **Prof. Dr. Manfred Sumper** and coworkers for the fruitful cooperation and the valuable discussions and ideas and for giving me the opportunity to work in his labs. Special thanks go to **Robert Hett** and **Gerhard Lehmann** for all the qualified support and things they taught me, a physicist, about diatom cultivation. I would like to thank **Dr. Ingrid Weiss** for providing me assistance with the confocal laser microscope.
- **Dr. Joachim Wachter** and **Andreas Biegerl** for the successful cooperation and the preparation of the crystals. In addition, I would like to thank **Prof. Dr. Manfred Scheer** and his coworkers **Dr. Laurence Gregoriades** and **Brian Wegley** for their assistance.
- **Dr. Diana Hoppe** of the group of **Prof. Dr. Arno Pfitzner** for providing the crystals I analyzed. I also thank **Franz Rau** for his help with the preparation of the isotopic enriched silica.
- **Prof. Dr. Dr. Hans Robert Kalbitzer** for the opportunity to use his labs. Special thanks go to **Emmi Fuchs**, **Dr. Christina Schreier**, and the biochemistry group for their advice with words and deeds.
- my colleagues **Katharina Lutz**, **Christoph Liebold**, **Dr. Daniela Baumer**, **Ingrid Cuno**, **Rainer Hartl**, **Dr. Michael Spörner**, and all the other people of our department for the good team play and the loyal and friendly ambiance at work and off-time.
- my parents **Johanna** and **Harald** for their unconditional support during all the years of my study and PhD time.

Last but not least I would like to thank **Heidi** for her patience, understanding and support during this period of my life.

Erklärung:

Hiermit erkläre ich, dass ich die vorliegende Arbeit selbständig angefertigt und keine anderen Hilfsmittel außer den angegebenen verwendet habe.

Regensburg, den 13.05.2008 ________________________